

EFFECTS OF FLOW CONTROL ON A MODIFIED
GLAUERT II AIRFOIL SECTION

By

Benjamin Fredrik Wesley

A Thesis Submitted to the Faculty of the

DEPARTMENT OF AEROSPACE AND MECHANICAL ENGINEERING

In Partial Fulfillment of the Requirements

for the Degree of

MASTER OF SCIENCE

WITH A MAJOR IN AEROSPACE ENGINEERING

In the Graduate College

THE UNIVERSITY OF ARIZONA

2007

STATEMENT BY AUTHOR

This thesis has been submitted in partial fulfillment of the requirements for an advanced degree at The University of Arizona and was deposited in the University Library to be made available to borrowers under rules of the Library and under copyright protection rules.

Brief quotations from this thesis are permissible, provided that accurate acknowledgment of the source is made. Requests for permission for extended quotation from or reproduction of this manuscript in whole or in part may only be granted by the author.

THESIS DEFENSE DATE: 07/02/2007

SIGNED: Benjamin Wesley

APPROVAL BY THESIS DIRECTOR

This thesis has been approved on the date shown below:

Dr. Israel Wagnanski _____ 07/02/2007

Professor of Aerospace and Mechanical Engineering

Date

ACKNOWLEDGEMENTS

This research project has been made possible through the generous support of many people. Although not everyone can be mentioned, I would like to recognize those who have been most critical for making this project a success. First and foremost, I would like to thank my advisor Dr. Israel Wygnanski for his financial support, his contributions in project direction, and his unwavering motivation to drive the project into new domains that previously have not been properly addressed. Additionally, thanks go to Dr. Ahmed Hassan for providing his CFD results, L. Taubert for his help with PIV technique, and turntable design, Priyank Varghese for his programming and experimental contributions, and Boris Zakharin for his help with programming, experimental testing, project direction, and fundamental fluid knowledge. Finally, I would like to dedicate this manuscript to my father, Dr. J. P. Wesley, who passed away this year. His influence, guidance and support played a great role in helping me work and complete this.

TABLE OF CONTENTS

LIST OF FIGURES	8
LIST OF CHARTS	13
NOMENCLATURE	18
ABSTRACT	22
1. INTRODUCTION	23
1.1 Historical Summary of the GLAS II Airfoil Section	23
1.2 Passive Flow Control	24
1.3 Active Flow Control.....	25
1.3.1 Parameters Governing AFC	28
1.4 Objective of Current Research	30
1.5 Airfoil Design.....	30
2. EXPERIMENTAL SETUP.....	32
2.1 1.22 m X 0.91 m Low Speed Wind tunnel.....	32
2.1.1 Wind tunnel Contraction Setup.....	33
2.1.2 Wind tunnel Splitter Plate Setup.....	33
2.2 Davis Wind tunnel.....	34
2.3 GLAS II Airfoil.....	35
2.3.1 Configuration A	36
2.3.2 Configuration B	38
2.3.3 Configuration C	39
2.3.4 Configuration D	40
2.4 Motion Drive System	41
2.5 Pressure and Velocity Measurement Systems.....	41
2.5.1 Wake Rake and Airfoil Static Pressure Measurement System	42
2.5.2 Airfoil Dynamic Pressure Measurement System	43
2.5.3 U_{∞} Measurement	43
2.5.4 Hotwire Velocity Measurement System	44

TABLE OF CONTENTS--Continued

2.6	Data Acquisition.....	45
2.7	Active Flow Control Devices.....	45
2.7.1	Centrifugal Blower	46
2.7.2	External Domzalski Actuators	47
2.7.3	Internal Domzalski Actuators	48
3.	EXPERIMENTAL PROCEDURES.....	50
3.1	Hotwire Calibration.....	50
3.2	Pressure System Calibration	51
3.3	ZMF Control Actuator Calibration	53
3.4	Continuous Blowing or Suction AFC Calibration	60
4.	AERODYNAMIC COEFFICIENTS.....	63
4.1	Total Drag	63
4.1.1	Total Drag Calculations	63
4.1.2	Pressure Drag Calculations	67
4.2	Lift Calculations.....	70
4.3	Moment Calculations	70
5.	ERROR ESTIMATIONS	71
5.1	Combined Error.....	71
5.2	Instrumentation and Resolution Errors	71
5.2.1	U_∞ Measurement Errors.....	71
5.2.2	Static Aerodynamic Coefficient Amplitude Errors	72
5.2.3	Unsteady Aerodynamic Coefficient Amplitude Errors	73
5.2.4	Hotwire Measurement Errors.....	74
5.2.5	Other DAQ Errors.....	75
5.3	Aerodynamic Errors	76
5.3.1	Freestream/Test-section Angularity.....	76
5.3.2	Pitot-Static Pressure Measurement Errors	76
5.3.3	Airfoil Tap Static Pressure Read - Error.....	77
5.3.4	Static Pressure Error in Wake Measurements.....	78

TABLE OF CONTENTS--Continued

5.4	Post Processing Analysis Read – Error	79
6.	RESULTS AND DISCUSSION	80
6.1	Baseline Results	80
6.1.1	Baseline Re Sweep Clean	80
6.1.2	Re Dependence for Clean vs. Tripped Airfoil	83
6.1.3	Sensitivity of Airfoil Performance to Wind tunnel Turbulence	88
6.1.4	Airfoil Geometry Variation Effects	96
6.1.5	Historical Baseline Comparison	99
6.1.6	Hysteresis Analysis.....	102
6.1.7	Baseline CFD Study.....	110
6.1.8	Effects of Roughness	113
6.1.9	Quarter Chord Moment Coefficient Analysis.....	118
6.2	AFC Results	120
6.2.1	Case Study to Verify Glauert’s Data	120
6.2.2	CFD ZMF Actuation Slot Optimization Analysis	129
6.2.3	The Importance of Slot Location (69.3% vs. 59%)	132
6.2.4	Steady vs. Unsteady AFC through 59% Slot at Re = 117K	133
6.2.5	Steady vs. Unsteady AFC at Re = 235K.....	137
6.2.6	Steady vs. Unsteady AFC at Re = 352K.....	139
6.2.7	Effects of C_{μ} and F^+ on Aerodynamic Performance.....	142
6.2.8	Effects of Roughness on ZMF Control Performance	146
6.2.9	Effect of ZMF - and ZMF - control with Roughness on $C_{mc/4}$	150
6.2.10	Open Loop Control through ZMF Control Parameters	151
6.3	Smoke Wire Flow Visualization Experiments.....	160
6.5.1	Baseline Flow Study	160
6.5.2	AFC Flow Study	164
6.4	Particle Image Velocimetry Flow Visualization Experiments.....	168
6.5	Conclusion.....	174
APPENDIX.....		176

REFERENCES	177
------------------	-----

LIST OF FIGURES

FIGURE 1. A TOP DOWN SCHEMATIC OF THE SCOBEE TUNNEL TEST-SECTION . DIMENSIONS ARE IN CM'S.....	33
FIGURE 2. ADDED SCOBEE WIND TUNNEL CONTRACTION USING A SPLITTER PLATE, WHICH EXTENDED 2.5 CHORD LENGTHS DOWNSTREAM OF THE TE.	34
FIGURE 3. TOP VIEW SCHEMATIC OF THE DAVIS GRADUATE WIND TUNNEL INSIDE THE AERODYNAMICS LABORATORY WITH THE AIRFOIL, TURNTABLE, RAKE, AND PITOT TUBE INSTALLED.	35
FIGURE 4. GLAS II DIMENSIONS AS A FRACTION OF THE MAIN CHORD WITH EXCHANGEABLE AFT LOFT MODULE A) FOR A 0.813 MM WIDE ACTUATION SLOT AT 69.3% CHORD AND B) FOR A 0.711 MM WIDE ACTUATION SLOT AT 59.0% CHORD.	36
FIGURE 5. STATIC PRESSURE TAP LOCATIONS MEASURED IN PERCENTAGES OF THE MAIN CHORD WITH ORIGIN AT THE LE FOR AIRFOIL CONFIGURATION A.	37
FIGURE 6. A) FULLY ASSEMBLED AND POLISHED GLAS II AS SEEN FROM A 15° BOTTOM PERSPECTIVE VIEW WITH AFT LOFT MODULE A) INSTALLED AND THE SLOT LOCATION AT 69.3% CHORD AND B) THE COMPLETE SPANWISE PROFILE WITH VIEW OF THE 7 SEGMENTED SLOT.....	38
FIGURE 7. PRESSURE TAP LOCATIONS WITH TWO ADDITIONAL TAPS IN THE BL SEPARATION LOCATION AS WELL AS A NEW SLOT LOCATION AT 59% CHORD.....	39
FIGURE 8. SPT AND DPT LOCATIONS AS PERCENTAGES OF CHORD. SPT'S ARE INDICATED BY YELLOW DIAMONDS AND DPT LOCATIONS ARE INDICATED BY RED CIRCLES.....	40
FIGURE 9. A) ANGLED TOP 45° PERSPECTIVE OF COVERED GLAS II. THE LEFT ENDPLATE WAS NOT COVERED IN ORDER TO ALLOW LIGHT TO PASS FOR THE CAMERA AND/OR FROM THE LIGHT SOURCES AND B) THE SLOT SEEN IN A 30° BACKWARD TILTED PERSPECTIVE PARTIALLY THROUGH THE CLEAR ENDPLATE.	41
FIGURE 10. A) ISEL STEPPER MOTOR CONTROL UNIT WITH THREE STEPPER MOTOR CONTROL CARDS AND ONE PC INTERFACE CARD AND B) STEPPER MOTOR WITH Y DIRECTION LEAD SCREW FOR RAKE POSITIONING.	41

LIST OF FIGURES--Continued

- FIGURE 11. A) THE PRESSURE SYSTEM IN MONITORING MODE AND B) TWO ESP-32BP PRESSURE SCANNER MODULES WITH FOUR MINIATURE PRESSURE CONNECTORS AND C) SCHEMATIC OF THE WHEATSTONE CONFIGURATION PIEZORESISTIVE SCANNER DIES.¹⁴ 42
- FIGURE 12. A) THE NATIONAL INSTRUMENTS PC WITH 6 AVAILABLE SCXI UNIVERSAL STRAIN GAUGES AND B) ONE ENDEVCO TRANSDUCER WITH POLYURETHANE TYGON TUBING ADAPTER READY FOR INTEGRATION INTO THE AIRFOIL TO REPLACE CHOSEN STATIC PRESSURE PORTS.¹⁵ 43
- FIGURE 13. A) PITOT TUBE WITH STAGNATION PRESSURE PORT AT THE NOSE AND SEVERAL PERPENDICULAR STATIC PRESSURE PORTS ABOUT 5 CM DOWNSTREAM B) CONNECTED TO A DIFFERENTIAL AND PROPORTIONAL MKS PRESSURE TRANSDUCER.¹⁶ 44
- FIGURE 14. EQUIPMENT NECESSARY FOR PERFORMING HOTWIRE MEASUREMENTS WITH A) TEN CHANNEL HOTWIRE & FILM AA LABS ANEMOMETER AND B) A 8 POLE LP/HP BUTTERWORTH/BESSEL FILTER AND C) PROBE USED TO MEASURE VELOCITIES.¹⁷ 45
- FIGURE 15. A) CENTRIFUGAL PUMP FOR CONTINUOUS “STEADY” WITH THE UPPER SUCTION PORT AND THE SIDE BLOWING PORT B) ILLUSTRATIVE OF THE SCFM METER WITH A SCALE FROM 10-100 SCFM TO MEASURE THE FLOW RATE AND REGULATE THE MOMENTUM INPUT INTO THE FLOW AND C) THE VARIAC TO REGULATE THE PUMP FEED VOLTAGE AND THEREBY REGULATING THE ROTATION SPEED OF THE MOTOR THAT CHANGES THE VOLUMETRIC FLOW RATES.¹⁹ 47
- FIGURE 16. LARGE EXTERNAL DOMZALSKI ACTUATOR WITH BOTH FORCING COILS VISIBLE FROM THE SIDE. THE RIGHT IMAGE SHOWS THE SINGLE FORCING PORT EXITING FROM THE TOP. 48
- FIGURE 17. A) DOMZALSKI ACTUATOR AS SEEN FROM THE TOP WITH FIXED PERMANENT DRIVER MAGNET AND A COIL ATTACHED TO SQUARE COMPOSITE MEMBRANE AND B) ACTUATOR COOLING BODY AND C) THE AIRFOIL ASSEMBLED WITH 6 OF THE 7 ACTUATORS INSTALLED WITHOUT THE COOLING BODIES AS SEEN FROM THE SIDE..... 49
- FIGURE 18. PRESSURE SYSTEM FLOW DIAGRAM TO BETTER VISUALIZE THE INFORMATION FLOW DURING CALIBRATION AND DAQ. 52
- FIGURE 19. AIRFOIL SLOT CALIBRATION FLOW DIAGRAM HIGHLIGHTING ALL THE EQUIPMENT USED DURING CALIBRATION AND THE ORDER IN WHICH THEY WERE USED AND IN WHICH DATA WAS PROCESSED. 55

LIST OF FIGURES--Continued

FIGURE 20. CV ANALYSIS APPLYING NEWTON'S SECOND LAW TO A STEADY, INVISCID FLOW WITH NO BODY FORCES. ²¹	65
FIGURE 21. SCHEMATIC OF UPPER LOFT PRESSURE SIGNATURE TO ILLUSTRATE USAGE OF TRAPEZOIDAL INTEGRATION OF PRESSURES MEASURED BY THE PRESSURE SYSTEM.....	69
FIGURE 22. LIFT AND DRAG COMPONENTS OF PRESSURE FORCE FOR TWO TAPS ON AN AIRFOIL WITH LOCAL SURFACE INCLINATION ANGLE AND GLOBAL ANGLE OF ATTACK OF THE AIRFOIL.	70
FIGURE 23. A) IDEAL AIRFOIL PRESSURE TAP GEOMETRY MEASURING THE CORRECT P_s B) UPSTREAM BURR DECREASING P_s C) DOWNSTREAM BURR INCREASING P_s D) DOWNSTREAM ROUGHNESS WITH SIMILAR EFFECT AS DOWNSTREAM BURR ON P_s	78
FIGURE 24. A) V-ROUGHNESS STRIPS WERE APPLIED ALONG THE AIRFOIL SPAN (B) AT 36 % AND 55 % CHORD AND B) VORTEX GENERATOR STRIPS WERE PLACED WITHIN THE RAMP AT 75% CHORD ALONG B.	84
FIGURE 25. CHANGES IN AIRFOIL GEOMETRY FOR VARIOUS EXPERIMENTS.	98
FIGURE 26. BASELINE CFD STUDY WITH U VELOCITY CONTOURS. COMPUTATIONS WERE PERFORMED AT 54.9 M/S AT $\alpha = 0^\circ$ AND 10° ON A CLEAN AIRFOIL. ¹³	112
FIGURE 27. SAND ROUGHNESS STRIP WERE APPLIED ALONG B ON THE TS AT 30%, 36%, 38% AND 58 % CHORD AND ON THE BS AT 56% AND 60% CHORD.	113
FIGURE 28. CFD STUDY OF U VELOCITY CONTOURS AROUND THE GLAS II. THE COMPUTATIONS WERE PERFORMED AT 54.9 M/S AND $\alpha = 0^\circ, 4^\circ, 6^\circ,$ AND 8° . ZMF CONTROL DISTURBANCES WERE INTRODUCED AT 59% CHORD WITH 200 HZ AND $C_{\mu}=0.88\%$. ¹³	131
FIGURE 29. CFD VORTICITY STUDY OF A GENERIC RAMP TO GAUGE CHANGES IN STREAMLINE REATTACHMENT LENGTH HERE FOR STEADY SUCTION AT $C_{\mu} = 1\%$ AT $(Y,X) = (0,0)$ SHOWN TO ILLUSTRATE STREAMLINE PATTERNS WITHIN THE RAMP REGION AND EXPLAIN THE PRESSURE RISE IN THE RAMP OPPOSITE OF THE FLOW DIRECTION. ⁷	159
FIGURE 30. BASELINE SMOKE-WIRE STUDY OF THE GLAS II'S LE AT $\alpha = 0^\circ$ AND 1.35 M/S IN CONFIGURATION D.	162

LIST OF FIGURES--Continued

- FIGURE 31. BASELINE SMOKE-WIRE IMAGE OF THE TS RAMP AT $\alpha = 0^\circ$ AND 1.35 M/S. SHEAR LAYER ROLLUP WAS INDICATED THROUGH CONCENTRATED SMOKE STREAK LINES. THE FLOW SEPARATED FROM THE TS AROUND 50% CHORD. 163
- FIGURE 32. BASELINE SMOKE-WIRE IMAGE OF THE BS RAMP $\alpha = 0^\circ$ AND 1.35 M/S. THE FLOW SEPARATED AT BS $\sim 70\%$ CHORD AND THE SHEAR LAYER ROLLED UP IN THE CCW DIRECTION. 164
- FIGURE 33. ZMF ACTUATION SMOKE-WIRE IMAGE OF THE AIRFOIL NOSE AT $\alpha = 0^\circ$ AND 1.35 M/S. FORCING PARAMETERS WERE $F = 200$ HZ AND $C_\mu = 176\%$ IN AIRFOIL CONFIGURATION C AND D. 165
- FIGURE 34. ZMF CONTROL SMOKE-WIRE IMAGE OF THE TS RAMP AT $\alpha = 0^\circ$ AND 1.35 M/S. FORCING PARAMETERS WERE $F = 200$ HZ AND $C_\mu = 176\%$ IN AIRFOIL CONFIGURATION C AND D. 166
- FIGURE 35. ZMF CONTROL SMOKE-WIRE IMAGE OF THE BS RAMP AT $\alpha = 0^\circ$ AND 1.35 M/S. FORCING PARAMETERS WERE $F = 200$ HZ AND $C_\mu = 176\%$ IN AIRFOIL CONFIGURATION C AND D. 167
- FIGURE 36. ZMF CONTROL SMOKE-WIRE IMAGE OF THE BS RAMP AT $\alpha = 0^\circ$ AND 1.35 M/S. FORCING PARAMETERS WERE $F = 100$ HZ AND $C_\mu = 65.8\%$ IN AIRFOIL CONFIGURATION C AND D. 167
- FIGURE 37. INSTANTANEOUS PIV IMAGE OF SPANWISE FLOW STRUCTURES ILLUMINATED BY A LASER SHEET PLACED PERPENDICULAR TO THE FLOW WITHIN THE RAMP DURING A BASELINE RUN AT 20 M/S. THE WHITE LINE INDICATES THE TE. 170
- FIGURE 38. INSTANTANEOUS PIV STUDY OF SPANWISE FLOW STRUCTURES ILLUMINATED BY A LASER SHEET PLACED PERPENDICULAR TO THE FLOW WITHIN THE RAMP DURING ZMF ACTUATION AIRFOIL CONFIGURATION C WITH $C_\mu = 0.88\%$ AND $F = 200$ HZ. 171
- FIGURE 39. AVERAGED PIV IMAGE OF SPANWISE VORTICITY WITHIN THE RAMP DURING A BASELINE RUN AT 20 M/S. $Y/C = 0$ INDICATED THE TE OF THE AIRFOIL AND $Y/C = 0.318$ INDICATED THE UPPER LOFT OF THE GLAS II. 172

LIST OF FIGURES--Continued

FIGURE 40. ZMF CONTROL AVERAGED PIV IMAGE OF SPANWISE RAMP VORTICITY AT 20 M/S WITH F = 200 Hz, $C_{\mu} = 0.88\%$. Y/C = 0 INDICATED THE TE AND Y/C = 0.318 INDICATED THE UPPER LOFT OF THE GLAS II.	173
---	-----

LIST OF CHARTS

CHART 1. SHOWS A TEN POINT CALIBRATION CURVE WITH U_{JET} VS. $V_{HOTWIRE}$ WITH A 5 TH ORDER POLYNOMIAL CURVE FIT.....	51
CHART 2. C_{μ} IN PERCENT VS. V_{RMS} FOR CONFIGURATION A AND ONE EXTERNAL ZMF CONTROL ACTUATOR AT 20 M/S. TWO OUTBOARD SLOTS WERE TAPED. $H = 0.813$ MM, $C = 25.16$ CM AND $L = 9.17$ CM.....	56
CHART 3. C_{μ} IN PERCENT VS. F FOR CONFIGURATION A WITH ONE EXTERNAL ZMF CONTROL ACTUATOR AT 20 M/S. TWO OUTBOARD SLOTS WERE TAPED. AND $H = 0.813$ MM, $C = 25.16$ CM AND $L = 9.17$ CM.	57
CHART 4. C_{μ} IN PERCENT VS. V_{RMS} WITH CONFIGURATION B,C, AND D USING INTERNAL ZMF ACTUATION AT 20 M/S WITH $H = 0.711$ MM, $C = 25.16$ CM AND $L = 11.6$ CM.....	58
CHART 5. C_{μ} IN PERCENT VS. F FOR VARIOUS V_{RMS} WITH CONFIGURATION B, C, AND D USING INTERNAL ZMF CONTROL ACTUATION AT 20 M/S WITH $H = 0.711$ MM, $C = 25.16$ CM AND $L = 11.6$ CM.	59
CHART 6. 2 D CHECK WITH U_{RMS} VS. Z/B AND $B = 60.96$ CM. $F = 100$ HZ AND $V_{RMS} = 12$ VOLTS. SEVEN INTERNAL DOMZALSKI ACTUATORS IN CONFIGURATION B, C, AND D WERE USED.....	60
CHART 7. C_{μ} IN PERCENT VS. SCFM FOR CONFIGURATION A, AND B AT $U_{\infty} = 20$ M/S. SLOT CALIBRATION WAS PERFORMED WITH A SINGLE HOTWIRE AT THE SLOT EXIT. TWO OUTBOARD SLOTS WERE TAPED AND ONE EXTERNAL CENTRIFUGAL PUMP WAS CONNECTED. $H = 0.813$ MM, $C = 25.16$ CM AND $L = 9.17$ CM.....	62
CHART 8. BASELINE STUDY OF C_L VS. α AND C_D AT 7 M/S, 12 M/S, 20 M/S AND 30 M/S FOR A CLEAN AIRFOIL WITH OPEN SLOT AND $\Delta\alpha = 2^{\circ}$ FROM 0° TO 26° . THE AIRFOIL IN CONFIGURATION C WITH LOWER CONTRACTION WAS USED.	81
CHART 9. BASELINE STUDY OF L/D VS. C_L AND α AT 7 M/S, 12 M/S, 20 M/S AND 30 M/S FOR A CLEAN AIRFOIL WITH OPEN SLOT AND $\Delta\alpha = 2^{\circ}$ FROM 0° TO 26°	83
CHART 10. BASELINE STUDY OF C_L AND C_D VS. Re AT $\alpha = 14^{\circ}$ WITH A CLEAN AND TRIPPED AIRFOIL IN CONFIGURATION C USING THE LOWER CONTRACTION.	85

LIST OF CHARTS--Continued

CHART 11. C_p VS. X/C DISTRIBUTIONS FOR $\alpha = 14^\circ, 16^\circ$ AND 18° AT $Re = 117K, 235K$ AND $352K$ IN AIRFOIL CONFIGURATION B WITHIN THE DAVIS WIND TUNNEL.....	87
CHART 12. BASELINE C_L VARIATION STUDY OF MULTIPLE DATA SETS WITH C_L VS. α AT VARIOUS Re 'S. ^{2,23,24}	91
CHART 13. BASELINE STUDY OF C_p VS. X/C AT $Re \approx 330K$ CORRESPONDING TO ROUGHLY ~ 20 M/S FOR A CLEAN AIRFOIL COMPARING SCOBEE TUNNEL 2004, 2005, 2007 AND DAVIS TUNNEL 2005 DATA AT $\alpha = 4^\circ$ AND 8°	94
CHART 14. BASELINE STUDY OF C_L VS. C_D AT AN AVERAGE $Re \approx 350K$ CORRESPONDING TO ROUGHLY ~ 20 M/S. THE AIRFOIL WAS CLEAN AND SCOBEE TUNNEL 2005, 2007 AND DAVIS TUNNEL 2005 WERE COMPARED WITH SALTER'S 1948 DATA.	94
CHART 15. DAVIS WIND TUNNEL TURBULENCE STUDY OF SINGLE HOTWIRE VELOCITY POWER SPECTRA TAKEN IN 2006. THE SAMPLING FREQUENCY WAS 4096HZ AT ~ 5 MINUTES SAMPLING TIME.	96
CHART 16. HISTORICAL BASELINE COMPARISON OF C_L VS. α AND C_D AND BEST MATCHING Re 'S FOR A CLEAN AIRFOIL WITH OPEN SLOT IN CONFIGURATION C AND ADDED CONTRACTION. ^{2,24}	101
CHART 17. HISTORICAL BASELINE COMPARISON OF L/D VS. C_L AND α FOR BEST MATCHING Re 'S. A CLEAN AIRFOIL WITH OPEN SLOT IN CONFIGURATION C WITH ADDED CONTRACTION WAS USED. ^{2,24}	102
CHART 18. STALL HYSTERESIS STUDY AT $Re = 112K$ FOR A CLEAN AIRFOIL IN CONFIGURATION C USING THE ADDED CONTRACTION. SOLID RED LINES MARKED $\alpha+$ WHILE DOTTED BLUE LINES INDICATED $\alpha-$	104
CHART 19. C_p DISTRIBUTIONS AT $\alpha = 22^\circ, 24^\circ$, AND 26° AROUND HYSTERESIS. $Re = 112K$ FOR A CLEAN AIRFOIL IN CONFIGURATION C AND ADDED CONTRACTION. SOLID RED LINES MARKED $\alpha+$ WHILE DOTTED BLUE LINES INDICATED $\alpha-$	105
CHART 20. HYSTERESIS AT $Re = 320K$ FOR A CLEAN AIRFOIL IN CONFIGURATION C USING THE ORIGINAL 2004/2005 SCOBEE TUNNEL CONTRACTION. SOLID RED LINES MARKED $\alpha+$ WHILE DOTTED BLUE LINES INDICATED $\alpha-$	107

LIST OF CHARTS--Continued

- CHART 21. HYSTERESIS STUDY OF C_p VS. x/c AT $Re = 320K$ AT $\alpha = 0^\circ, 4^\circ, 6^\circ$ AND 8° FOR $\alpha+$ (RED TS AND PINK BS) AND $\alpha-$ (BLUE TS AND GREEN BS). 109
- CHART 22. C_L VS. α , AND C_D AND $Re = 320K$. ROUGHNESS AT $x/c = 0.56$ BS, 0.58 TS, AND 0.36 TS WAS APPLIED. THE AIRFOIL CONFIGURATION C WITH ORIGINAL CONTRACTION WAS USED. 115
- CHART 23. L/D VS. C_D AT $Re = 320K$. ROUGHNESS AT $x/c = 0.56$ BS, 0.58 TS, AND 0.36 TS WAS APPLIED. THE AIRFOIL CONFIGURATION C WITH ORIGINAL CONTRACTION WAS USED. 116
- CHART 24. C_L VS. α , AND C_D AND $Re = 480K$. ROUGHNESS AT $x/c = 0.36$ TS AND 0.38 TS WAS APPLIED. THE AIRFOIL CONFIGURATION C WITH ORIGINAL CONTRACTION WAS USED. 117
- CHART 25. L/D VS. C_D AND $Re = 480K$. ROUGHNESS AT $x/c = 0.36$ TS AND 0.38 TS WAS APPLIED. THE AIRFOIL CONFIGURATION C WITH ORIGINAL CONTRACTION WAS USED. 118
- CHART 26. BASELINE STUDY OF $C_{M/C4}$ VS. $\alpha+$ AT 7 M/S, 12 M/S, 18 M/S, 20 M/S AND 30 M/S FOR A CLEAN AIRFOIL AND 12 M/S FOR AN AIRFOIL WITH VARIOUS APPLIED ROUGHNESS STRIPS AND VORTEX GENERATORS. THE AIRFOIL TESTED WAS IN CONFIGURATION C AND THE ADDED CONTRACTION WAS USED. 119
- CHART 27. STEADY AFC STUDY OF C_L VS. α AND C_{DP} AT 20 M/S. THE AIRFOIL WAS CLEAN AND TWO CENTRIFUGAL TYPE BLOWERS WERE USED IN AIRFOIL CONFIGURATION A USING THE ORIGINAL CONTRACTION. 122
- CHART 28. STEADY AFC STUDY OF SUCTION AND BLOWING L/D_p VS. C_L AND α AT 20 M/S. 123
- CHART 29. STEADY AFC STUDY OF C_L VS. α AND C_{DP} . TESTS WERE DONE AT 30 M/S FOR A CLEAN AIRFOIL WITH AIRFOIL CONFIGURATION A USING THE ORIGINAL CONTRACTION. 124
- CHART 30. STEADY AFC STUDY OF L/D_p VS. C_L AND α . TESTS WERE DONE AT 30 M/S FOR A CLEAN AIRFOIL. 125
- CHART 31. STEADY AFC STUDY OF C_L VS. α AND C_{DP}/C_D AT 20 M/S FOR A CLEAN AIRFOIL. UNDERGRADUATE 2004 DATA USING THE ORIGINAL CONTRACTION WAS COMPARED TO GLAUERT'S DATA.² 127

LIST OF CHARTS--Continued

CHART 32. SCOBEE TUNNEL 2004 SUCTION AFC STUDY OF L/D_p VS. C_L AND α COMPARED TO GLAUERT'S L/D PERFORMANCE 20 M/S BUT VERY DIFFERENT Re 'S FOR A CLEAN AIRFOIL. ..	128
CHART 33. SLOT OPTIMIZATION STUDY OF C_L VS. α AT 20 M/S. THE 69.3% CHORD SLOT EFFICACY, WITH $H = 0.711$ MM, WAS COMPARED TO THE OPTIMIZED 59% CHORD ONE, WITH $H = 0.813$ MM SLOT.	133
CHART 34. AFC STUDY OF THE C_L VS. α AND C_D AT 7 M/S FOR A CLEAN AIRFOIL IN CONFIGURATION B. $H = 0.711$ MM AND $C = 25.16$ CM.	135
CHART 35. AFC STUDY OF L/D AND L/T VS. C_L AT 7 M/S FOR A CLEAN AIRFOIL IN CONFIGURATION B.	136
CHART 36. AFC STUDY OF C_L VS. α AND C_D AT 14 M/S FOR A CLEAN AIRFOIL WITH MODERATE C_{μ} 'S.	138
CHART 37. AFC PERFORMANCE STUDY OF L/D VS. C_L AND α AT 14 M/S FOR A CLEAN AIRFOIL WITH MODERATE C_{μ} 'S.	138
CHART 38. AFC C_L VS. α AND C_{dp} & C_D AT 20 M/S FOR A CLEAN AIRFOIL WITH MODERATE TO SMALL C_{μ} 'S.	139
CHART 39. AFC PERFORMANCE STUDY OF L/D & L/D_p VS. C_L AND α AT 20 M/S FOR A CLEAN AIRFOIL AT SMALL C_{μ}	140
CHART 40. ZMF FORCING PARAMETER STUDY OF C_L VS. α AND C_D AT 20 M/S. A CLEAN AIRFOIL IN AIRFOIL CONFIGURATION C WITH ORIGINAL CONTRACTION WAS USED. $L = 11.6$ CM, $H = 0.711$ MM, AND $C = 25.16$ CM.	143
CHART 41. ZMF CONTROL PARAMETER STUDY OF L/D VS. C_L AND α AT 20 M/S FOR A CLEAN AIRFOIL.	144
CHART 42. ZMF CONTROL PARAMETER STUDY OF C_L VS. α AND C_D AT 30 M/S FOR CLEAN AIRFOIL. THE SCOBEE TUNNEL WITH THE ORIGINAL CONTRACTION WAS USED.	145

LIST OF CHARTS--Continued

CHART 43. ZMF FORCING PARAMETER STUDY OF L/D VS. C_L AND α AT 30 M/S FOR A CLEAN AIRFOIL.	146
CHART 44. ROUGHNESS EFFECTS ON ZMF ACTUATION STUDY AT 20 M/S COMPARING A CLEAN TO A TRIPPED AIRFOIL.....	147
CHART 45. ROUGHNESS EFFECTS ON ZMF FORCING STUDY AT 30 M/S COMPARING A CLEAN TO A TRIPPED AIRFOIL.....	149
CHART 46. ZMF CONTROL STUDY OF $C_{MC/4}$ AT 7 M/S, 12 M/S, 18 M/S, 20 M/S AND 30 M/S FOR A CLEAN AIRFOIL AND 12 M/S FOR AN AIRFOIL WITH VARIOUS APPLIED ROUGHNESS STRIPS AND VORTEX GENERATORS. THE AIRFOIL TESTED WAS IN CONFIGURATION C AND THE SPLITTER PLATE SETUP WAS USED.....	151
CHART 47. ZMF CONTROL FREQUENCY SWEEP AT $\alpha = 0^\circ$ WITH C_μ VS. C_L AND C_{DP}/C_D AT 14 M/S FOR A CLEAN AIRFOIL IN CONFIGURATION B.....	153
CHART 48. ZMF CONTROL FREQUENCY SWEEP AT $\alpha = 0^\circ$ WITH C_μ VS. L/D AT 14 M/S FOR A CLEAN AIRFOIL IN CONFIGURATION B.....	154
CHART 49. C_p WITH $F^+ = 0.36$ AND 1.80 AT $C_\mu = 0.3\%$ COMPARED TO BASELINE AT 14 M/S. THE AIRFOIL WAS CLEAN AT $\alpha = 0^\circ$	155
CHART 50. C_μ SWEEP STUDY OF C_p DISTRIBUTIONS BEFORE AND AFTER $\Delta\partial CL/\partial C_\mu$ OCCURRED COMPARED TO BASELINE AT 14 M/S AND $\alpha = 0^\circ$ FOR A CLEAN AIRFOIL AND EXTERNAL ZMF CONTROL AT $F = 50$ HZ.	156
CHART 51. ZMF ACTUATION FREQUENCY SWEEP AT $\alpha = 6^\circ$ WITH C_L AND C_{DP} VS. C_μ AT 14 M/S FOR A CLEAN AIRFOIL.	157
CHART 52. C_μ SWEEP STUDY OF C_p DISTRIBUTIONS BEFORE AND AFTER $\Delta\partial CL/\partial C_\mu$ OCCURRED COMPARED TO BASELINE AT 14 M/S AND $\alpha = 6^\circ$ FOR A CLEAN AIRFOIL AND EXTERNAL ZMF ACTUATION AT $F = 50$ HZ.....	158

NOMENCLATURE

Coefficients

<p>A = angle of attack of slot on a circular cylinder</p>	<p>$L/D_p = L/D$ based on C_{dp}: $\frac{C_L}{C_{dp}}$</p>
<p>α = main element angle of attack in [°]</p>	<p>L/T = thrust performance: $\frac{C_L}{-C_D}$</p>
<p>b = airfoil span</p>	<p>m = mass</p>
<p>c = chord length</p>	<p>μ = dynamic viscosity</p>
<p>q = dynamic pressure: $\frac{1}{2} \rho U_\infty^2$</p>	<p>ν = kinematic viscosity: $\frac{\rho}{\mu}$</p>
<p>C_D = total drag coefficient: $\frac{D}{q \times c}$</p>	<p>Ω_z = z plane vorticity</p>
<p>C_{dp} = pressure drag coefficient: $\frac{\int (p - p_\infty) dy}{q \times c}$</p>	<p>P_0 = total/ stagnation pressure</p>
<p>C_f = skin friction coefficient</p>	<p>P_s = static pressure</p>
<p>C_L = total lift coefficient: $\frac{L}{q \times c}$</p>	<p>Re = Reynolds number: $U_\infty \frac{c}{\nu}$</p>
<p>C_p = pressure coefficient</p>	<p>ρ = density of the medium: $\frac{m}{\nabla}$</p>
<p>c_{μ}, c_m = steady momentum coefficient: $\left(\frac{2h}{c} \right) \left(\frac{U_{jet}}{U_\infty} \right)^2$</p>	<p>St = Strouhal number: $F \frac{\theta}{U}$</p>

$$C_{\mu}, C_m = \text{unsteady } c_{\mu}, c_m: \left(\frac{2h}{c} \right) \left(\frac{U_{rms}}{U_{\infty}} \right)^2 \text{ in [\%]}$$

$C_{mc/4}$ = quarter chord moment coefficient

$$C_Q = \text{mass flow coefficient: } \left(\frac{Q}{U_{\infty} c} \right) \text{ in [\%]}$$

$\Delta\phi$ = phase difference between sensors

Δx = distance between the corresponding sensors

F = frequency of excitation

$$F^+ = \text{fixed non-dimensional frequency: } \frac{F \times L}{U_{\infty}}$$

h = excitation slot width

L = characteristic length of the ramp

$$L/D = \text{performance parameter: } \frac{C_L}{C_D}$$

Sub/Super-scripts

d = drag

D = total drag

f = flap

t = thickness

τ = time

θ = momentum thickness

U, U_{∞} = freestream velocity

U_{jet} = mean slot exit jet velocity

U_{ph} = vortex phase velocity: $2f \frac{\Delta x}{\Delta\Phi}$

U_{rms} = rms unsteady jet velocity: $\frac{U_{jet}}{\sqrt{2}}$

U_w = deficit velocity of the wake

V_{rms} = rms excitation voltage

\forall = volume

rms = root mean square

x = streamwise

y = perpendicular to chord

l = lift

μ = momentum

p = pressure

z = spanwise

∞ = infinity

Acronyms

2 D = two dimensional

3 D = three dimensional

AFC = active flow control

AME = Aerospace & Mechanical Engineering College

AOA = angle of attack

BL = boundary layer

BS = bottom surface

CAT = compressed air wind tunnel

ccw = counter clockwise

CFD = computational fluid dynamics

cw = clockwise

DPT = dynamic pressure tap

DAQ = data acquisition

FSO = full-scale output

NI = National Instruments

PIV = particle image velocimetry

PSI = Pressure System Incorporated

PC = personal computer

RPM = revolutions per minute

SL = streamline

SCFM = std air cubic feet per minute

SM = smoke wire flow visualization

SPT = static pressure tap

STL = streak line

SWV = smoke-wire visualization

TE = trailing edge

TS = top surface

UAV = unmanned air vehicle

GLAS II = modified Glauert type II airfoil section

UofA = The University of Arizona

LE = leading edge

ZMF = zero mass-flux

NPL = National Physical Laboratory

ABSTRACT

Several active flow control, as well as passive flow control, schemes were applied to a modified Glauert II “laminar” airfoil section. Zero mass-flux oscillatory suction and blowing and net mass-flux steady suction, or steady blowing were applied through a segmented spanwise slot. Static and dynamic pressures were measured. Pressures around the main element and within the wake were analyzed in order to gauge the performance through aerodynamic coefficients. Unsteady AFC was found to be effective as well as efficient. Several flow visualization techniques were used to aid the static analysis of the pressure distributions. Separation bubbles, recirculation zones, jump in stagnation location, spanwise-, and streamwise vortices were visualized. The present research attempts to quantify the control efficacy of unsteady zero mass-flux control and its ability to reattach the flow and/or prevent separation. The concave curvature of the ramp was of concern as were the flow instabilities present due to the concavity.

1. INTRODUCTION

1.1 Historical Summary of the GLAS II Airfoil Section

The GLAS II was the creation of M. B. Glauert in 1947 through the application of the exact method of aerofoil design theory to a high lifting suction airfoil. The GLAS II was designed to have a maximum thickness to chord ratio of 31.5%, to operate using massive suction through a slot located at 69.3% chord shown in Figure 4. By implementation of these design characteristics, Glauert was able to create an airfoil that had favorable pressure gradients over most of the upper and lower lofts while maintaining laminar flow until reaching the location of the suction slot. The thickness of the airfoil, in addition to its asymmetry, generated a large C_L without the use of flaps. Suction through the 69.3% chord slot, as shown in Figure 4 and module a), provided a pressure discontinuity across the slot that created a favorable pressure gradient along the entire concave recovery ramp, which resulted in the flow over the ramp to reattach in a turbulent manner.^{1,2}

The possible applications of the GLAS II airfoil were immediately recognized, and following its introduction there were several publications introducing and exploring the potential uses of the airfoil. However, it was quickly discovered there were also difficulties with the new and radical design. The difficulty with a 31.5% thick airfoil was the decreased minimum pressure due to its thickness. This created a more severe adverse pressure gradient, and to compensate the pressure recovery had to begin earlier. At the specified maximum thickness, the recovery had to start with the steepest possible gradient. Liebeck addressed this issue by stating that the thickest possible section must have a boundary layer

that is just on the verge of separation throughout the recovery portion.³ This was Glauert's aim when he designed the suction airfoil with its distinct recovery ramp design.

The L/D for the GLAS II was measured for a variety of operating conditions. With adequate suction through the 69% chord slot, the measured L/D varied from 250 to 550, for $C_L > 1$ and $Re \sim 1,000K$. In absence of suction L/D was 12 for the same Re , with C_L being reduced to $C_L \approx 0.6$. The L/D increased to approximately 30 at $Re \sim 3,000K$. It appeared that the flow was intermittently reattaching to the ramp just upstream of the trailing edge (TE) resulting in large drag oscillations. Blowing through the same slot location appeared to be less effective than suction since it required a larger mass-flux to force the flow to reattach. For blowing, the c_μ required to keep the flow attached was in excess of 20% and for suction in excess of 4%.³ The GLAS II's performance was staggering because it presented a high lifting airfoil with a possible L/D of 550, which exceeded conventional airfoils today by an order of magnitude. If C_μ could be reduced at similar L/D, by using ZMF actuation, it would lay the foundation for a new era in aviation.

1.2 Passive Flow Control

Passive flow control (PFC) was aimed at controlling high lift flight scenarios, such as in the cases of take-off, landing, and fast maneuvering. Sudden boundary layer separation would cause the airfoil to stall midway through one of these maneuvers, dramatically increasing its drag and decreasing its lift. The interest in passive flow control was initiated by the prospects of delaying this sudden stall that characteristically occurred when the

airfoil's angle of attack was generating its maximum lift. The first attempts to delay the stall were made by placing devices such as vortex generators or riblets on the TE of the airfoil. This led to making modifications to the actual design of the airfoil's TE. Eventually, PFC was applied to an airfoil by tripping the BL from laminar to turbulent state by use of roughness, and trip strips on the surface. The applied tripping, and/or roughness improved the mixing in the BL, which improved the diffusion of additional momentum from the mainstream flow into the BL. This increased the BL's energy content, thereby making it less sensitive to adverse pressure gradients. Adverse pressure gradients could cause the flow to stagnate locally resulting in separation bubbles or complete BL separation. Vortex generators introduced streamwise vortices into the flow, thereby improving the mixing from the high to the low momentum fluid. This had a similar effect than roughness, though much more pronounced, and with the downside of substantial increased skin friction drag. In the subsequent experiments on a GLAS II roughness strips and vortex generators were used in the effect henceforth described.

1.3 Active Flow Control

Active flow control (AFC) is a technique used to alter the flow around an airfoil, thereby influencing lift, drag and moments that are naturally generated by the airfoil within a streaming flow.

AFC can be divided into two categories, one in which mass is injected or removed from the flow, in addition to adding momentum, and one in which no net mass is injected or removed from the flow, but momentum is.

Steady blowing adds momentum to the flow continuously via a steady jet, which also adds mass to the flow. In addition a blowing jet entrains mass from the surrounding freestream.

Steady suction is designed to remove mass in areas of stagnation so bubbles and/or dead-water zones may be eliminated. Suction can also remove the entire BL, thereby allowing it to develop again downstream of the suction source. Even though low momentum fluid is removed the net effect on the flow is that of adding momentum due to suction due to acceleration of the flow upstream of the slot.

Unsteady AFC can also be subdivided into multiple categories. Listed in order of importance, these include oscillatory AFC (ZMF control) exhibiting the same suction and blowing phase applied in a sinusoidal wave fashion, unsteady blowing without the suction phase, and unsteady suction without the blowing phase all versions applied through an unsteady fluid jet that can be two dimensional or three dimensional. All three of the unsteady AFC subcategories can be further divided into mass flow actuation and no mass flow or zero mass-flux (ZMF) actuation.

ZMF control was shown to be as or more effective at similar momentum inputs (c_{μ} 's, C_{μ} 's) than steady AFC, which will be elaborated on in the discussion and results section.

The primary reason as to why ZMF control is superior to steady AFC is the fact that it takes advantage of many of the instabilities that occur in the separation or dead-water zone.

This zone often exhibits interesting flow characteristics due to instabilities that were generated because of large velocity and/or pressure gradients. Some of these observable phenomena are reverse flow, coherent structures, and time dependent flow. These may include periodic shedding of vortices, typically in counter-rotating pairs of Van Karman type.

The ZMF control concept involves the introduction of periodic perturbations into the flow by generating vortices through an instability mechanism that are amplified downstream. This transports momentum from the main freestream into areas of lower momentum, enhancing the mixing and promoting a reduced wake size. The concept can be traced back to the work of D. Oster, where he demonstrated that by forcing a mixing layer, the spreading rate increased and large coherent structures enhanced the entrainment capacity of the flow through momentum transfer across the shear layer.^{4,5}

Katz *et al.* performed harmonic excitation at the apex of a wedge.⁶ On one side was entrained fluid bound by the mixing layer, and the wedge was on the other, which dropped the pressure and forced the mixing layer to bend towards the surface and promoted reattachment. Neuburger and Wygnanski discovered that an oscillating ribbon next to the leading edge (LE) of a NACA 0015 airfoil, improved its' stall, and lift.⁷ Experiments on wall jets by Katz *et al.*, Zhou and Wygnanski indicated, that the amplification region of a forced oscillation was dependent on the velocity distribution in the jet, particularly the momentum excess provided by forcing.⁸ As a result any disturbances generated by the control device were amplified and convected downstream to the location where they became

most effective. Seifert *et al.* performed testing on a hollow, flapped NACA 0015 that was equipped with a two-dimensional slot over the flap.^{9, 10} The airfoil was subjected to steady and modulated blowing, and it was determined that the latter was a major factor for improving performance at lower momentum inputs. They observed a significant increase in lift, as well as concomitant reduction of form drag at reduced frequencies based on the flap chord for Reynolds number considered. In addition to lift enhancement, the pulsating jet effectively eliminated the large wake area for the majority of the post-stall region. Greenblatt and Wygnanski subjected an airfoil to periodic excitation at typical Micro Air Vehicle Reynolds numbers of 50,000. Under the effects of oscillations, the flow was able to withstand an adverse pressure gradient of much higher magnitude before separation, thus transforming a non-lifting airfoil into one that approached performance of that of conventional airfoils.^{4, 11}

1.3.1 Parameters Governing AFC

There are several parameters in use to benchmark AFC performance. One can imagine that the perturbation frequency in Equation (1) and amplitude in Equation (2) play a role.

$$\text{a) } F^+ = \frac{L}{\left(\frac{U_\infty}{F}\right)} = \frac{\text{Characteristic Length}}{\text{Wavelength of Perturbation}} \quad \text{b) } St = \frac{\theta}{\left(\frac{U_\infty}{F}\right)} = \frac{\text{Momentum Thickness}}{\text{Wavelength of Perturbation}} \quad (1)$$

$$\text{a) } c_{\mu} = \frac{2h}{c} \left(\frac{U_{jet}}{U_{\infty}} \right)^2 \quad \text{b) } C_{\mu} = \frac{2h}{c} \left(\frac{U_{rms}}{U_{\infty}} \right)^2 = \frac{h}{c} \left(\frac{U_{peak}}{U_{\infty}} \right)^2 \quad (2)$$

The frequency is useful in order to compare the airfoil's shedding frequency to an equivalent 2 D cylinder shedding frequency dependent on the height and/or length of the pressure recovery region. The amplitude of the perturbation is desirable in order to compare the momentum of the induced oscillating jet to the momentum of the freestream. Other parameter of importance include, but are not limited to, the slot geometry, slot height, jet ejection angle to the flow, slot location with respect to the TE, and LE, ducting design, 2 D vs. 3 D forcing, shape, thickness, and dimensions of the airfoil.⁴

F^+ , the induced nondimensional frequency of oscillations, is defined by the ratio between the wavelengths of the induced vortex sheets as they are amplified further downstream to the reference length from the origin of the generated perturbations to the TE of the airfoil. In case of a cylinder or very thick airfoil the Strouhal number (St), can be of importance being representative of the vortex shedding frequency aft of a 2 D cylinder.

The momentum coefficient C_{μ} , is the measure of the momentum input into the flow by the jet relative to the freestream momentum. For continuous excitation, such is the case in continuous blowing or continuous suction Equation (2 a) is used and for an oscillatory jet that exhibits a suction phase and blowing phase, Equation (2 b) is applied.

1.4 Objective of Current Research

The goal of the present project was to benchmark the control efficacy of several flow control methods and realize some of the historically claimed results by Glauert. If comparable performance could be realized using periodic excitation at considerably smaller C_{μ} levels, the use of GLAS II type airfoils could be revived. The large volume inside the airfoil, which may be used for transport of cargo, fuel, or the reduction of the wings weight makes GLAS II a good candidate for “span loader” or blended wing concepts. Another goal was to understand the dynamic mechanism involved in the attachment and separation process and how those mechanisms interact with AFC excitation. The airfoil was tested at low Reynolds numbers ranging from 300,000 to 500,000 and the effect of flow control on the lift, and drag performance as well as the pressure distribution was analyzed. The slot location was optimized using CFD results to improve the cost function of control. The airfoil was tripped to prevent hysteresis for repeatable results. Steady actuation ranged from 20 SCFM to 200 SCFM, unsteady actuation frequencies ranged from 20Hz to 700Hz, and C_{μ} 's ranged from 0.01% to 30%. There still was much interest in high lifting airfoils such as the Glauert airfoil. A recent research project of a hump that was placed on the wind tunnel wall and whose shape represents GLAS II's upper loft for validation of CFD codes highlights that.¹²

1.5 Airfoil Design

Two GLAS II airfoil design variations were tested. The first test airfoil had two modifications to Glauert's design; the recovery ramp curvature lacked the discontinuity

bump present in the original design, as well as the sharp TE. In addition to these modifications, the second airfoil also had changes made to the LE, slot width, slot location, and surface roughness. Detailed descriptions of these changes are given in Section 2.3.

2. EXPERIMENTAL SETUP

2.1 1.22 m X 0.91 m Low Speed Wind tunnel

The majority of experiments were carried out in the open suction wind tunnel of the AME lab at the UofA. The tunnel is called Scobee tunnel in honor of Richard Scobee. The wind tunnel's test-section was 122.0 cm wide and 91.4 cm as shown in Figure 1. The GLAS II was sandwiched between two round Plexiglas endplates. These plates were recessed within the wind tunnel wall, in order not to disturb the flow. A turntable was connected to one of the endplates and a stepper motor powered the turntable via a belt, with further discussion of the motion setup consult Section 2.4. The belt fixed the alpha and stabilized the airfoil illustrated in Figure 1. The test-section airflow velocity could be modified by two means. First, by controlling the RPM of the wind tunnel's axial 16 bladed fan. The fan was powered by a three-phase electric motor, which could be remotely controlled through a three-phase transistor motor control system from 0 RPM to 566 RPM. The motor to fan gear ratio was one to one (1:1). Second, the 16 blades of the fan had variable pneumatic pitch control from 0% to 100%. This changed the generated thrust, and therefore, the airflow speed within the test-section, after accounting for losses. Velocities within the test-section, incorporating the airfoil and the contraction, ranged from 12 m/s to 35 m/s corresponding to approximate blade passing frequencies of 78 Hz to 254 Hz. A maximum test-section velocity of 50 m/s made this wind tunnel a favorite wind tunnel for the conducted research.

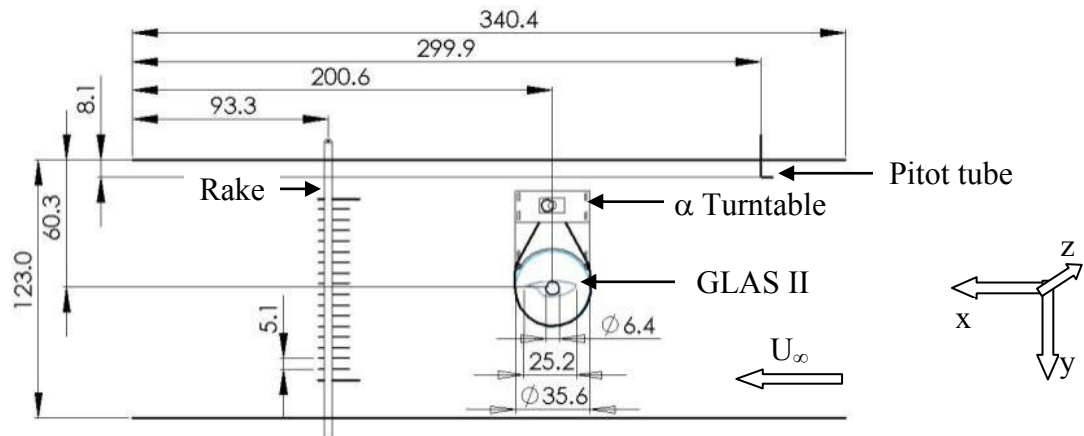


Figure 1. A top down schematic of the Scobee tunnel test-section . Dimensions are in cm's.

2.1.1 Wind tunnel Contraction Setup

The 91.4 cm tall test-section was modified by a contraction to reduce the height to 60.96 cm in order to incorporate the GLAS II's 60.96 cm wingspan vertically within the center of the test-section. The contraction was an Aerodynamics Laboratory design and attention was paid to ensure that no separation occurred in the downstream section of the contraction. The smallest diffuser angle was chosen equal to 15° based on the length of the contraction and the necessity of a level 1.52 m contraction floor downstream of the airfoil.

2.1.2 Wind tunnel Splitter Plate Setup

Instead of a contraction a new setup was used that had been designed and built in the Aerodynamics Laboratory shown in Figure 2. A 2.5" pipe was used as a spacer on whom the airfoil rotated. To avoid interactions between the flow around the cylinder and the airfoil a large splitter plate was mounted between the pipe and the airfoil. The splitter

plate extended 2.5 chord lengths downstream of the airfoil, which also prevented any flow from underneath the splitter plate to impinge on the wake rake. The splitter plate was 1.5 chord lengths wide and extended 6.35 cm ahead of the TE.

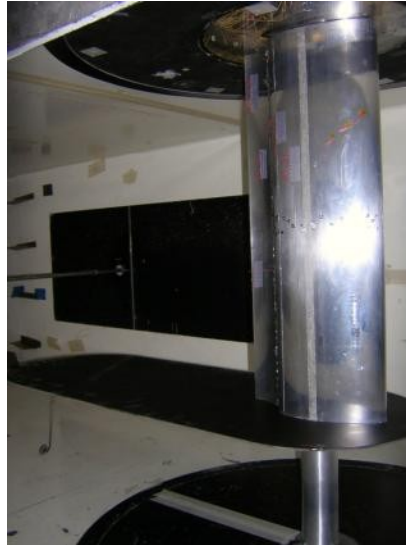


Figure 2. Added Scobee wind tunnel contraction using a splitter plate, which extended 2.5 chord lengths downstream of the TE.

2.2 Davis Wind tunnel

Some of the earliest experiments were conducted in the graduate blow-down wind tunnel (Davis wind tunnel) in the Aerodynamics Laboratory at the UofA with schematic shown in Figure 3. The wind tunnel was equipped with a 2.4 m high by 0.61 m wide test-section and incorporated the 60.96 cm span airfoil vertically. It's 11-bladed centrifugal type blower was driven by an electric motor which RPM could be controlled remotely through a transistor inverter. The motor to fan gear ratio was 1:1.15. The generated test-section

velocities ranged from 5 m/s to 15 m/s corresponding to approximate blade passing frequencies of 10.4 Hz to 30 Hz.

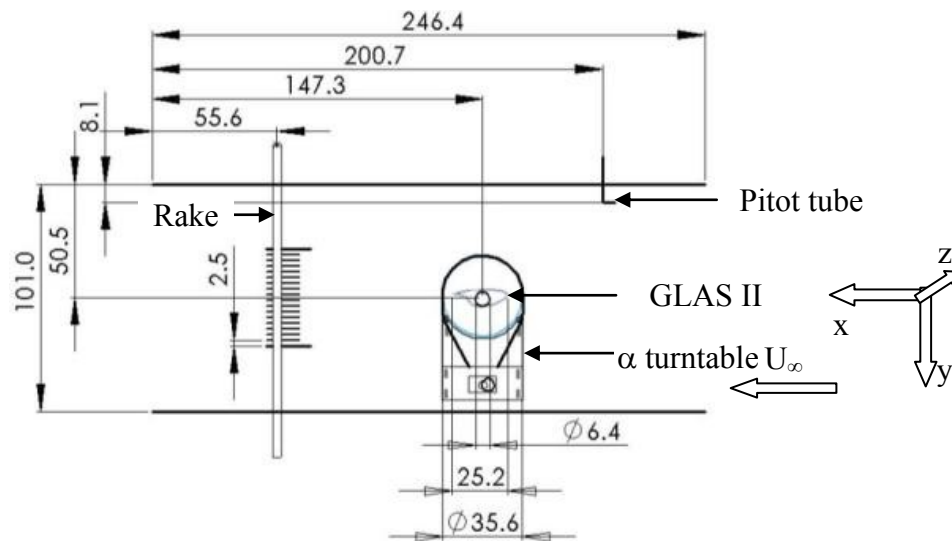


Figure 3. Top view schematic of the Davis graduate wind tunnel inside the Aerodynamics Laboratory with the airfoil, turntable, rake, and Pitot tube installed.

2.3 GLAS II Airfoil

The test subject was a multi-element GLAS II airfoil with modified pressure-recovery ramp geometry. The ramp did not incorporate the discontinuity introduced around the suction slot by Glauert using Lighthill's method.¹ The test subject was composed of four main pieces as shown in Figure 4. Because of its modular design each one of the pieces could be modified and easily back incorporated into the assembly as a whole. This allowed fast and flexible changes in geometry and/or slot location. The airfoil had a chord of 25.16 cm and a thickness of 7.93 cm. Both slots were cut into seven spanwise segments and each one of the segments could be actuated individually if desired. During internal ZMF

actuation, all seven segments were connected through the forcing chamber. Four main airfoil configurations were tested listed in chronological order.

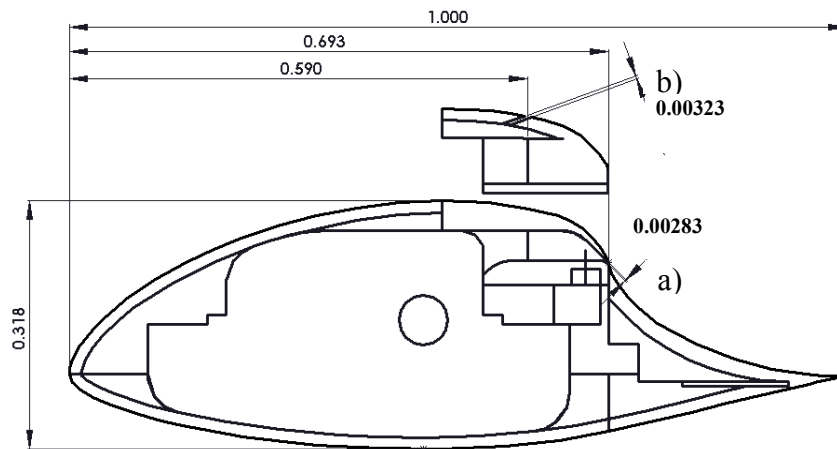


Figure 4. GLAS II dimensions as a fraction of the main chord with exchangeable aft lift module a) for a 0.813 mm wide actuation slot at 69.3% chord and b) for a 0.711 mm wide actuation slot at 59.0% chord.

2.3.1 Configuration A

The original configuration had 57 static pressure taps shown in Figure 5. The SPT's were unevenly distributed midspan around the entire airfoil. The uneven distribution diagonally offset each pressure tap with respect to the upstream one. Any disturbance that could have been generated by the upstream tap would not impinge on a tap aligned in the downstream direction reducing chance of measurement error.

It is common to check if within the recovery portion of the airfoil the flow is in fact 2 dimensional. Hence, two additional pressure taps are placed along the span to the left and right of the midspan pressure tap. In case of the GLAS II the SPT 30, at 79.6% chord,

was the midspan pressure tap or the 30th tap from the LE moving downstream and SPT 31 and 32 were used to check for 2D flow aligned along the span. After the PIV investigation of the ramp region discussed in Section 6.4 it became clear that the flow within the ramp had three-dimensional instabilities.

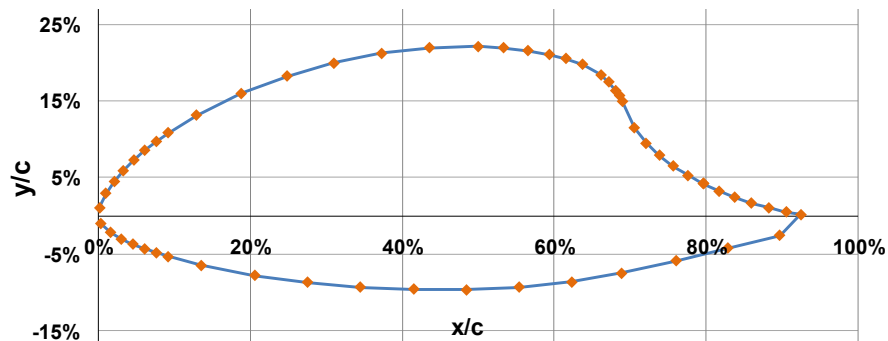


Figure 5. Static pressure tap locations measured in percentages of the main chord with origin at the LE for airfoil configuration A.

The slot was located at 69.3% chord measured from the LE as originally dictated by Glauert's suction slot design see Figure 6. The jet ejected at an angle of 30.6° , not tangential to the adjacent surface. The airfoil was polished with no roughness or steps on its surface. No internal actuation was applied during these experiments. Instead, external actuation was applied through ports centered in the left- and rightmost endplates. Continuous blowing, continuous suction, and external AFC were the flow control modes investigated in configuration A.

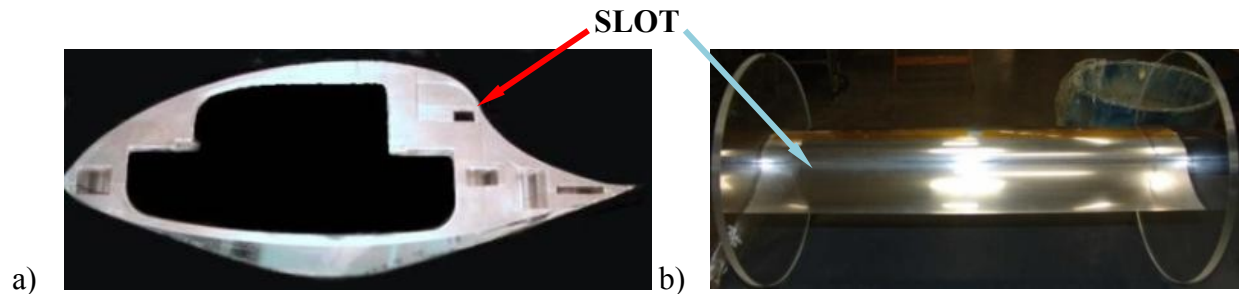


Figure 6. a) Fully assembled and polished GLAS II as seen from a 15° bottom perspective view with aft loft module a) installed and the slot location at 69.3% chord and b) the complete spanwise profile with view of the 7 segmented slot.

2.3.2 Configuration B

In this configuration, 59 SPTs were unevenly distributed midspan around the entire airfoil with locations indicated in Figure 7. 2 D check was accomplished with two additional SPTs 33 and 34 centered along the span within the ramp and in line with SPT 32. The aft loft module was replaced with module b) in order to move the slot to 59% chord measured from the LE. This was done after flow control has had essentially no effect using configuration A at any momentum input and CFD analysis conducted by Ahmed Hassan indicated BL separation around 60% chord.¹³ Two additional pressure ports were added with the new slot module to increase the data resolution within the predicted separation region. The jet ejected at an angle of 29.7°, not tangential to the adjacent surface. The airfoil was polished (clean) with and without applied surface roughness. One external Domzalski actuator provided the necessary momentum for ZMF actuation.

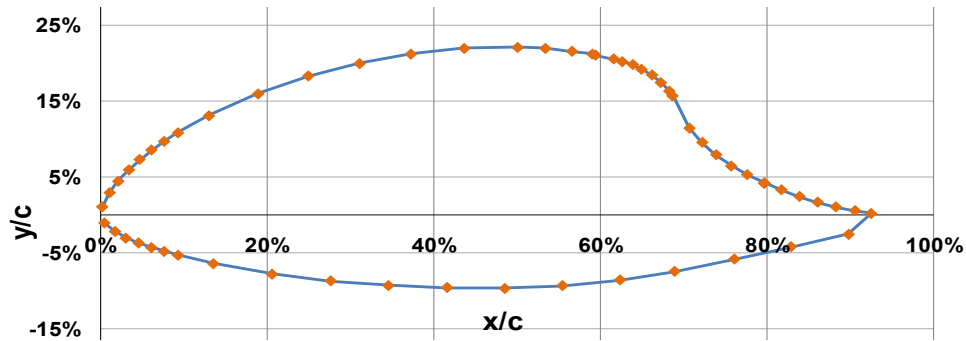


Figure 7. Pressure tap locations with two additional taps in the BL separation location as well as a new slot location at 59% chord.

2.3.3 Configuration C

In this configuration, 44 SPTs were distributed midspan around the entire airfoil seen in Figure 8. 15 dynamic pressure taps (DPT) were replacing 15 SPT's at locations of interest. One DPT was responsible for measuring the slot exit pressure around the midspan of the slot. Endevco pressure transducers were connected to those taps through short Tygon tubing adapters. No 2 D check was performed in the ramp region because measurements indicated that flow within the ramp had significant three dimensionality. For a more detailed discussion on 3 D flow structures refer to Section 6.4. The same aft loft module b) was used during experiments. The airfoil was polished with various types of roughness and/or vortex generators applied along the airfoils span, in different combinations. Seven internal Domzalski actuators generated the required momentum input.

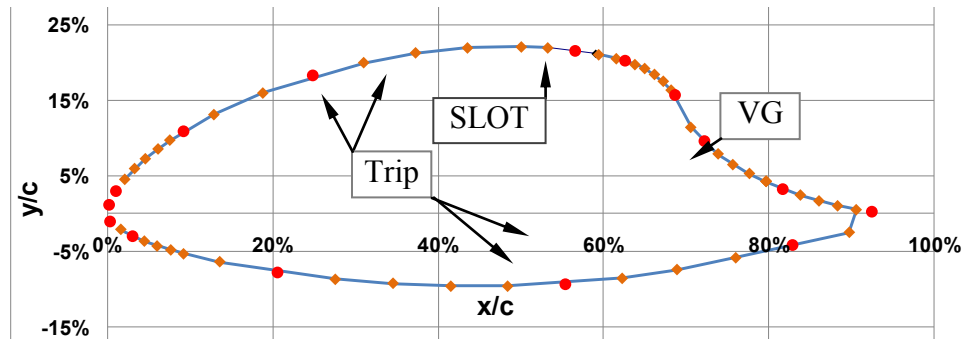


Figure 8. SPT and DPT locations as percentages of chord. SPT's are indicated by yellow diamonds and DPT locations are indicated by red circles

2.3.4 Configuration D

In this configuration, the entire airfoil was covered in a highly light absorptive and refractive black adhesive material shown in Figure 9. All other exposed metal parts such as bolts, pins, and surfaces were colored black. All pressure ports were sealed. The 59% chord slot was open and ready for ZMF actuation in airfoil configuration C. The black surface coating was applied during all flow visualization experiments for smoke-wire and PIV technique. It minimized reflections from halogen lamps and/or laser sheets. It also absorbed reflected light from the light source. Roughness was applied on the top surface (TS) at 36% chord.

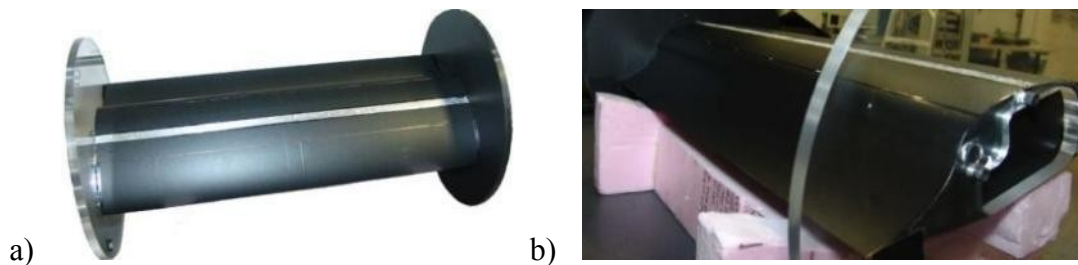


Figure 9. a) Angled top 45° perspective of covered GLAS II. The left endplate was not covered in order to allow light to pass for the camera and/or from the light sources and b) the slot seen in a 30° backward tilted perspective partially through the clear endplate.

2.4 Motion Drive System

A techno-isel multi axis stepper motor control powered two stepper motors shown in Figure 10. One stepper motor positioned the rake moving it along the y direction; the other stepper motor was connected to the airfoil turntable setup and adjusted the angle of attack around $\pm 35^\circ$. The stepper motor connected to the turntable setup also locked the airfoil in place preventing any α play.

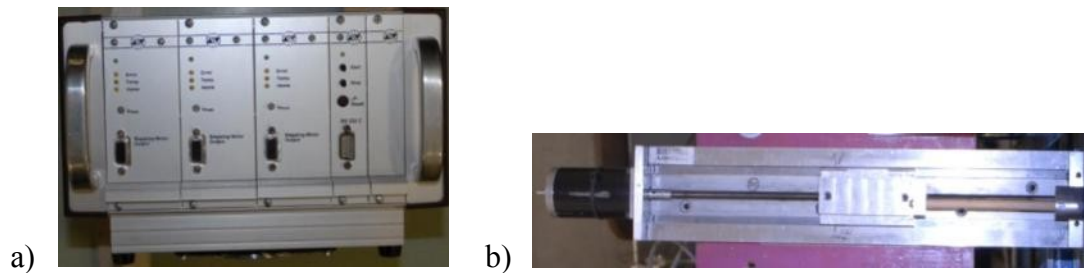


Figure 10. a) Isel stepper motor control unit with three stepper motor control cards and one PC interface card and b) stepper motor with y direction lead screw for rake positioning.

2.5 Pressure and Velocity Measurement Systems

Various tools were used to gather data on pressures and velocities of interest. Each one of them was sophisticated and accurate. Much of the functionality of those tools remained hidden and was mostly considered as a black box with concern only of its inputs and outputs, thereby relying on previous research that had shown these tools to be useful and operational. For static measurements manometers, Baratrons, and a Pressure System device

was utilized. For time dependent measurements and slot calibration a National Instruments device and a hotwire anemometer was used.

2.5.1 Wake Rake and Airfoil Static Pressure Measurement System

A rake measured the total drag force on the airfoil. The rake had 16 total pressure measurement tubes and 2 outboard static ones'. The rake was placed into the wind tunnel about three chord lengths downstream of the airfoil as a rule of thumb, at a right angle in the y direction see Figure 1. The rake and airfoil pressures were scanned electronically with the fast, flexible, and modular PSI (Esterline model PSI 8400) shown in Figure 11 a). The PSI system uses differential pressure scanner with 16 or 32 (Esterline model ESP-16BP, ESP 32BP) piezoresistive silicon pressure dies per unit (Esterline model DH200) and/or a combination thereof see Figure 11 b). The piezoresistors are connected in a Wheatstone bridge configuration and the output voltage generated is proportional to the input pressure with a schematic shown in Figure 11 c).¹⁴

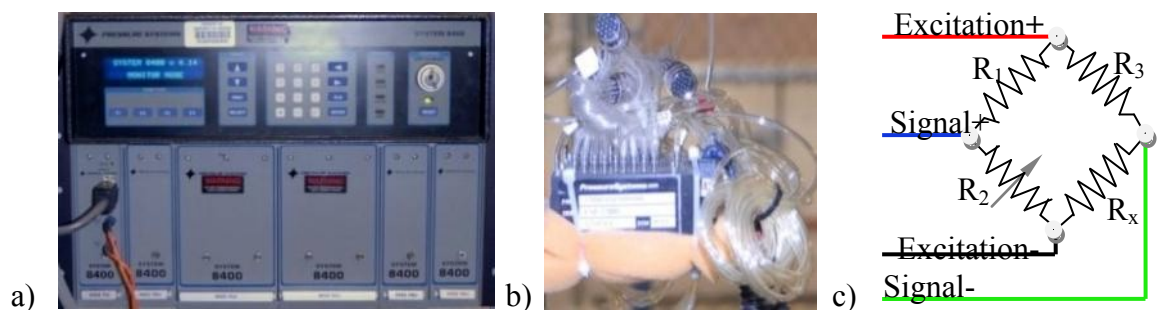


Figure 11. a) The Pressure System in monitoring mode and b) two ESP-32BP pressure scanner modules with four miniature pressure connectors and c) schematic of the Wheatstone configuration piezoresistive scanner dies.¹⁴

2.5.2 Airfoil Dynamic Pressure Measurement System

The dynamic airfoil pressures were scanned electronically with the fast, accurate, and versatile National Instruments (NI) data acquisition (DAQ) PC (NI model PXI-1011 Compact PCI PC). Piezoresistive differential pressure transducers (Endevco model 8507C-1) illustrated in Figure 12 b) were connected to three universal strain gauge amplifier modules (NI model SCXI-1520) with eight channels each that were connected through the NI's A/D card (NI model 6052 A/D) all contained within the PXI chassis. Each Endevco transducer was connected in a Wheatstone bridge configuration inside the SCXI amplifier. The excitation voltage for the Endevco pressure transducers was 10V DC.¹⁵

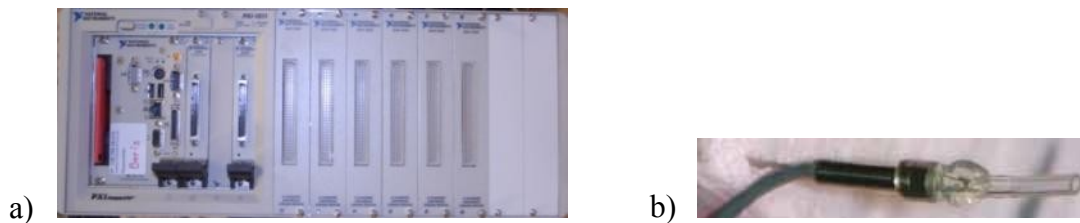


Figure 12. a) The National Instruments PC with 6 available SCXI universal strain gauges and b) one Endevco transducer with polyurethane Tygon tubing adapter ready for integration into the airfoil to replace chosen static pressure ports.¹⁵

2.5.3 U_∞ Measurement

A Pitot-static tube was inserted about two chord lengths upstream of the airfoil shown in Figure 1 a. With help of the Pitot tube, the U_∞ was measured. Due attention was paid to move the Pitot tube out of the test-section's BL in order to measure the true U_∞ . The airfoil measurement ports were outside the disturbance wake generated by the Pitot-

static tube. A differential pressure transducer (MKS Baratron model 698A11TRC) was used to measure the dynamic pressure by evaluating the pressure difference between P_0 and P_s , both measured by the Pitot-static tube shown in Figure 13.¹⁶

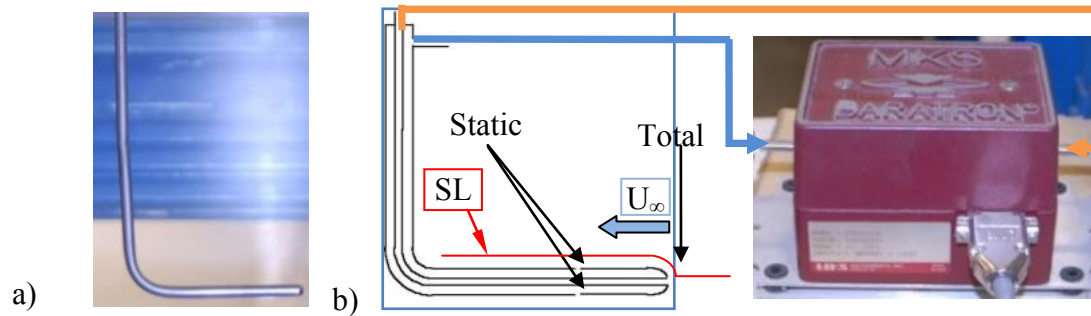


Figure 13. a) Pitot tube with stagnation pressure port at the nose and several perpendicular static pressure ports about 5 cm downstream b) connected to a differential and proportional MKS pressure transducer.¹⁶

2.5.4 Hotwire Velocity Measurement System

A single hotwire and a constant temperature anemometer (CTA) (AA Lab model AN 1003) was used to measure velocities and capture time series. Time series were measured in the airfoil slot exit plane in order to calibrate the ZMF actuation jet momentum, and the wind tunnel test-section entrance planes in order to measure wind tunnel turbulence levels. The single hotwire was made out of tungsten with a thin platinum surface coating to prevent oxidation. It had a diameter of $5\mu\text{m}$ and a resistance of about $3.5\text{-}4.0\ \Omega$ depending on the spacing between the two prongs. A 8-pole Butterworth filter (Krohn Hite model 3386) was utilized when capturing time series information to avoid aliasing frequencies see Figure 14.¹⁷



Figure 14. Equipment necessary for performing hotwire measurements with a) ten channel hotwire & film AA Labs anemometer and b) a 8 Pole LP/HP Butterworth/Bessel filter and c) probe used to measure velocities.¹⁷

2.6 Data Acquisition

The data from the hotwire anemometer and the pressure transducer was acquired using a 16-bit A/D card (NI model PCI 6024E A/D) with a range of ± 10 Volts. The data from the Pressure System was acquired by an interface card (NI model PCI GPIB PC), over an interface cable (Unknown model IEEE 488.2). The NI SCXI PC recorded dynamic pressure time-series data from the piezoresistive Endevcos.¹⁸

2.7 Active Flow Control Devices

Three different flow control methods were applied throughout this study. A centrifugal pump provided continuous blowing and continuous suction. The pump was regulated manually by an autotransformer. For external ZMF actuation, one or two large Domzalski actuators were utilized. Internal ZMF control was provided through seven Domzalski actuators that fit within the airfoil's cavity. A function generator (HP model 33120A) in conjunction with an amplifier (Crown model 3600VZ) provided the excitation signal for both electromagnetic ZMF actuators.

2.7.1 Centrifugal Blower

The centrifugal blower (AMETEK model 117500-12) was only used for external actuation in airfoil. The blower was used for continuous steady actuation by removing or adding momentum through the airfoil's actuation slot depending on whether the slot was connected to the discharge or the suction port of the blower.

The volumetric flow rate was measured with help of a SCFM meter (KING model 7511) see Figure 15 b) with a scale of 10 SCFM – 100 SCFM connected in series between the pump and the airfoil AFC port/ports. An autotransformer (VARIAC model W20MT3) see Figure 15 c) was used to control the pump by varying its output voltage from 0 V – 120 V. The only limitation was the pump motor's maximum load current of 20 Amps. After only moderate operating times the temperature of the pump as well as VARIAC would rise significantly. This problem was solved by routinely switching the devices off to allow them to cool. After long operating hours the actuation air temperature would also rise noticeably, which made it again necessary to switch the pump off until it had time to cool off.¹⁹

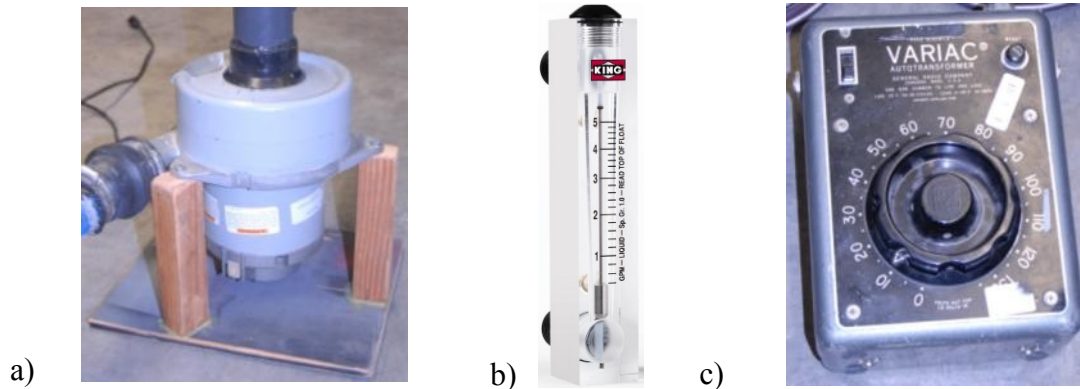


Figure 15. a) Centrifugal pump for continuous “steady” with the upper suction port and the side blowing port b) illustrative of the SCFM meter with a scale from 10-100 SCFM to measure the flow rate and regulate the momentum input into the flow and c) the VARIAC to regulate the pump feed voltage and thereby regulating the rotation speed of the motor that changes the volumetric flow rates.¹⁹

2.7.2 External Domzalski Actuators

The electromagnetic Domzalski actuators build under a contract by Boeing in Mesa were used for the oscillatory flow control cases in configuration A, B and C as seen in Figure 16. One or two actuators were connected to the same ducting that was attached to the airfoil during continuous blowing. In addition, it was essential to have the same length piping connected to both actuation ports on the airfoil to avoid in and out of phase forcing when using two external actuators.

The actuator total coil resistance was 2.8Ω and they operated safely up to 36 Volts AC, if cooled through the pressurized air supply port. The driver coils were of dual coil type and were connected by jumpers to ensure parallel operation. Each coil was connected to a membrane each of which was supposed to operate in parallel. Two ducting variations occurred during experiments. First, one actuator was used on both airfoil AFC

ports. Second, two actuators were used, one on each port, to double the momentum input into the flow.



Figure 16. Large external Domzalski actuator with both forcing coils visible from the side. The right image shows the single forcing port exiting from the top.

2.7.3 Internal Domzalski Actuators

The internal Domzalski actuators were only used in airfoil configuration B, C, and D. One actuator's total coil resistance was 0.9Ω and each one operated safely up to 6 Volt AC shown in Figure 17 a. Seven actuators were connected in series within the airfoil's cavity shown in Figure 17 c. To prevent heat damage to the actuators each actuator was equipped with an aluminum cooling body shown in Figure 17 b that effectively halved the equilibrium temperature reached during maximum power testing conducted outside the airfoils cavity.



Figure 17. a) Domzalski actuator as seen from the top with fixed permanent driver magnet and a coil attached to square composite membrane and b) actuator cooling body and c) the airfoil assembled with 6 of the 7 actuators installed without the cooling bodies as seen from the side

3. EXPERIMENTAL PROCEDURES

3.1 Hotwire Calibration

Before calibrating the single hotwire, it had to be properly initialized. All resistances had to be accounted for from the hotwire, hotwire probe, probe holder, BNC connectors and BNC connection cables. The overheat ratio and hotwire damping had to be adjusted, and the desired dynamic measurement range had to be set. The A/D PC card had a range of ± 10 Volts, which limited the hotwire signal voltage, and therefore the AA Labs anemometer amplification range. The desired hotwire voltage output had to fall between ± 8 Volts to stay within dynamic range. Calibrations were performed with a single hotwire operating at an overheat ratio of 1.5, which measured the jet exit velocity of the calibration test stand blower. The constant temperature anemometer, the hotwire was connected to, operated on the basis that the resistance of the hotwire was proportional to temperature. The hotwire was connected in a Wheatstone bridge configuration to determine the measured voltage drop.²⁰ The calibration was performed with a Pitot tube connected to a Baratron for referencing the hotwire voltage-velocity relationship while being immersed inside the same jet stream. At least ten different voltages needed to be generated resulting in a calibration curve shown in Chart 1. The polynomial was later used to convert experimentally measured voltages from the hotwire directly into velocities using LabView. Thermal drift caused the offset to change frequently. To resolve this issue, and avoid having to recalibrate the hotwire constantly, a multimeter was attached to the AA Lab amplifier output. The multimeter read the hotwire

voltage to monitor the jet velocity. If the value deviated from that recorded during calibration, the offset would be readjusted by the AA Lab range trim pod.

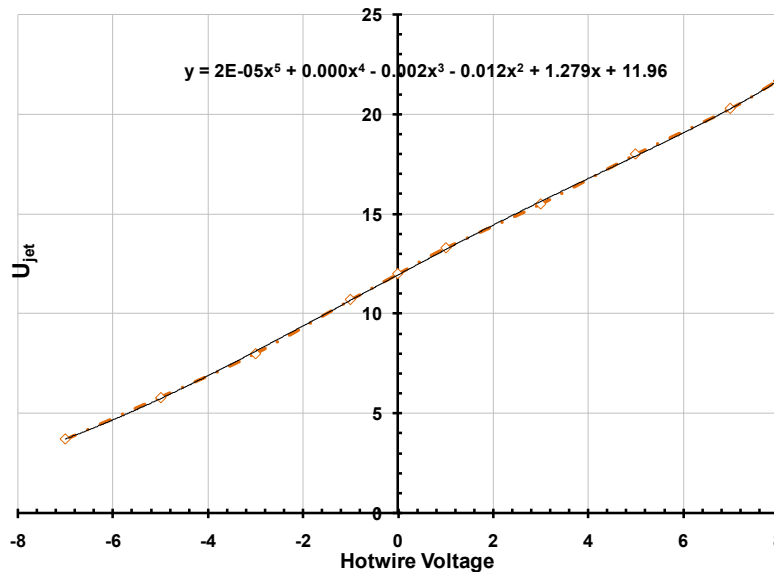


Chart 1. Shows a ten-point calibration curve with U_{jet} vs. $V_{Hotwire}$ with a 5th order polynomial curve fit.

3.2 Pressure System Calibration

The Pressure System consisted of multiple modules, each playing a part in the calibration procedure. The pressure calibration unit (PCU) generated a set of five very accurate calibration pressures, chosen by the user, to reflect the pressures to be measured during experiments. The pressures were fed to the differential pressure scanner modules (Esterline model ESP-32BP), which produced voltage signals proportional to the input pressures. A valve inside the ESP module switched between calibration mode and run mode and was controlled by the SDU. Voltages were acquired by the scanner digitizer unit (SDU) that also converted the analog signals to digital signals, which than were processed by a PC

shown in Figure 18. A pressure-blanking unit zeroed out any excess line pressure after calibration or after measurement runs. The five pressures were chosen as -2000, -1000, 0, 1000, 2000 Pa. The sub-atmospheric pressures were generated with the aid of a Venturi tube attached to the pressure supply.

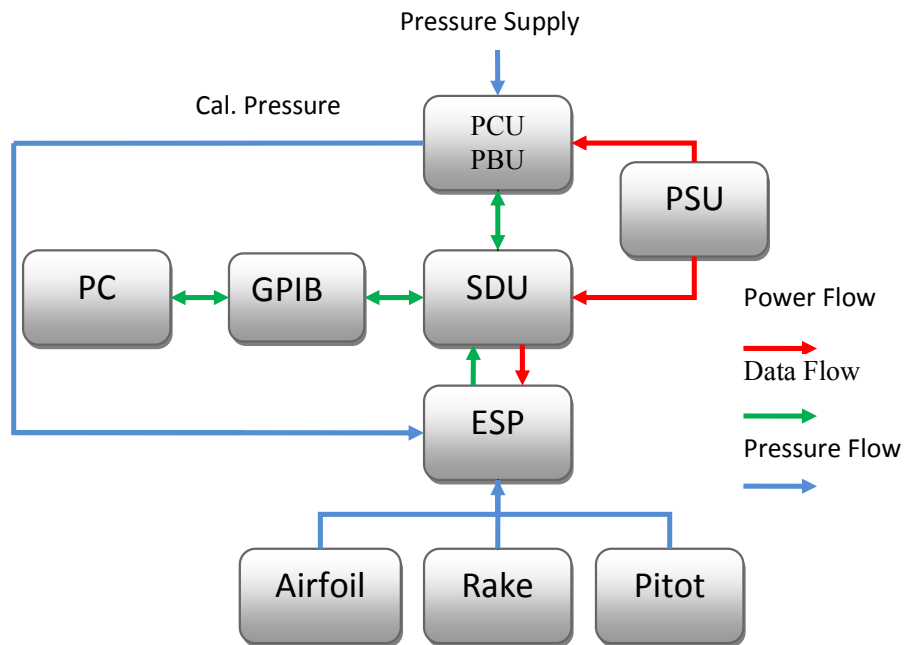


Figure 18. Pressure System flow diagram to better visualize the information flow during calibration and DAQ.

The calibration coefficients were found by fitting a 4th-order polynomial through five measured pressure points. Each die was able to handle a maximum pressure of 6,870 KPa with a typical full-scale accuracy of $\pm 0.08\%$. The polynomial was used to evaluate pressures measured during experiments according to the calibration coefficients shown in Equation (3). Every time the unit was reset, a new calibration was performed. Before beginning the calibration, it was also necessary to wait at least 30 minutes for the electronic

components to warm up after the device had been turned off. For routine measurement checks, the unit was recalibrated every 5 hours. For error corrections due to temperature drifts, a simple re-zeroing procedure was sufficient. By re-zeroing only the zero pressure was applied by the PCU to correct the C_0 offset coefficient and perform a y shift on the polynomial. This was done every 2 hours to compensate for temperature changes in the room and/or the measurement equipment. Room temperature variations of up to $\pm 2^\circ\text{C}$ were common, even with air-conditioning. The temperature changed depending on the time of day and the location of the sun. Piezoresistive dies were very temperature sensitive, which again made frequent re-zeroing necessary.

$$P_x = C_0 + C_1(V_x) + C_2(V_x)^2 + C_3(V_x)^3 + C_4(V_x)^4 \quad (3)$$

P_x = pressure to be measured

C_0 = offset (Pa)+

C_1 = sensitivity (Pa/Volt¹) + C_2 = non-linearity (Pa/Volt²) +

C_3 = non-linearity (Pa/Volt³) + C_4 = non-linearity(Pa/ Volt⁴)

V_x = transducer voltage at P_x

3.3 ZMF Control Actuator Calibration

Slot calibrations were performed in order to quantify the momentum input into the freestream flow during experiments running AFC shown in Figure 19. A calibrated hotwire

was used to determine these relationships. The hotwire was placed into the exit area of the airfoils actuation slot. The membrane displacement of the actuators, all connected in parallel, caused pressure fluctuations within the actuation chamber. The increased pressure within the chamber, for maximum membrane displacement, caused air to accelerate through the slot opening to the lower atmospheric pressure of the lab. At minimum membrane displacement, a sub atmospheric pressure was generated causing the air to rush through the slot into the chamber to fill the void. The air movement in and out of the chamber followed the actuator-forcing signal. The hotwire resistance changed with the amplitude and direction of the slot airflow. The voltage oscillations due to the resistance changes were amplified by the AA box. A low pass filter cut off any frequencies above 2048 Hz to avoid aliasing. The signal was recorded onto a PC in form of a voltage time-series. A A/D PCI card translated the analog input voltages into a digital signal that was processed by a PC. Since the hotwire calibration curve was known the average voltage readout could be directly correlated to an airflow velocity with help of LabView. LabView calculated the mean velocity from the voltage time series. For various excitation frequencies and amplitudes, this procedure was repeated, resulting in a plot of C_{μ} vs. V_{rms} amplitude and frequency of excitation shown in Chart 2. The excitation frequency was changed with the function generator, and the function generators base output voltage was amplified with a secondary amplifier. 2 D checks were performed at 7 measurement locations along the slot to ensure 2 D forcing.

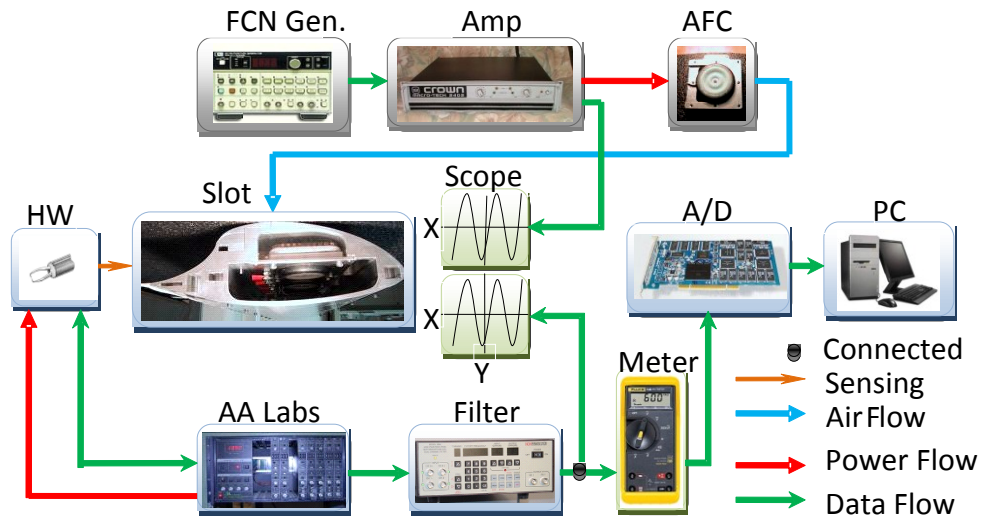


Figure 19. Airfoil slot calibration flow diagram highlighting all the equipment used during calibration and the order in which they were used and in which data was processed.

For configuration A, the slot was calibrated using one external Domzalski actuator connected to both outboard ports on the airfoil. Chart 2 shows the momentum input as compared to the freestream (C_{μ}) vs. the excitation amplitude (V_{rms}). The reference freestream (U_{∞}) was 20 m/s and calibrations were done at various frequencies (F) or correspondingly nondimensional frequencies (F^+). The C_{μ} was based on chord (c), which was 25.16 cm and the slot width (h), which was 0.813 mm. F^+ was based on the characteristic length (L), which was 9.17 cm for the $x/c = 0.693$ slot.

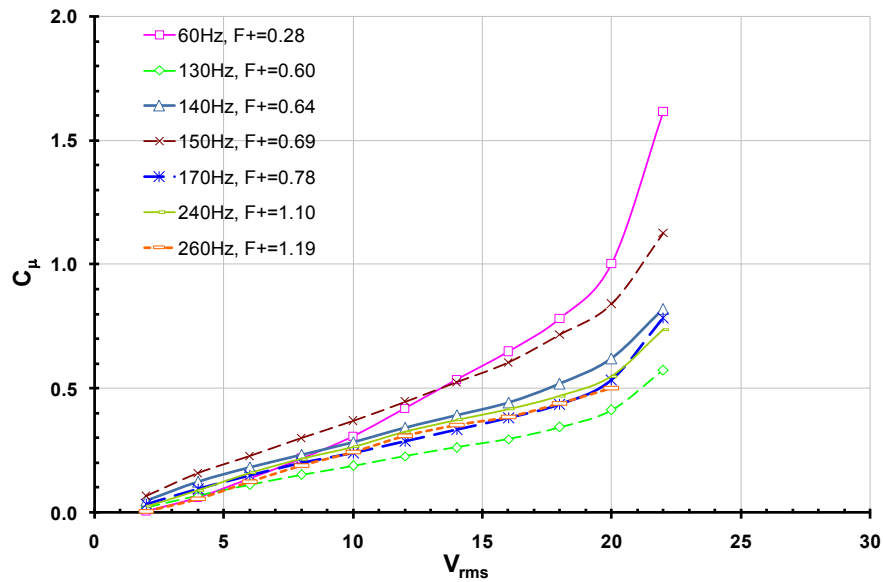


Chart 2. C_{μ} in percent vs. V_{rms} for configuration A and one external ZMF control actuator at 20 m/s. Two outboard slots were taped. $h = 0.813$ mm, $c = 25.16$ cm and $L = 9.17$ cm.

Chart 3 shows C_{μ} vs. F at various V_{rms} . There were three optimum frequencies, 50 Hz, 150 Hz and 250 Hz, at which the actuator provided the highest C_{μ} at the lowest power input. At V_{rms} of 10, 15 and 20, C_{μ} was measured every 10 Hz and all other curves are likely to follow the same trends if a higher frequency resolution would have been chosen.

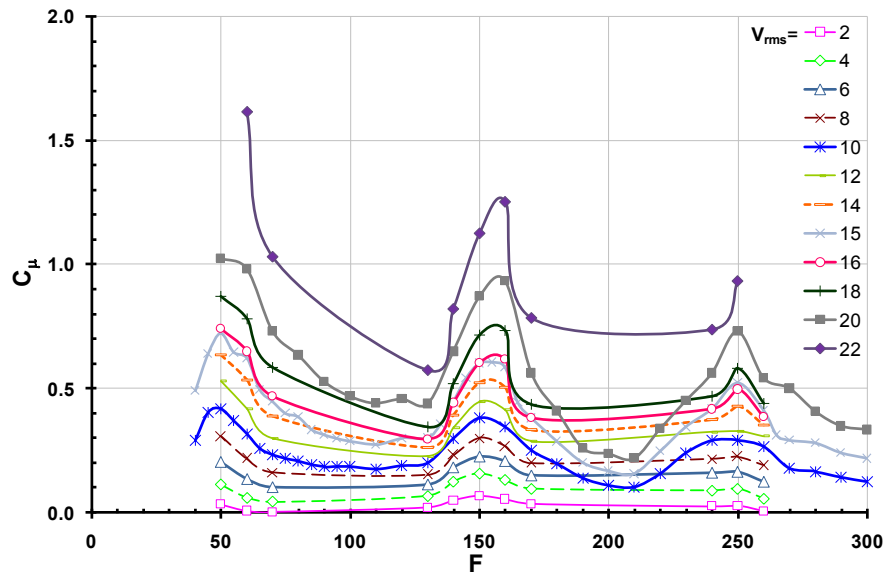


Chart 3. C_μ in percent vs. F for configuration A with one external ZMF control actuator at 20 m/s. Two outboard slots were taped, and $h = 0.813$ mm, $c = 25.16$ cm and $L = 9.17$ cm.

Seven internal Domzalski actuators connected in series were used for slot calibration in airfoil configuration B, C, and D. The assumption was that all actuators worked in tandem providing equal power input at the same time. Chart 4 shows C_μ vs. V_{rms} expected at $U_\infty = 20$ m/s. The C_μ varied linearly with V_{rms} whereas the slope mostly was a function of frequency.

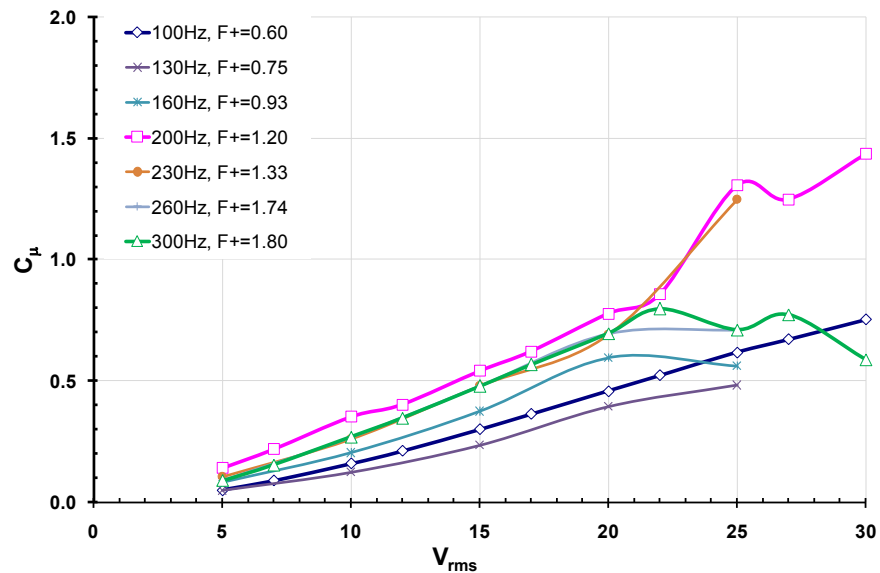


Chart 4. C_{μ} in percent vs. V_{rms} with configuration B,C, and D using internal ZMF actuation at 20 m/s with $h = 0.711$ mm, $c = 25.16$ cm and $L = 11.6$ cm.

Chart 5 shows C_{μ} vs. F for different V_{rms} . At $V_{rms} > 15$ Volts a maximum peak developed in the range of 200 Hz – 250 Hz. This represents the optimum operating frequency range of the actuator for high V_{rms} operation, mostly due to actuator design and built.

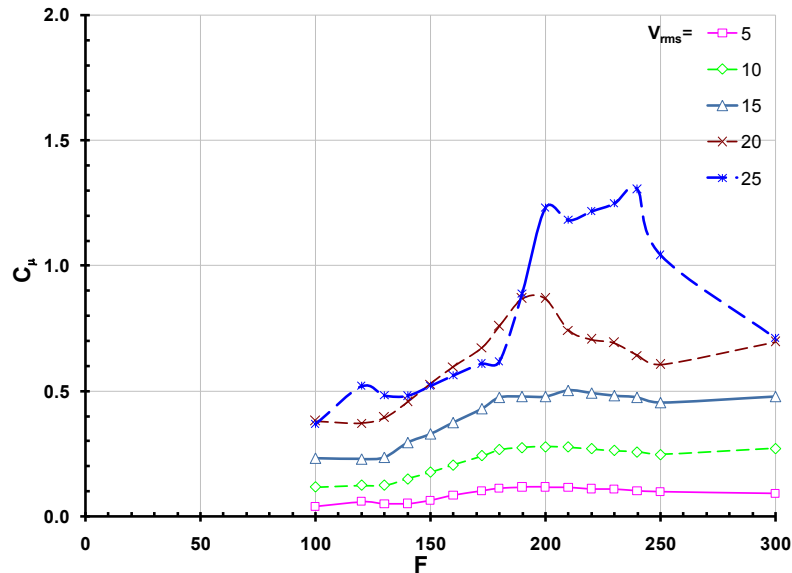


Chart 5. C_{μ} in percent vs. F for various V_{rms} with configuration B, C, and D using internal ZMF control actuation at 20 m/s with $h = 0.711$ mm, $c = 25.16$ cm and $L = 11.6$ cm.

A 2 D check was performed by measuring the U_{rms} jet velocity at seven spanwise slot locations, which corresponded to the center of each actuator slot. The actuation frequency was 100 Hz, and the amplitude was 12 Volt AC, as shown in Chart 6. Under zero freestream influence, the jet exhibited a slight non-uniform spanwise behavior. The lopsidedness tended to the right, with two actuators producing $\sim 20\%$ higher velocities than the rest. Before the calibration, the best 7 out of 12 available actuators were chosen based on experimentally determined membrane displacement characteristics. During this matching process, the actuator membrane displacement was measured at various voltages and frequencies. For various actuators, the membrane also exhibited different instability modes depending on the operating frequencies. All this was taken into account as best as possible. Nevertheless, an uneven distribution resulted.

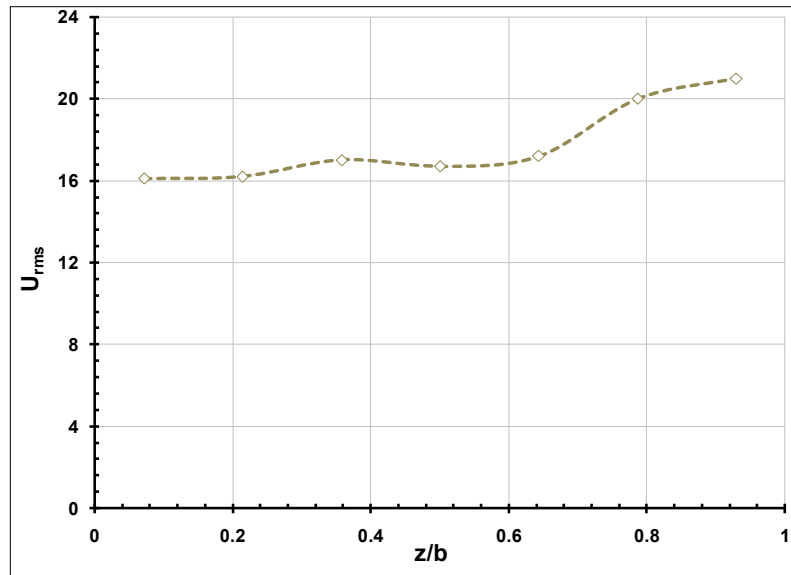


Chart 6. 2 D check with U_{rms} vs. z/b and $b = 60.96$ cm. $F = 100$ Hz and $V_{rms} = 12$ Volts. Seven internal Domzalski actuators in configuration B, C, and D were used.

A 20% variation in U_{rms} was discovered. The variation tended to one side with two actuators producing a larger U_{rms} than the rest. To rectify this in the future it would be recommended to power each actuator separately such that variations could be compensated outside the airfoil with use of a resistor or trim pod. In addition a better slot design might create a more uniform spanwise velocity distribution.

3.4 Continuous Blowing or Suction AFC Calibration

External suction or blowing was used for airfoil configuration A and B in order to add or remove momentum continuously. One external centrifugal blower was connected to both outboard actuation ports on the airfoil. The slot calibration was performed by varying the standard air SCFM and was measured directly with a SCFM meter. A calibrated hotwire was used to find the average jet exit velocity.

For configuration A, two outboard slots were taped. Chart 7 shows the steady momentum coefficient (c_{μ}) vs. SCFM expected at a $U_{\infty} = 20$ m/s. Five measurements of U_{jet} were taken and the average value was utilized to find c_{μ} . For a given SCFM the suction and blowing c_{μ} should be the same. According to Chart 7 this was not the case for SCMF > 20 . Whereas mostly uniform flow exited the slot during blowing, suction caused separation around the slot to occur creating flow nonuniformity and therefore a variation in average U_{jet} measured. The nonuniformity of the jet increased as the SCFM was increased. The blowing c_{μ} matched the one calculated with SCFM only and should in general be taken as the c_{μ} indicator. However, in this research the c_{μ} 's were all taken based on the hotwire calibration.

The readout from the standard SCFM indicator was only accurate within SCFM $\approx \pm 2.5 \frac{ft^3}{min}$ as it sometimes would bob around the desired SCFM value making it necessary to take the average SCFM value. Due to its lack of accuracy as well as lack of resolution, only one measurement was made for every 10 SCFM. After about 50 SCFM, the suction and blowing c_{μ} started to level off after a roughly linear increase of c_{μ} with increasing SCFM. This is again associated with the assumptions made of uniform flow in the slot exit plane when using a hotwire.

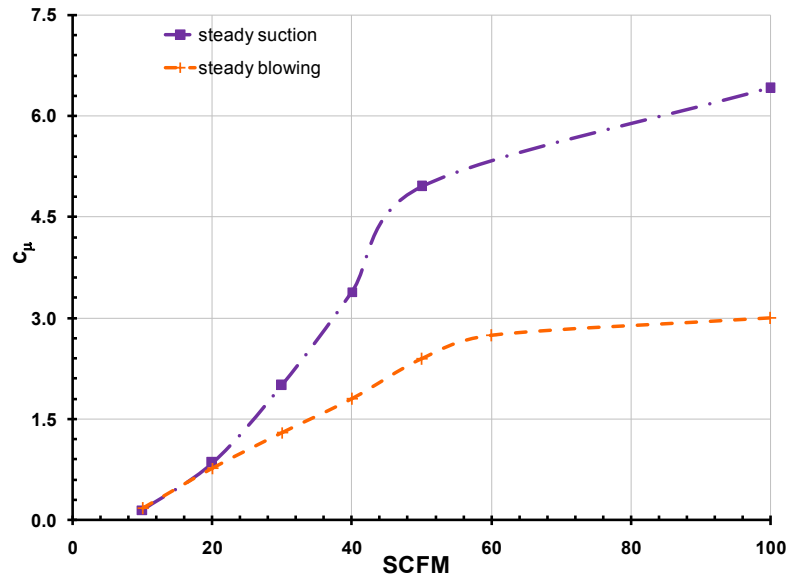


Chart 7. c_u in percent vs. SCFM for configuration A, and B at $U_\infty = 20$ m/s. Slot calibration was performed with a single hotwire at the slot exit. Two outboard slots were taped and one external centrifugal pump was connected. $h = 0.813$ mm, $c = 25.16$ cm and $L = 9.17$ cm.

4. AERODYNAMIC COEFFICIENTS

4.1 Total Drag

The drag force is the net aerodynamic force acting on an airfoil in the direction of the undisturbed freestream flow calculated by Equation (5). In 2 D flow the total drag force is most commonly decomposed into two main components the form or pressure drag and the skin friction drag. Vortex drag is potential, though rarely discussed, contributor to total drag if a steady stationary vortex in the aft region of the airfoil exists. Such a vortex could be caused by a rollup of the separated boundary layer. A thin viscous layer close to the airfoil surface, called boundary layer (BL), is responsible for skin friction drag. A shear force acts on the fluid within the BL decelerating fluid particles until they come to rest at the airfoil surface, satisfying the no slip condition. Since viscous effects within the boundary layer are confined to a very thin region around the airfoil, the Euler equations for inviscid flow still apply outside the BL; the assumption being that streamlines are following the body geometry closely. The C_D is the nondimensional drag. The total drag was divided by a reference pressure and the airfoil chord in order to get the C_D per unit span.

$$C_D = (C_{dp} + C_{df})_{common} + C_{dv} \quad (5)$$

4.1.1 Total Drag Calculations

The one and only reliable way to measure the GLAS II C_D directly was by measuring the momentum deficit across the airfoil caused by frictional, pressure, and

other losses. A rake with 16 total pressure tubes was inserted into the wind tunnel about three chord lengths downstream of the airfoil's TE and perpendicular to the freestream shown in Figure 1 and Figure 3 and was traversed in the y direction for wake DAQ and positioning. Two additional static pressure measurement tubes were placed symmetrically around the center of the rake outboard of the total pressure tubes.

A classical control volume approach was chosen encompassing the airfoil, the rake location, and the upstream Pitot tube location are shown Figure 20. It was assumed that streamlines ab and hi are far above and below the body, and perpendicular lines ai , and $bc-gh$ are far ahead and behind the body and that the control boundary hugged the airfoil surface closely such that streamlines followed the curvature of the airfoil perfectly. Because the streamlines ab and hi were far away from the body the pressures were assumed equal everywhere to the atmospheric pressure. Any forces on cd were equal and opposite to gf and would cancel each other out. Shear and pressure forces on def were the same as those generated by the flow on the surface of the body. The only contributions came from ai and bh .²¹ The momentum into the control volume due to the freestream was subtracted by the momentum out of the control volume measured by the rake in Equation (6). In addition, using continuity Equation (7 a) one arrives at Equation (7 b).

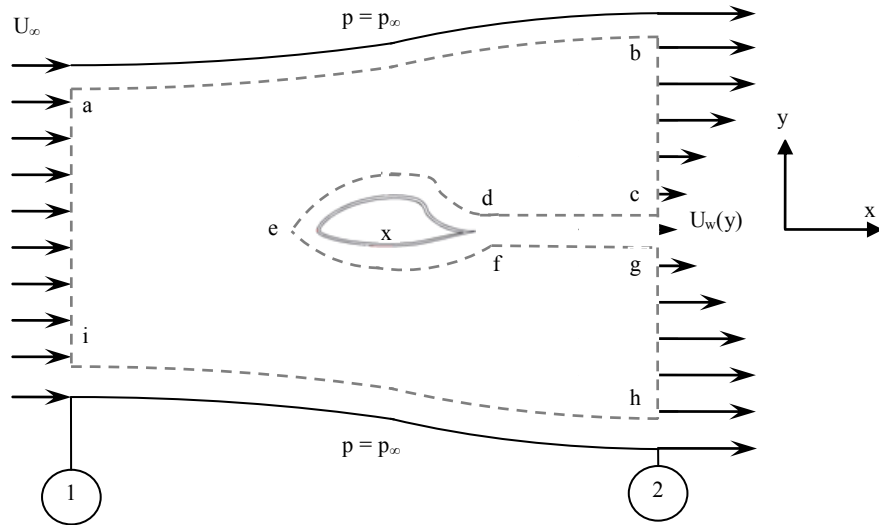


Figure 20. CV analysis applying Newton's second law to a steady, inviscid flow with no body forces.²¹

$$D' = \iint_S (\rho \vec{V} \cdot d\vec{S})u = \rho \left(\int_h^b (U_w(y))^2 dy - \int_i^a U_\infty^2 dy \right) \quad (6)$$

$$\text{a) } \rho U_w d_{y2} = \rho U_\infty d_{y1}, \text{ b) } D' = \rho \int_h^b U_w(y)(U_\infty - U_w(y)) dy \quad (7)$$

Any static pressure differences across the rake were averaged over the two static pressure tubes of the rake. The U_∞ at the rake was measured locally through total pressure tubes and static pressure tubes that resided outside the airfoil wake. Local U_∞ was used to normalize deficit velocities in the wake. These were calculated with help of the Bernoulli

equation. Total and static pressures were converted into dynamic pressures and knowing the density into local velocities seen in Equation (8).

$$\text{a) } P_0 = q + P_s \quad \text{b) } q = \frac{1}{2} \rho U^2 \quad \text{c) } U = \sqrt{\frac{2}{\rho} (P_0 - P_s)} \quad (8)$$

Caution was at place because the airfoil wake was turbulent and its' center changed its' y location depending on lift and incidence. It was necessary to monitor the wake and make sure it would not interfere with the local freestream pressure measurements. Another approach to finding the total drag on an airfoil was used to check the classical derivation. Betz and Jones had developed correction schemes because experimentalists measured wakes less than one chord-length downstream of the body. Static pressure differences had to be taken into account because the previously developed technique assumed a rectangular control volume where the upstream and downstream width is the same. This resulted in the conservation of mass-flux being equal to the mass-flux out of

$$h_1 = \int_{-\infty}^{\infty} \frac{U_w(y)}{U_\infty} dy \quad (9)$$

the control volume leading to Equation (9).

Solving the equation for h_1 gave the height of the control volume at station one. With knowledge of the entrance height the momentum change could be calculated and with the change in momentum the drag on the airfoil. Normalizing by q_∞ and dividing by

the chord of the airfoil gave the resulting total pressure drag coefficient shown in Equation (10) that was equal to the classical drag except for the normalization.

$$C_D = \frac{D}{\frac{1}{2}\rho U_\infty^2 c} = \frac{(\rho U_\infty^2 h_1) - \left[\rho \int_{-\infty}^{\infty} (U_w(y))^2 dy \right]}{\frac{1}{2}\rho U_\infty^2 c} = \left[\frac{2}{c} \int_{-\infty}^{\infty} \frac{U_w(y)}{U_\infty} \left(1 - \frac{U_w(y)}{U_\infty} \right) dy \right] \quad (10)$$

Drag forces due to a static pressure drop given by Equation (11) across the airfoil were not considered in the calculations or measurements.

$$D_s = P_{s1} \cdot h_1 - \int_{-\infty}^{\infty} \Delta P_{sw}(y) \cdot dy \quad (11)$$

Wake pressure data was only known at 16 discrete locations without wake refinement. For data acquired in within the Scobee tunnel in 2007 wake refinement was done. Trapezoidal integration was performed to calculate the velocity deficit. Summation started at a relative zero y for the first total pressure tube marching in $\Delta y = 25.4$ mm increments for subsequent pressure tubes and ended with the last pressure tube at $y = 381$ mm.

4.1.2 Pressure Drag Calculations

According to thin airfoil theory, the form drag had to be determined by integrating the streamwise component of pressures read by the surface pressure taps distributed along the surface of an airfoil. Thin airfoil theory applied for small variations in dz/dx , hence

only slight thickness and camber. Because the GLAS II was 31.5% thick and had large camber thin airfoil theory could only give an approximation of the C_{dp} . In addition, it was shown during experiments that the flow within the ramp region exhibited 3D behavior and the simplified 2 D Euler equations would possibly break down within the ramp. The 2D check pressure taps within the ramp at 79.6% chord measured variations in spanwise pressures, e.g. at 7 m/s and suction the spanwise pressures at $\alpha = 3^\circ$ varied up to 10.5% with an average variation of 5.5% over the entire range of alphas. At 20 m/s baseline and $\alpha = 6^\circ$ the pressures varied up to 21.9% with an average variation in the range $0^\circ < \alpha < 8^\circ$ of 13.5%. Again, C_{dp} estimates should be considered with a grain of salt. The ΔC_p was measured between every two sequential pressure taps and was decomposed into a streamwise component ΔC_{dp} and a perpendicular component ΔC_L . In order to get ΔC_{dp} , the ΔC_p was multiplied by the sine of the local surface inclination angle plus the angle of attack. The local surface inclination angle was found by taking the tangent of Δy over Δx from one tap to the next seen in Equation (12) and Figure 21. This procedure was repeated across all taps starting from the LE of the airfoil continuing clockwise to the TE and then continuing all the way around back to the bottom surface (BS) LE of the airfoil.

$$\Delta C_p = C_{i+1} + C_i \quad (12)$$

$$\Delta C_{dp} = (C_{i+1} + C_i) \times \sin(\theta \pm \alpha)$$

$$\theta = \tan^{-1}\left(\frac{\Delta y}{\Delta x}\right) = \tan^{-1}\left(\frac{y_{i+1} - y_i}{x_{i+1} - x_i}\right)$$

$$\text{Trapezoidal - Rule} = \int_b^a f(x) dx = \sum_{i=1}^n \frac{h}{2} \cdot (f(a + (i-1)h) + f(a + ih))$$

$$f(a + (i-1)h) + f(a + ih) = (C_{i+1} + C_i) \times \sin\left(\tan^{-1}\left(\frac{y_{i+1} - y_i}{x_{i+1} - x_i}\right) \pm \alpha\right)$$

$$h = x_{i+1} - x_i$$

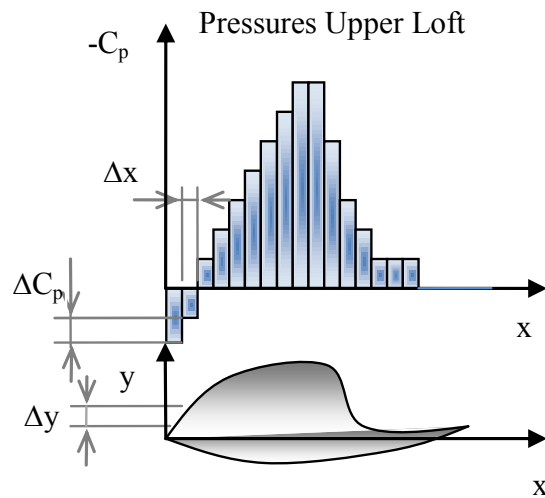


Figure 21. Schematic of upper loft pressure signature to illustrate usage of trapezoidal integration of pressures measured by the Pressure System.

4.2 Lift Calculations

The lift can be found in a similar manner as previously illustrated for the pressure drag. The measured ΔC_p 's vertical component constitutes lift or ΔC_l and can be found by multiplying the C_p by the cosine of the local surface inclination plus the global angle of attack. To illustrate the decomposition see Figure 22.

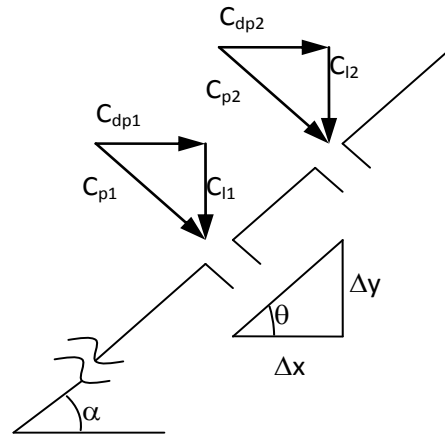


Figure 22. Lift and drag components of pressure force for two taps on an airfoil with local surface inclination angle and global angle of attack of the airfoil.

4.3 Moment Calculations

The quarter-chord moment calculations follow from the C_{dp} and C_L calculations illustrated in the last two sections with the addition of C_l and C_{dp} now being multiplied by the moment arm or the distance from the discretized area upon which the pressure force acts to the quarter chord location of the airfoil.

5. ERROR ESTIMATIONS

5.1 Combined Error

During experiments various pressure and/or velocity measurement devices were employed together or by themselves. A total error resulted with each device contributing its own combination of errors. A detailed analysis of the combined error will not be pursued at this point but a rough estimate of the maximum possible error for each device will be given.

5.2 Instrumentation and Resolution Errors

Resolution error or instrumentation read off error was defined by half the measurement device's smallest scale increment. Instrumentation errors were defined as absolute error for given input signal. Full-scale error was according to the maximum allowable input signal. Full-scale output error was defined as a relative error depending on the input signal amplitude. All following errors pertain to amplitude errors only and do not consider phase or other errors.

5.2.1 U_∞ Measurement Errors

The wind tunnel U_∞ was calibrated using a Pitot tube in a velocity range of 7 m/s to 30 m/s roughly equal to a pressure difference range of 0.22 mmHg to 4.08 mmHg. The Baratron connected to the Pitot tube had a $\pm 0.08\%$ read-error as specified by the manufacturer. This read-error generated an experimental full-scale error of ± 0.0033 mm Hg or $U_\infty = \pm 0.85$ m/s.¹⁶ The same Baratron model was used in Davis wind tunnel and Scobee tunnel experiments. Another contribution to U_∞ error came from the measured

density in the lab. Using a lab manometer/thermometer in the graduate lab (Sargent Welch model S-4519) and a manometer/thermometer in the Undergraduate lab (Wallace and Tiernan model FA160) the density was calculated using perfect gas law. With a density resolution error of $\pm 0.017 \text{ kg/m}^3$ due to instrumentation in the graduate lab the test-section velocity could deviate with an experimental full-scale error of $\pm 0.236 \text{ m/s}$. In the Undergraduate lab, the density resolution error found was $\pm 0.00823 \text{ kg/m}^3$ due to instrumentation the test-section velocity could deviate with an experimental full-scale error of $\pm 0.117 \text{ m/s}$. Total maximum expected error in U_∞ due to instrumentation was around 1.09 m/s not including errors due to temperature and pressure variations during the experimental runs. Remembering that the C_p measured was the pressure difference measured over the dynamic pressure measured shown in Equation (13), it became clear that the freestream error had little effect on C_p , and hence on C_L , C_{dp} , and $C_{mc/4}$ results.

$$C_p = \frac{P_\infty - P}{\frac{1}{2}\rho U_\infty^2} = \frac{P_\infty - P_s}{(P_o - P_s)_{ref}} \quad (13)$$

5.2.2 Static Aerodynamic Coefficient Amplitude Errors

The C_p 's around the airfoil, which determined C_{dp} , C_L , and $C_{mc/4}$ did not vary with U_∞ , but with α and AFC case run during experiments. Pressure ports close to the slot of the airfoil often experienced much larger pressure gradients during AFC compared to the other transducers around the airfoil especially during continuous AFC at large C_μ 's. The worst-case range was roughly specified and the error from the PSI ESP modules was

determined to get a feeling for the maximum instrumentation error possible to have been experienced during measurements. The airfoil pressures, experienced by the transducers, fell within - 675 Pa to 520 Pa. The usual accuracy of a 6.9 KPa PSI scanner was not expected to exceed its full-scale error of $\pm 0.08\%$. Hence, the maximum instrumentation error in full-scale output (FSO) in pressures measured was of the order ± 5.5 Pa.¹⁴ Additionally sampling error was introduced with the ESP and Baratron transducers and their dependency on sampling frequency, number of data sets, and sampling time. The PSI incorporated a convergence subroutine that increased sampling time and number of data sets until convergence was reached. In other words if the variation in measured averaged pressure with addition of a new data set fell below a predefined threshold the data was converging. This feature was not available for the Baratron, or the Endevcos and a sufficiently long data acquisition time had to be chosen to get the desired accuracy within the averaged data.

5.2.3 Unsteady Aerodynamic Coefficient Amplitude Errors

Fifteen Endevco pressure transducers installed in configuration C and D. measured time sensitive data. According to the manufacturer the combined maximum non-linearity, non-repeatability, pressure hysteresis error was $\pm 1.5\%$ of FSO or ± 10.1 Pa.¹⁵ Endevcos directly replaced several static pressure taps that beforehand were used for gathering data through the PSI. Thus, were being exposed to the same pressure differences as the ESP transducers. With a maximum absolute pressure difference measured on the airfoil of - 675 Pa, the error introduced by the Endevco would be ± 4.5 Pa. Nevertheless, the

Endevco's nominal voltage output was so low that most of the instrumentation error was introduced by signal amplification through the SCXI strain gauge module. At a - 675 Pa differential pressure one Endevco would generate 19.7 mV. According to the SCXI manual because of signal amplification and conditioning at a nominal signal range of ± 18 mV and an amplification of 420 the strain gauge would produce an absolute error of ± 2.04 mV or ± 10.4 % of the differential pressure measured.²² The largest combined error at - 675 Pa would be ± 80.3 Pa. Another large source of error came from electrical noise picked up through the 7 m long connection cables due to lack in proper shielding and grounding. It was determined that the Scobee tunnel was not properly grounded and a source of large amplitude and high frequency electrical noise seriously affecting Endevco measurements. This was partially resolved by properly grounding airfoil, connection cables, and NI PC box and by avoiding ground loops. High frequency electrical noise was reduced significantly. From this simple error analysis it became clear that an Endevco was not as accurate as the Baratron or the ESP transducer and that the error had to be monitored closely. With a resonance frequency of 50,000 Hz Endevcos perform excellently were dynamic data is required but they do not provide the static accuracy desired for lift, drag, and moment calculations.

5.2.4 Hotwire Measurement Errors

At least three sources for this type error were quantified for all hotwire velocity measurements. One error came from the NI DAQ A/D card itself that converted the analog signals into digital ones. An absolute full-scale error was specified by the

manufacturer of ± 20 mV at a nominal input range of ± 10 Volt.¹⁸ Using the calibration polynomial for the external continuous AFC case that generated the large jet velocities the velocity error solely by the A/D card was roughly ± 0.026 m/s or 0.1% of the measured full-scale. The AA Lab hotwire anemometer had an absolute accuracy of 0.1%, which equaled to a velocity read-error of ± 0.026 m/s for the continuous external AFC case. The combined error would be ± 0.052 m/s. By far a much larger contribution to error was due to thermal drift, oxidation buildup, and dirt/dust on the wire. Oxidation buildup and dust/dirt had to be cleaned off the wire regularly by flushing the wire with Acetone while the hotwire was turned off. Thermal drift in the instrumentation and the wire was compensated for effectively by knowing the output voltage at a corresponding average reference velocity and adjusting the offset manually through a trim potentiometer located on the AA Lab anemometer panel. Variations in velocity, due to thermal drift, rose up to 8% of the full-scale experimental value in one hour and offset had to be closely monitored with the help of a multimeter connected to the anemometer output.

5.2.5 Other DAQ Errors

Other errors included maximum angle of attack resolution errors of $\pm 0.5^\circ$. Numerical errors introduced into aerodynamic coefficients when integrating pressures with the trapezoidal rule of roughly ± 0.5 %. Errors in measurements caused by fluctuations in the equipments' power supply voltage that had not been quantified. Thermal drift caused error between equipment calibration and re-zeroing procedures due to changes in laboratory temperature that had not been quantified. Errors due to leakages

in Tygons connected to pressure taps or reference pressures that had not been quantified. Errors were also introduced due to short averaging times and small sample sets as well as improperly defined convergence parameters within the hardware parameters of the PSI system. Finally, amplitude errors in aerodynamic coefficients by removing taps on the airfoil located within large pressure gradients; tape before and/or after pressure taps, which changed the pressure reading locally, and erroneous pressure readings close to the slot exit that none of which had been quantified.

5.3 Aerodynamic Errors

Various aerodynamic errors were introduced as well depending on streamline curvature, pressure hole alignment and/or geometry, freestream flow angle/turbulence and BL properties.

5.3.1 Freestream/Test-section Angularity

The flow across the entire wind tunnel test-section was not uniform within the Davis wind tunnel and could vary as much as 2%. The flow within the Scobee tunnel test-section cross section was uniform within 1%. The test-section itself within the Davis wind tunnel was difficult to align with the rest of the tunnel nozzle because the nozzle walls were starting to warp and deform being made of thin high-density plywood.

5.3.2 Pitot-Static Pressure Measurement Errors

Errors were introduced by incorrect pressure readings, caused by the disrupted or modified airflow around the Pitot-static tube. The pressure read-errors depended on

incidence of the Pitot-static tube with respect to the freestream flow streamlines and the type and strength of upstream flow disturbances. The flow streamlines had to be parallel to the Pitot-static tube's pressure holes in order to arrive at the true static pressure reading. If the streamlines were curved there would have been a dynamic pressure component in addition to the static one measured by the static pressure tap. This would result in an absolute velocity reading that would be smaller than expected. In order to minimize that error the static pressure holes had to be placed in undisturbed flow and aligned perpendicular to the flow. The Pitot-static tube used during the experiments had several of these ports located around the circumference, thereby ideally cancelling the effect of streamlines at incidence. The Pitot-static tube was also well outside the wind tunnels BL minimizing turbulent disturbances.

5.3.3 Airfoil Tap Static Pressure Read - Error

This type error introduced flawed pressure readings at the tap. The error was caused by introductions of variations in local tap geometry and/or roughness near the tap hole. Ideally, to achieve low error, the pressure tap hole needed to have a certain geometry as illustrated in Figure 23 a) with a smooth surface around the hole. In this case the static pressure reading is equal to P_∞ . The assumption was made that the streamlines are parallel to the tap surface. In b) the flow will expand over the burr and a lower pressure than P_∞ is read as a result. In c) the flow will be slowed down in the tap region resulting in a pressure reading greater than P_∞ . In d) added roughness can have a similar effect as the burr did. In this case it retarded fluid motion increasing the local pressure reading

resulting in $P_s > P_\infty$. This happened during experiments when roughness was applied close to the tap either upstream or downstream through a roughness strip.

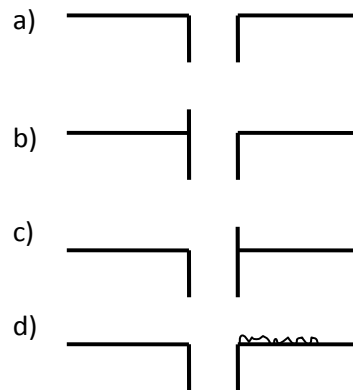


Figure 23. a) Ideal airfoil pressure tap geometry measuring the correct P_s b) upstream burr decreasing P_s c) downstream burr increasing P_s d) downstream roughness with similar effect as downstream burr on P_s .

5.3.4 Static Pressure Error in Wake Measurements

From Section 4.1.1 several assumptions were made in order to calculate C_D . Wake ΔP 's were normalized with the locally measured q . A uniform distribution was assumed across the wake. Due to large airfoil camber, thickness, and large α 's, the P_s 's could vary up to 10% across the wake. A static pressure gradient existed across the entire wake with larger drop in P_s on the TS side than on the BS side of the airfoil. A linear curve fit could have been employed to properly determine each dynamic pressure measured by the Pitot rake tubes. The overall difference in P_s perpendicular to the flow across the test-section on average did not exceed 2%. Due to code development-time limitations, the curve-fitting algorithm, to compensate for the static pressure gradient, was neglected.

5.4 Post Processing Analysis Read – Error

This type error occurred when connecting the experimental data points by curve fitting the data using a 3rd degree polynomial fit through Microsoft Excel. Any information in between data points was useful to garner trends not exact quantitative information. A smooth polynomial curve fit was chosen because it better represented historical results from Glauert and Salter who had also been smoothly curve fitted their data.

6. RESULTS AND DISCUSSION

6.1 Baseline Results

Tests were executed on a clean and tripped airfoil to establish baseline performance and compare it to historical results. Reynolds numbers (Re's) varied from 117,000 to 560,000 corresponding to approximate freestream velocities of 7 m/s to 40 m/s.

6.1.1 Baseline Re Sweep Clean

The clean baseline was analyzed at Re = 112K, 196K, 320K, and 480K shown in Chart 8 with airfoil configuration C within the Scobee tunnel using the splitter plate setup (added contraction). The maximum lift coefficient (C_{Lmax}) for Re = 112K was 1.5. C_{Lmax} decreased from 1.5, 1.45, 1.45, to 1.35 with increasing Re = 112, 196, 320, and 480K respectively. The lift curve slope $\left(\frac{dC_L}{d\alpha}\right)$ for Re = 480K was 0.08, lower than the common 0.111 for thin airfoil theory and much lower than should be ideally expected from a 30% thick airfoil. For a more detailed discussions on $\frac{dC_L}{d\alpha}$ refer to Section 6.1.5 and 6.1.3. . There was a rise in $\frac{dC_L}{d\alpha}$ except at Re = 480K. At Re = 112K the change was most dramatic at angle of attack (α) of 25°. The airfoil went from a fully laminarly separated state to a partial and turbulently reattached state in less than one degree. For a detailed discussion and a look at the pressure (C_p) distributions at fixed α , refer to the following Section on Re dependence. The stall angle (α_s) decreased with increasing Re's.

For $Re = 480K$ the drag coefficient (C_D) was 0.05 with only minor changes due to α . For $Re < 480K$ the C_D first increased up to a maximum and then decreased again up to a second minimum. At $Re = 112K$, $196K$, and $320K$ C_D increased progressively with increasing α in the ranges from $12^\circ - 22^\circ$, $0^\circ - 10^\circ$, and $0^\circ - 4^\circ$ respectively. This was believed to be due to progressive laminar separation at low Re 's. A gradual C_D decrease followed when further increasing α . This was possibly caused by transition and enhanced turbulent reattachment. Hence, C_D was strongly dependent on α and Re . For $Re = 112K$ and $196K$ C_D was much larger compared to higher Re 's. The drag increased with increasing α for lower Re 's, which signified the existence of laminar separation on the airfoil.

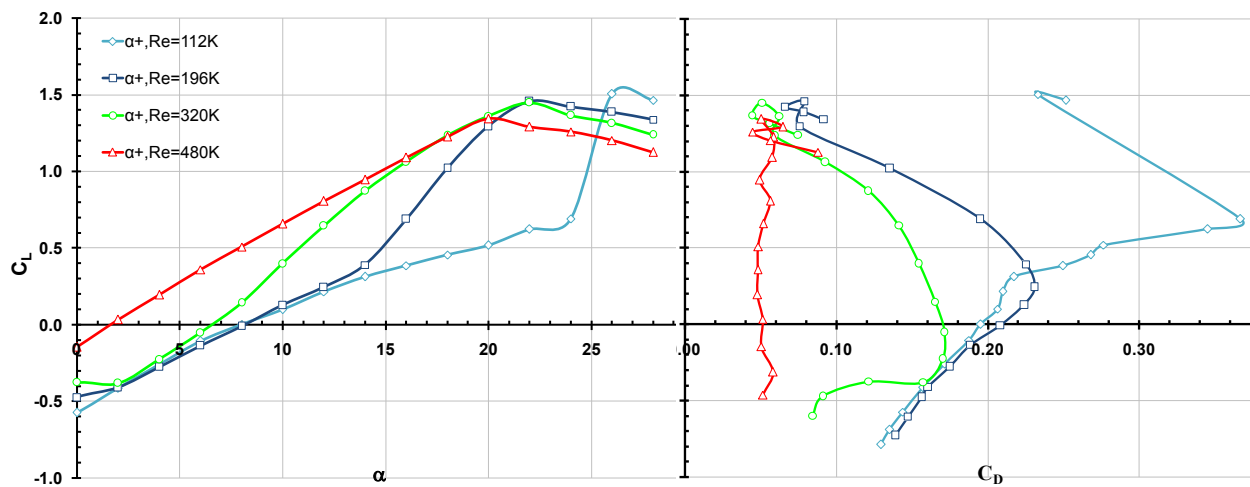


Chart 8. Baseline study of C_L vs. α and C_D at 7 m/s, 12 m/s, 20 m/s and 30 m/s for a clean airfoil with open slot and $\Delta\alpha = 2^\circ$ from 0° to 26° . The airfoil in configuration C with lower contraction was used.

The clean baseline L/D vs. C_L and α is shown in Chart 9. L/D is a crucial parameter in determining the range and endurance performance of an aircraft. If the L/D could be

increased it would increase the range and/or endurance of an aircraft equipped with a modified GLAS II type airfoil after accounting for loss in lift due to tip vortex and increase in C_D due to addition of induced drag.

Maximum 2D L/D , (L/D_{\max}) , = 30, 28, 22, 6 was reached at $Re = 480K$, 320K, 196K and 112K respectively. This was a very poor performance for an airfoil, which made this airfoil an excellent candidate for AFC. In contrast, modern glider airfoils can reach L/D 's ≈ 120 without AFC.

In order to improve range and loiter, the goal would be to improve L/D performance by decreasing C_D , thereby avoiding the increased induced drag that goes with C_L^2 . For improved landing performance, a high C_L would be necessary and a large increase in induced drag would be acceptable because the lower the landing speed of an aircraft the shorter the runway. Another important benefit of increasing C_L and C_D during landing would be a reduction in flap area, weight, and complexity, in return, increasing range, loiter, and/or passenger capacity. The same that was true for landing holds true for takeoff with the additional caveat that a larger C_L is needed during takeoff and that C_D preferably should be lower.

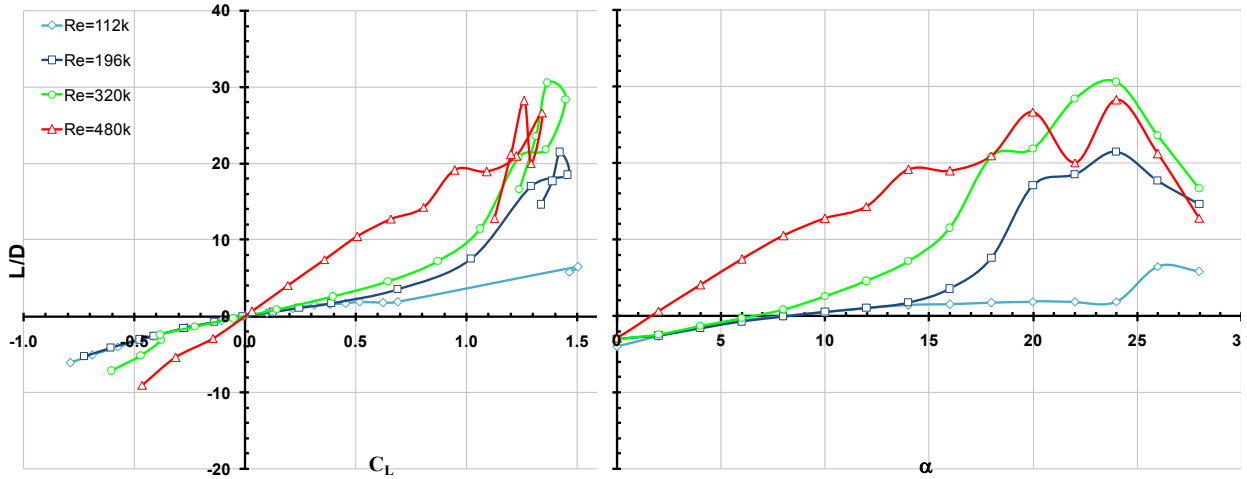


Chart 9. Baseline study of L/D vs. C_L and α at 7 m/s, 12 m/s, 20 m/s and 30 m/s for a clean airfoil with open slot and $\Delta\alpha = 2^\circ$ from 0° to 26° .

There appeared to be a strong Re dependent behavior on airfoil L/D especially below $Re = 480K$. For $Re = 480K$ $\frac{dC_L}{d\alpha}$ showed a linear trend compared to the nonlinear trends at lower Re 's. Laminar separation seemed to occur at $Re = 112K$, $196K$, and $320K$ followed by transition and turbulent reattachment.

6.1.2 Re Dependence for Clean vs. Tripped Airfoil

The Re dependence of the airfoil was analyzed further at a fixed $\alpha = 14^\circ$ and 18° with airfoil configuration C in the Scobee tunnel using the added contraction described in Section 2.1.2. Re vs. C_L and C_D is shown in Chart 10 for a clean and a tripped airfoil. For the clean airfoil, the C_L became independent of Re at $Re > 400K$. The C_D for the clean airfoil became independent at $Re > 500K$.

V-tape roughness shown in Figure 24 a) was used for tripping at upper loft (TS) locations of $x/c = 0.36$ and 0.55 . The roughness strips were 12.4 mm wide and 0.27 mm thick. V-letters were 0.18 mm high, 3.65 mm wide and 4.51 mm long. Vortex generators (VG's) shown in Figure 24 b) were used to introduce streamwise vortices within the ramp at $x/c = 0.75$ to improve mixing and minimize recirculation. VG's were fixated on double-sided tape that was 12.4 mm wide and 0.08 mm thick. VG's were ~ 2.6 mm high, ~ 8.6 mm long, and placed 13.3 mm apart at an angel of $\sim 30^\circ$ to the flow.



Figure 24. a) V-roughness strips were applied along the airfoil span (b) at 36 % and 55 % chord and b) vortex generator strips were placed within the ramp at 75% chord along b.

For the tripped airfoil case Re was first increased, noted by Re^+ , and then decreased again, noted by Re^- . C_L and C_D independence on Re occurred sooner for Re^+ at $Re > 240K$. For Re^- C_L and C_D independence on Re occurred at $Re > 320K$. For more detailed effects of sand roughness on airfoil coefficients, see Section 6.1.8. For further discussion on lift and drag ($C_L \setminus C_D$) hysteresis, refer to Section 6.1.6. There was slight $C_L \setminus C_D$ - hysteresis due to increasing vs. decreasing Re 's.

For the tripped airfoil, the C_L and C_D independence on Re occurred sooner for Re^+ at $Re > 240K$ for. For Re^- the C_L and C_D independence on Re occurred at $Re > 320K$.

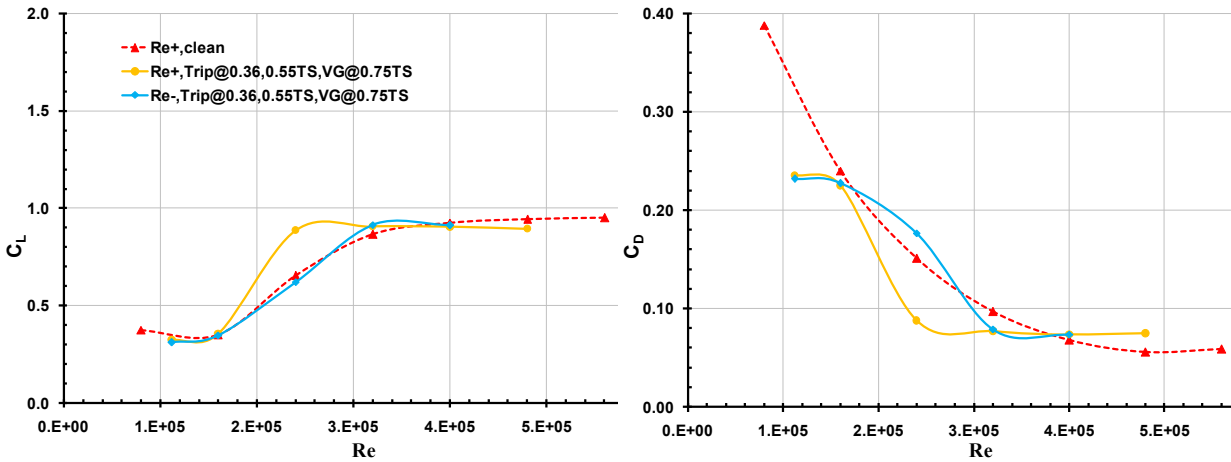


Chart 10. Baseline study of C_L and C_D vs. Re at $\alpha = 14^\circ$ with a clean and tripped airfoil in configuration C using the lower contraction.

The C_p distributions for $\alpha = 14^\circ$, 16° and 18° were compared in Davis wind tunnel experiments at $Re = 112K$, $235K$, and $352K$ shown in Chart 11 in order to investigate Re dependent C_L variations. Symbols representing pressure taps on the TS were open while the ones' on the BS were full. The airfoil configuration B was used and the slot was taped.

A horizontal line in the C_p distribution was indicative of laminar separation or the existence of a laminar separation bubble (bubble). The bubble on the TS, at $\alpha = 14^\circ$, moved downstream from $x/c \approx 0.30$ to 0.44 between $Re = 235K$ and $352K$. A similar trend was noticed at $\alpha = 16^\circ$ with a downstream bubble displacement from $x/c \approx 0.32$ to 0.44 between $Re = 235K$ and $352K$. At $\alpha = 18^\circ$ the $Re = 235K$ bubble jumped to $x/c = 0.44$ the same location of the $Re = 352K$ bubble. This illustrated the difficulty in getting repeatable results due to sensitivity to Re and α on TS bubble location.

The trend towards a laminar separation bubble was also seen on the BS at $x/c \approx 0.06$, which was independent on Re or α .

The stagnation point in a C_p distribution was identified by the tap measuring a $C_p = 1.0$. The stagnation point for all shown C_p distributions was located at the LE on the BS and was not affected by a change in Re or α .

Another important effect of an increase in Re was a corresponding increase in the average ramp pressure (C_p). The increase in ramp C_p was likely caused by an increase in circulation due to a much larger suction peak for the Re = 235K and 352K cases compared to the almost fully separated airfoil case at Re = 117K.

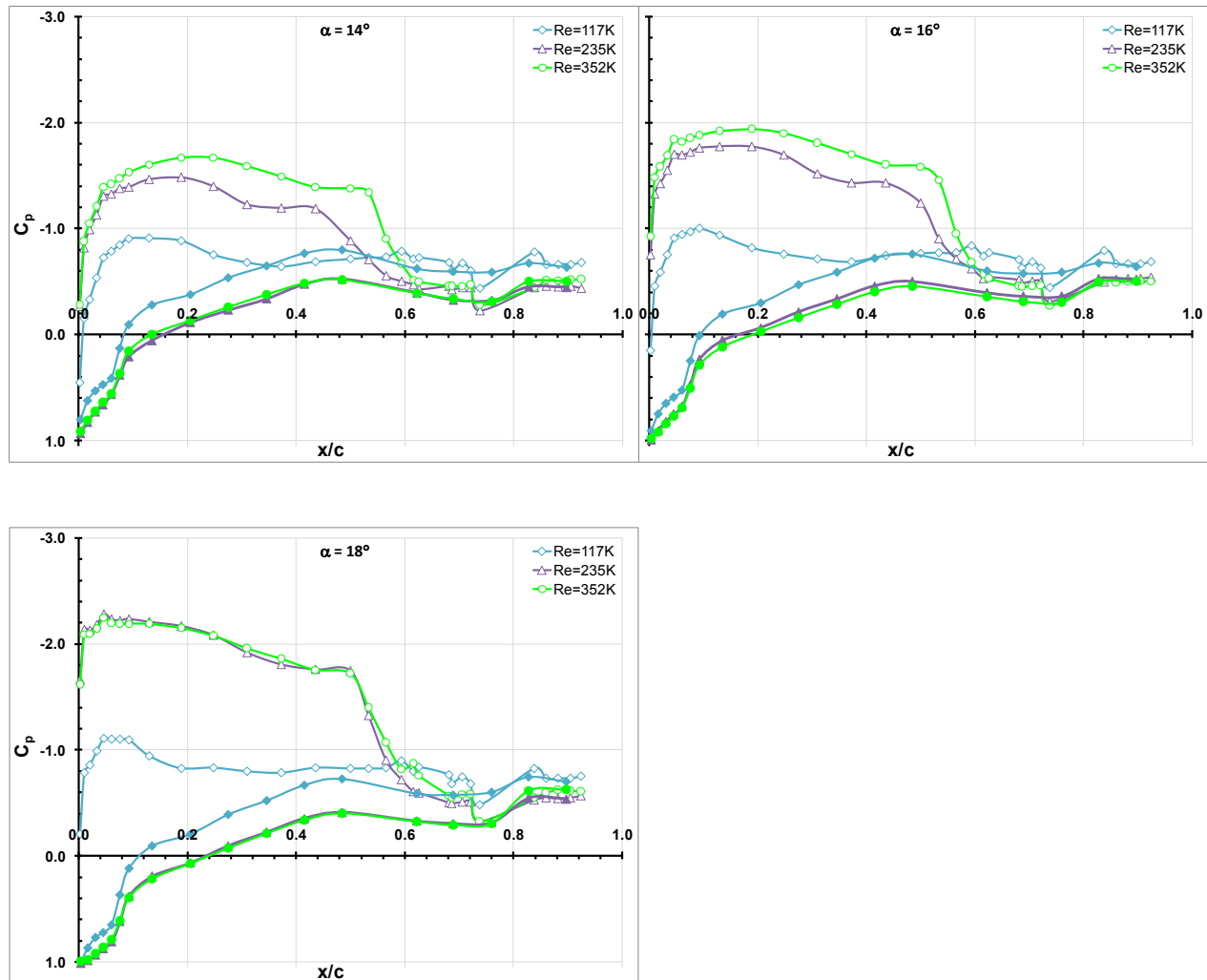


Chart 11. C_p vs. x/c distributions for $\alpha = 14^\circ$, 16° and 18° at $Re = 117K$, $235K$ and $352K$ in airfoil configuration B within the Davis wind tunnel.

C_L and C_D were strongly Re dependent at these low Re . Re independence was reached at large enough $Re > 400K$ for a clean and $> 250K$ for a tripped airfoil. The Re dependence and variations in Re dependence for different α 's was due to a TS bubble at $x/c \approx 0.4$, which moved with Re and α . Another tendency of a bubble at $x/c = 0.06$ was identified, which appeared Re and α independent.

6.1.3 Sensitivity of Airfoil Performance to Wind tunnel Turbulence

Apart from Re dependence, the airfoil was also sensitive to wind tunnel turbulence and possibly geometry variations. The airfoil was tested in the Scobee tunnel in 2004, in the Davis graduate wind tunnel in 2005 and again in the Scobee tunnel in 2005 using the original contraction and in 2007 using the added tunnel contraction. Some baseline variations in C_L and C_D were noticed, even at similar Re's and experimental conditions. In order to understand the significance of these variations the C_L vs. α curves are compared between the before mentioned measurement sets and historically available data in Chart 12.

There were two kinds of $\frac{dC_L}{d\alpha}$ changes that were noticed. First, a more gradual increase in $\frac{dC_L}{d\alpha}$ over a larger range of α , e.g. for the Re = 320K, Scobee tunnel in 2004 and 2007 and the Davis tunnel cases on average between $7^\circ < \alpha < 12^\circ$. Second, abrupt changes in $\frac{dC_L}{d\alpha}$ at a definite α , with large resulting ΔC_L . For the Scobee tunnel in 2005 at Re = 288K and 320K this occurred at respective $\alpha = 5^\circ$, and 7° . For Re = 112K in the Davis 2005 tunnel, Undergraduate 2005, 2007 tunnel case this occurred at $\alpha = 21^\circ$, 25° , and 25° respectively. With exception of the Undergraduate 2005 case changes in $\frac{dC_L}{d\alpha}$ were reduced with increasing Re. At Re $\geq 480K$ no change in $\frac{dC_L}{d\alpha}$ was apparent and

became largely independent on wind tunnel turbulence or Re effects, which supports previous discussions in Section 6.1.2.

The average wind tunnel turbulence level $\{(u')^2\}$ increased from the lowest, for the Scobee tunnel with original contraction setup (2004, 2005), to the Davis tunnel (2005), up to the Scobee tunnel, with added contraction (2007).

The gradual $\frac{dC_L}{d\alpha}$ for $Re \approx 320K$ approximately changed as followed from chart a) to e): a) $\frac{dC_L}{d\alpha}$ increased from 0.075 to 0.14, b) increased from 0.09 to 0.11, d) increased from 0.087 to 0.1 and e) increased from 0.089 to 0.092 with the highest $Re = 406K$ in the comparison.

The abrupt $\frac{dC_L}{d\alpha}$ for $Re = 320K$ in chart c) increased from 0.096 to 0.131. For chart b) at $Re = 117K$ the $\Delta C_L = 1$, for c) the $\Delta C_L = 1$, and for d) $\Delta C_L = 0.8$. For a detailed discussion of these cases and the consequences of abrupt $\frac{dC_L}{d\alpha}$ changes, see Section 6.1.6 on CL/CD hysteresis.

In cases of a) and c) the lowest $(u')^2$ existed and both had the largest gradual change in $\frac{dC_L}{d\alpha}$. With cases in b) and d), for increasing $(u')^2$, and e), for the highest Re in the comparison, the change in $\frac{dC_L}{d\alpha}$ was only $\sim 1/2$. The variations in $\frac{dC_L}{d\alpha}$ increase were

an indication of the airfoil's sensitivity to flow and/or surface properties themselves, other than Re. Gradual $\frac{dC_L}{d\alpha}$ changes were likely due to transition effects while abrupt changes were due to laminar separation and/or sudden turbulent reattachment.

In chart e) the tendency was noticed towards $C_{L_{\max}} = 1.0$ for $Re \geq 1210K$ combined with a C_L plateau and minimal stall from $20^\circ < \alpha < 30^\circ$. The high Re behavior corresponds to the Scobee tunnel 2004 behavior at $Re = 480K$ with large $(u')^2$.

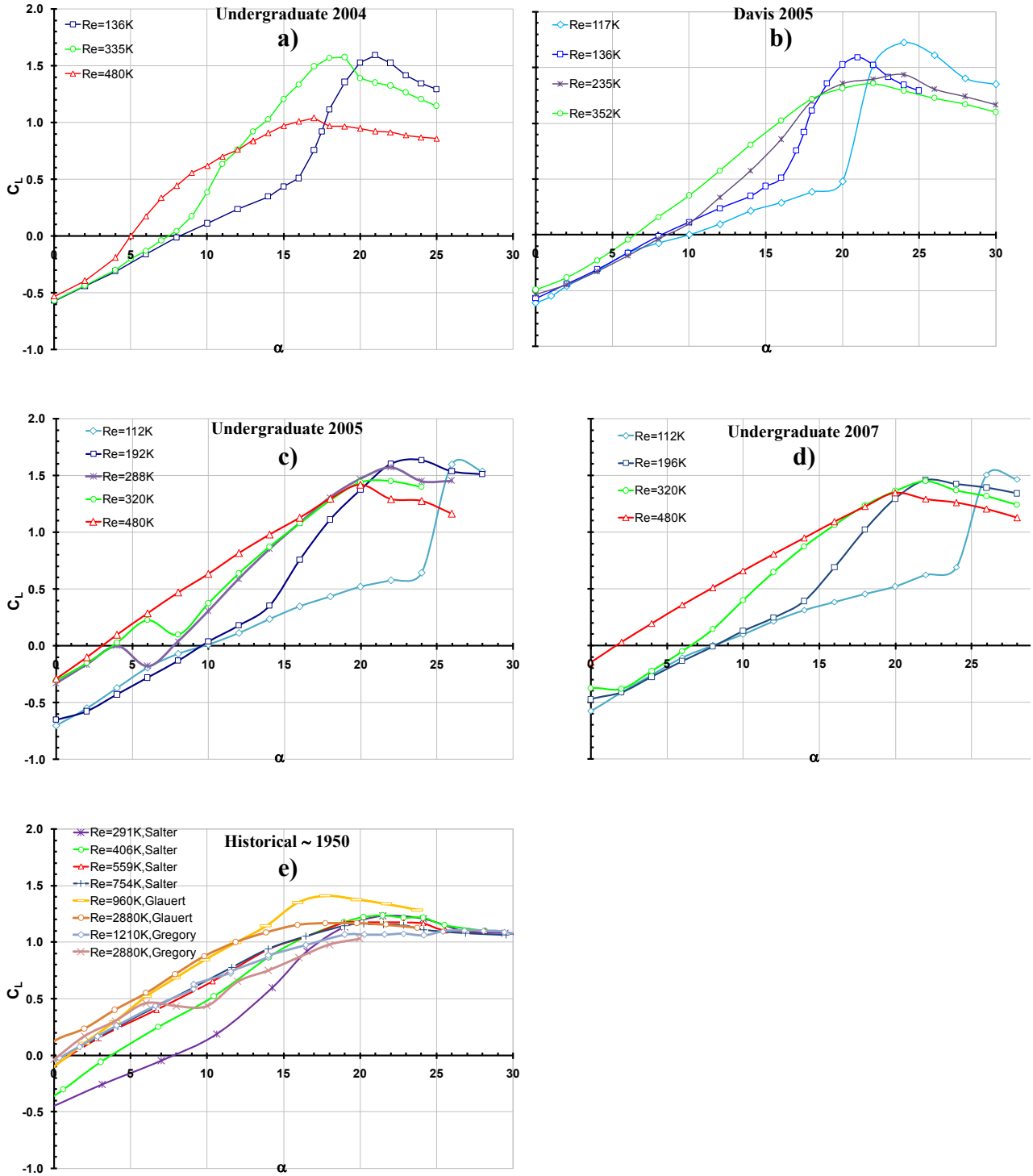


Chart 12. Baseline C_L variation study of multiple data sets with C_L vs. α at various Re 's.^{2, 23, 24}

The C_p distributions further illustrated the differences between experiments where sharp changes in $\frac{dC_L}{d\alpha}$ were experienced vs. ones where it was gradual. They are compared at $\alpha = 4^\circ$ and 8° , for the Scobee tunnel 2004, 2005, 2007 and Davis tunnel 2005 cases, in Chart 13 with $Re \approx 330K$. Unfortunately, Salter's and Glauert's C_p data was not available at this α and Re , neither was C_D data for the Undergraduate 2004 case.

The 2005 Scobee tunnel data, where an abrupt $\frac{dC_L}{d\alpha}$ change was present, showed that the flow over the TS stayed attached up to $x/c = 0.56$ at $\alpha = 4^\circ$. A small laminar separation bubble followed between $0.52 < x/c < 0.57$. The flow for the 2004, 2007 Undergraduate and 2005 Davis cases separated, before reaching $(t/c)_{max}$, at $x/c = 0.48$, 0.44 and 0.44 respectively, without noticeable reattachment. From C_p distributions, only a tendency of a bubble was apparent after initial separation. After the abrupt $\frac{dC_L}{d\alpha}$ change, for the Scobee tunnel 2005 case the $\frac{dC_L}{d\alpha}$ approximately matched the ones in which it was changing gradually. Hence, the C_p distributions at $\alpha = 8^\circ$ show that all experiments had very similar results.

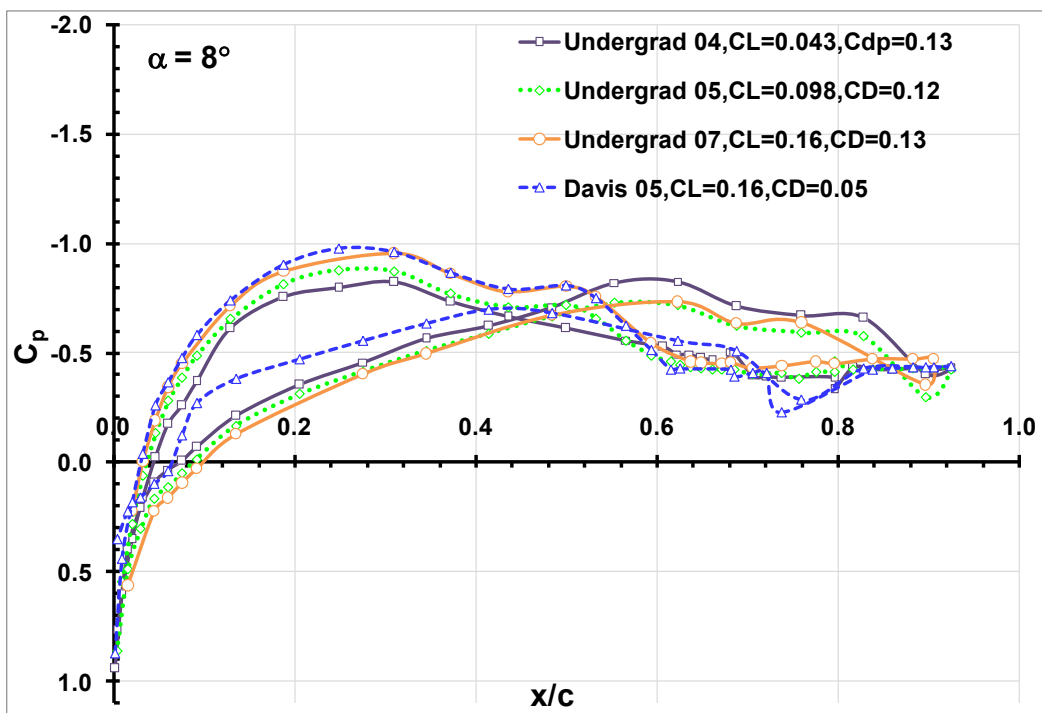
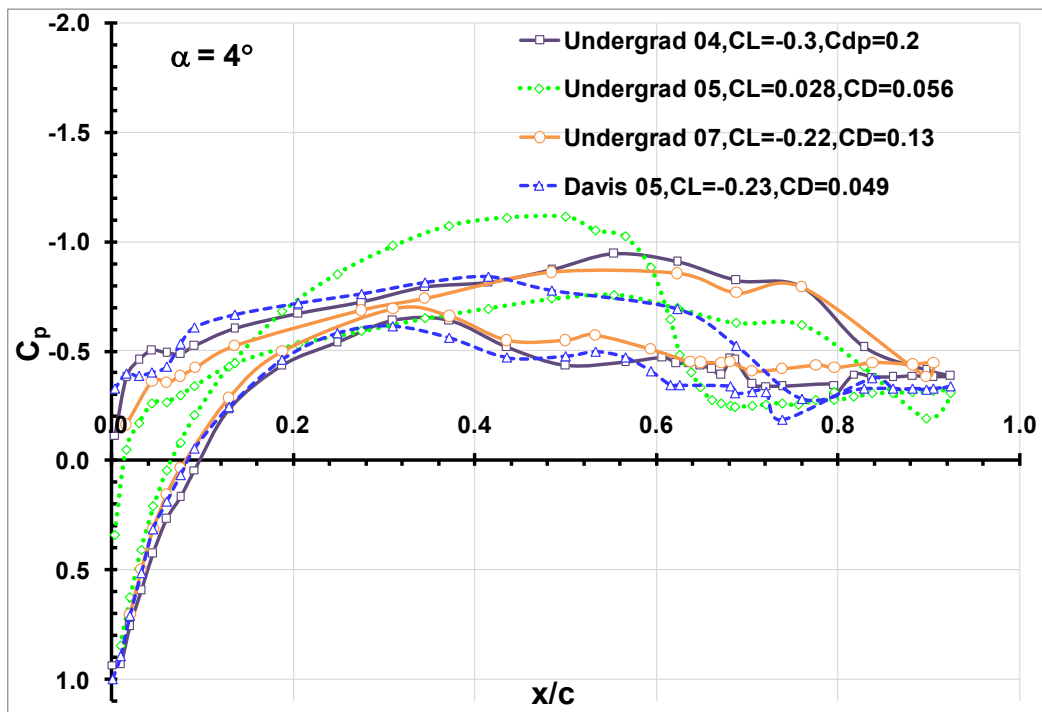


Chart 13. Baseline study of C_p vs. x/c at $Re \approx 330K$ corresponding to roughly ~ 20 m/s for a clean airfoil comparing Scobee tunnel 2004, 2005, 2007 and Davis tunnel 2005 data at $\alpha = 4^\circ$ and 8° .

The C_D for Undergraduate 2005, 2007, and Davis 2005 is compared to Salter's 1948 in Chart 14. In Undergrad and Davis wind tunnel experiments the C_D exhibited a very different behavior compared to Salter's. The same C_D behavior discussed in Section 6.1.1 was experienced during Undergrad tunnel 2005 and Davis tunnel 2005 experiments. For the Scobee tunnel 2007 and Davis tunnel 2005 the C_D increases substantially with increasing α to almost twice that of Salter's and more than three times that of the Scobee tunnel 2005 case at $C_L = 0$.

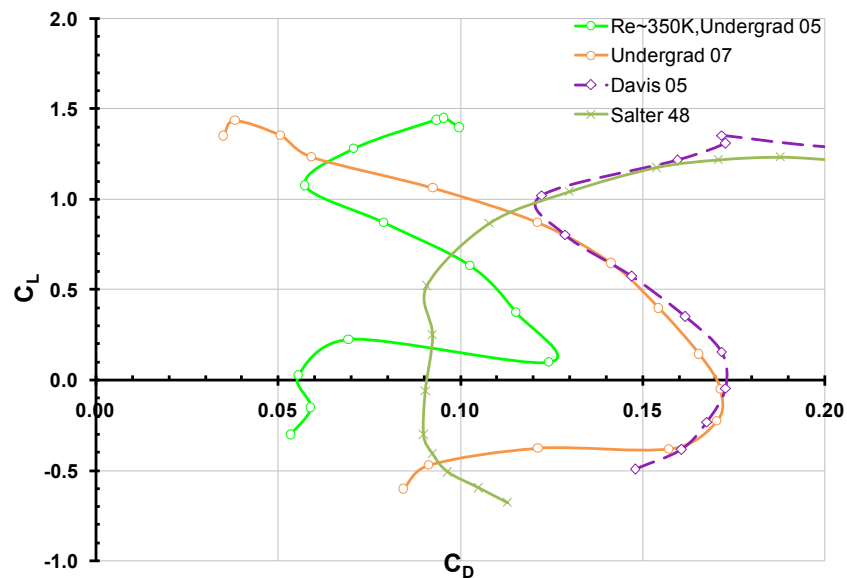


Chart 14. Baseline study of C_L vs. C_D at an average $Re \approx 350K$ corresponding to roughly ~ 20 m/s. The airfoil was clean and Scobee tunnel 2005, 2007 and Davis tunnel 2005 were compared with Salter's 1948 data.

The large increasing C_D at $C_L < 0.2$ was due to laminar separation experienced in the Scobee tunnel 2007 and Davis tunnel 2005 experiments. During these experiments

high $(u')^2$ between 0.3% - 0.8% was noticed. Chart 15 shows a typical $(u')^2$ velocity power spectra with sampling frequency of 4,096Hz and a sampling time of about 5 minutes. It compared high turbulence measures to low ones' after eliminating wind tunnel diffuser separation, cleaning dirty screens/ honeycombs, stiffening the nozzle structure, and restricting the fan inlet flow of the Davis tunnel.

Excluding the fan-inlet flow restriction (II), $(u')^2$ was reduced by 64.4%. Including the inlet flow restriction (III), $(u')^2$ was reduced an additional 55.1%. It also effectively dampened out large energy and low frequency oscillations of 5 Hz, 10 Hz, 20 Hz and 175 Hz. Flow oscillations were clearly visible with the wooden wind tunnel nozzle walls bellowing in and out.

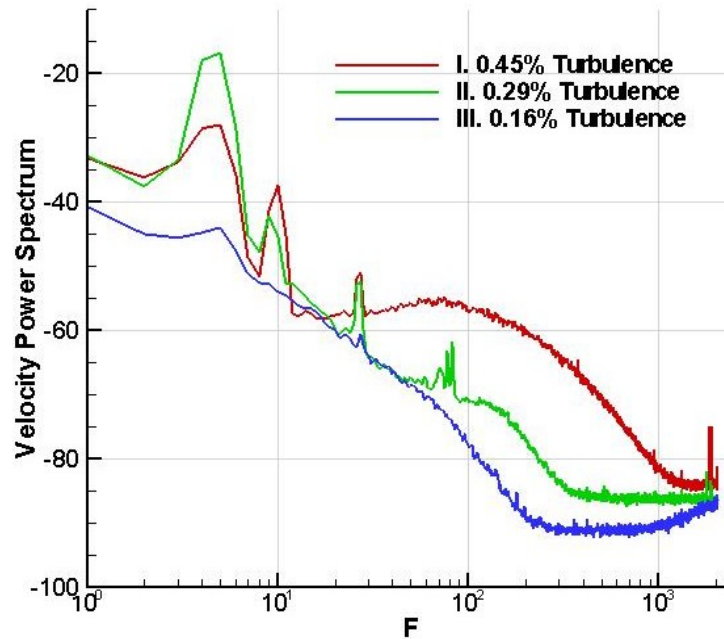


Chart 15. Davis wind tunnel turbulence study of single hotwire velocity power spectra taken in 2006. The sampling frequency was 4096Hz at ~ 5 minutes sampling time.

Wind tunnel turbulence had been identified as a possible driver for large increase in C_D due to laminar separation during Scobee tunnel 2007 and Davis tunnel 2005 experiments. The original contraction used in the Undergraduate 2004 and 2005 experiments effectively reduced $(u')^2$ to low levels of ~ 0.1% and the magnitude of C_D due to laminar separation.

6.1.4 Airfoil Geometry Variation Effects

Geometry variations between GLAS II specimens under investigation are illustrated in Figure 25. Red corresponded to the airfoil section used in the Scobee - 2005, 2007 and Davis – wind tunnel 2005 experiments at the AME. The slot was located at x/c

= 59%. For easier comparison the red geometry was slightly enlarged. Dark green corresponded to Salter's airfoil geometry with the slot located at. Light blue corresponded to Glauert's and the Undergraduate 2004 airfoil geometry with the slot located at the same $x/c = 0.69$.

The upper loft compared well between specimens. Hence, BL separation from the TS was most likely not effected by geometry variations. The airfoil tested at the AME had a smoothed nose in order to increase the radius and soften the sharp LE discontinuity. This could have had an effect on the stagnation location and α at which the stagnation point jumped from the TS to the BS. The discontinuity at $x/c = 0.69$ was removed as well for all experiments conducted at the AME. Since the ramp was separated during most experiments, little or no effect of smoothing was noticed. Salter's airfoil incorporated a ramp that was utilized as a flap with the hinge-point located at $x/c = 0.60$. A slight positive zero flap-angle offset was visible. This could have enlarged the separation region on the BS increasing C_D .

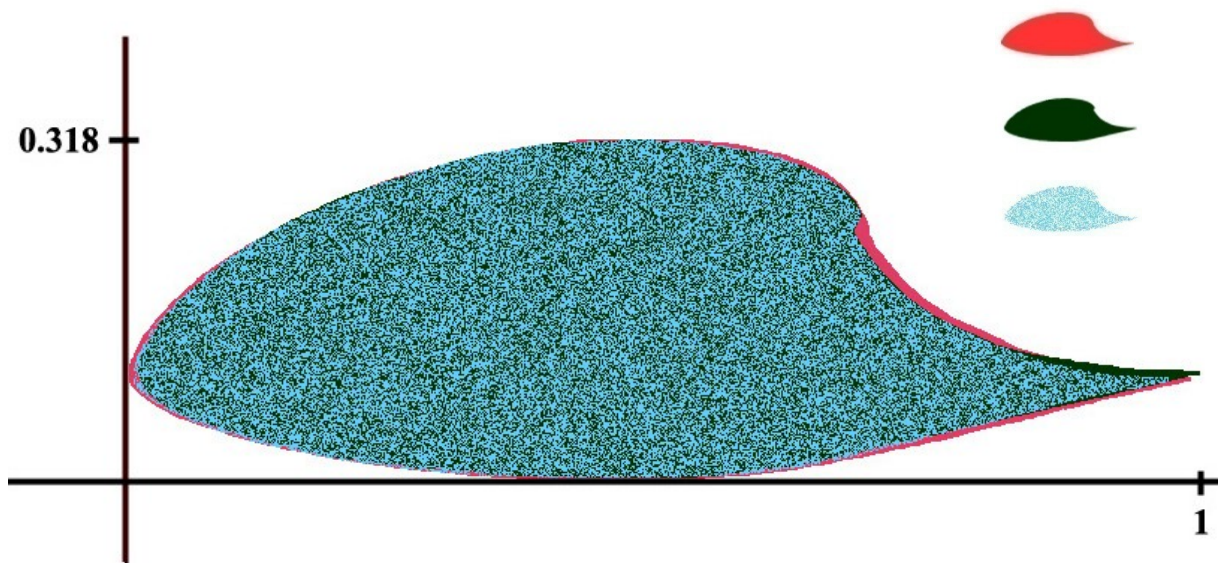


Figure 25. Changes in airfoil geometry for various experiments.

A laminar separation bubble was identified as one reason for variations in C_L and C_D between various data sets. The bubble was sensitive to $(u')^2$, α , Re's, and roughness.

High $(u')^2$ within the Davis tunnel 2005 and the Scobee tunnel 2007 experiments with the added contraction induced early BL separation. This resulted in a drop of C_L and an increase in C_D .

The smoothing of the LE for all AME experiments might have effected the stagnation point location. Salter's positive zero flap-angle offset could have been responsible for higher C_L at low α 's and/or larger separation from the BS of the ramp.

6.1.5 Historical Baseline Comparison

To validate baseline calculation and measurement technique data from the Scobee tunnel is compared to historically made measurements in Chart 16. The airfoil in configuration C with the added contraction was used and the closest matching Re values available were compared. Salter conducted his experiments in the compressed 1.83 m x 1.22 m air wind tunnel (CAT) at the National Physical Laboratory (NPL) using a force sting balance. His model was made out of two pieces of Mahogany with a metal flap and measured $c = 20.3$ cm, and $b = 1.22$ m.^[24] Glauert conducted his experiments in the 3.96 m x 2.74 m NPL air wind tunnel using surface pressure measurements. His model was made out of two pieces of Mahogany, but did not have a metal flap, and measured $c = 76.2$ cm, and $b = 2.74$ m.^[2]

The Scobee tunnel C_L vs. α curve fell in between Salter's and Glauert's. Glauert's $\frac{dC_L}{d\alpha}$, at $Re = 960K$, was shifted $\Delta C_L \approx +0.2$, while Salter's, at $Re = 406K$, was shifted $\Delta C_L \approx -0.15$. The Scobee tunnel $\frac{dC_L}{d\alpha} = 0.085$ matched Glauert's and Salter's at $Re = 406K$. Interestingly Salter's $\frac{dC_L}{d\alpha}$ decreased to 0.0635 at $Re = 559K$ with a large C_L jump at low incidence that compared to Glauert's curve, but at $\alpha > 15^\circ$ it more closely matched the $Re 406K$ case.

C_D behaved very differently compared to Glauert's or Salter's. One contribution to the differences was discussed in Section 6.1.2 and could have come from the C_D 's

dependence on Re . However, at $Re \geq 406K$ a plateau was reached after which the airfoil's C_D became independent of Re , even for a clean airfoil.

Another possible source discussed in Section 6.1.3 for variations in C_D was due to $(u')^2$ and induced separation resulting in an initial increase in C_D for increasing α . However, no such trends were visible in Chart 16.

It was believed that a major contributor to variations in C_D was related to the applied measurement technique. Glauert did rake pressure measurements with a pitot rake located 0.1 chord lengths behind the airfoil. Since he measured the wake so close behind the airfoil, he had to correct for the drop in P_s . This would explain the limited α range for which Glauert was able to measure C_D , only from $-2^\circ < \alpha < 8^\circ$. Salter used a force balance to measure C_D . Glauert's C_D , at $C_L = 0$, was 10% larger than Salter's and twice as large than the C_D measured in the Scobee tunnel. There the Pitot-rake was placed more than three chord lengths downstream of the airfoil with no correction for losses due to ΔP_s with resulting errors discussed in Section 5.3.4. The corrected C_D should have been slightly higher than presented. However, this would not have explained the twofold differences.

Another difficulty arose measuring the correct P_s three chord lengths downstream of the airfoil. The wake often spread and changed its location, at times impinging on the local P_s measurement tube. This caused an erroneous P_s reading that was higher with

resulting larger C_D , due to the normalization error. However, this would not explain the twofold differences between historical and AME results.

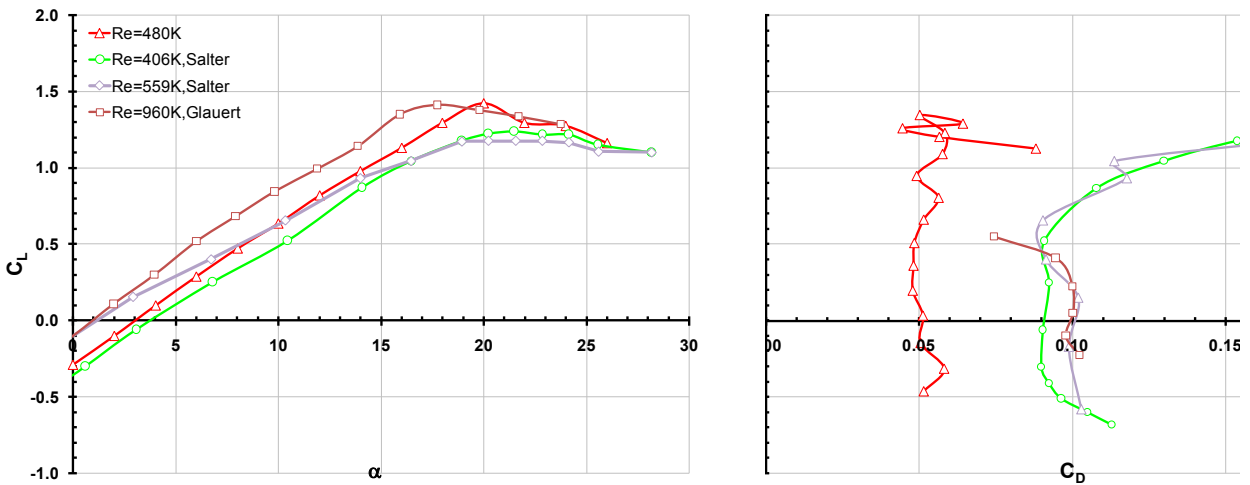


Chart 16. Historical baseline comparison of C_L vs. α and C_D and best matching Re's for a clean airfoil with open slot in configuration C and added contraction.^{2,24}

The historical baseline L/D 's vs. C_L and α are compared to new data in Chart 17. A $(L/D)_{\max} = 28$ was reached for $Re = 480K$ at $\alpha = 24^\circ$. For $Re = 406K$ the maximum $(L/D)_{\max} = 8$ at $\alpha = 15^\circ$, and for $Re = 960K$ the $(L/D)_{\max} = 8$ at $\alpha = 6^\circ$ after which no additional data was published.

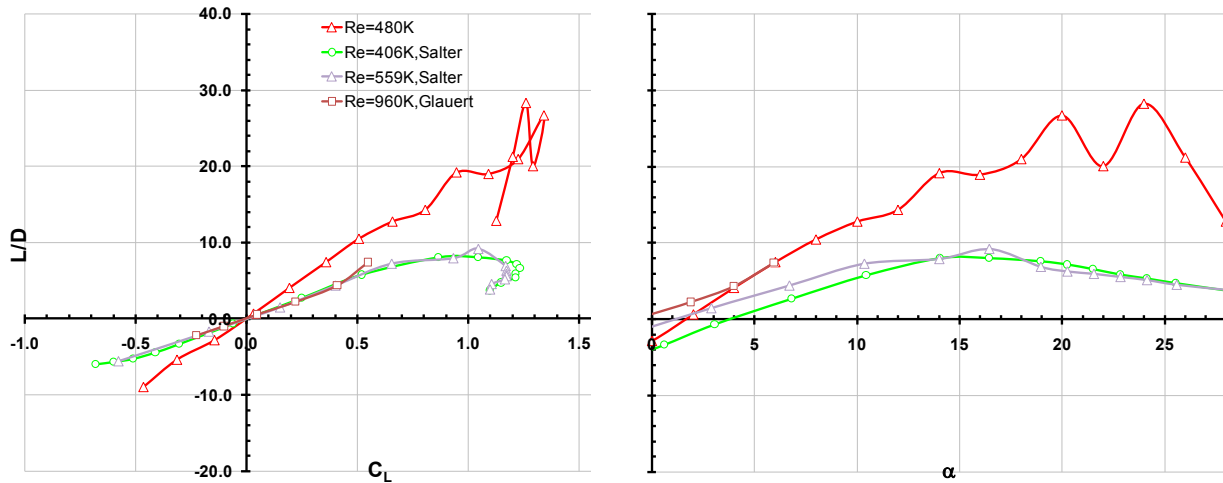


Chart 17. Historical baseline comparison of L/D vs. C_L and α for best matching Re 's. A clean airfoil with open slot in configuration C with added contraction was used.^{2,24}

While the C_L compared well for similar Re 's, the C_D exhibited a very different behavior. Wake measurement error and technique were believed to be the sources for C_D variations between Salter's, Glauert's and Scobee tunnel 2007 wake measurements.

6.1.6 Hysteresis Analysis

Hysteresis was discovered on the modified GLAS II dependent on roughness, Re , and $(u')^2$. Abrupt lift/drag-curve slope changes $\left\{ \Delta \frac{d(C_L \cup C_D)}{d\alpha} \right\}$ were associated with hysteresis effects. Hysteresis occurred when the C_L/C_D -curve followed two different paths, whether the incidence was increased ($\alpha+$) or decreased ($\alpha-$), hence would be a function of direction of $\Delta\alpha$, not only $\Delta\alpha$.

In order to investigate the C_L/C_D hysteresis phenomenon α was increased past the airfoils' α_s , and then decreased again to the starting α . After each $\Delta\alpha$ a one minute

settling time followed to allow the flow to reach steady state before acquiring data. In the following charts, lines of α^+ were solid, while lines of α^- were dotted.

Hysteresis at $Re = 112K$ is shown with airfoil in configuration C using the added contraction in Chart 18. At $Re = 112K$ hysteresis occurred around α_s between $22^\circ < \alpha < 28^\circ$, with C_L/C_D -curves not following the same paths for α^+ vs. α^- . C_L and C_D hysteresis were coupled and experienced at the same α . Large variations, by a factor of up to 2.59, in L/D resulted.

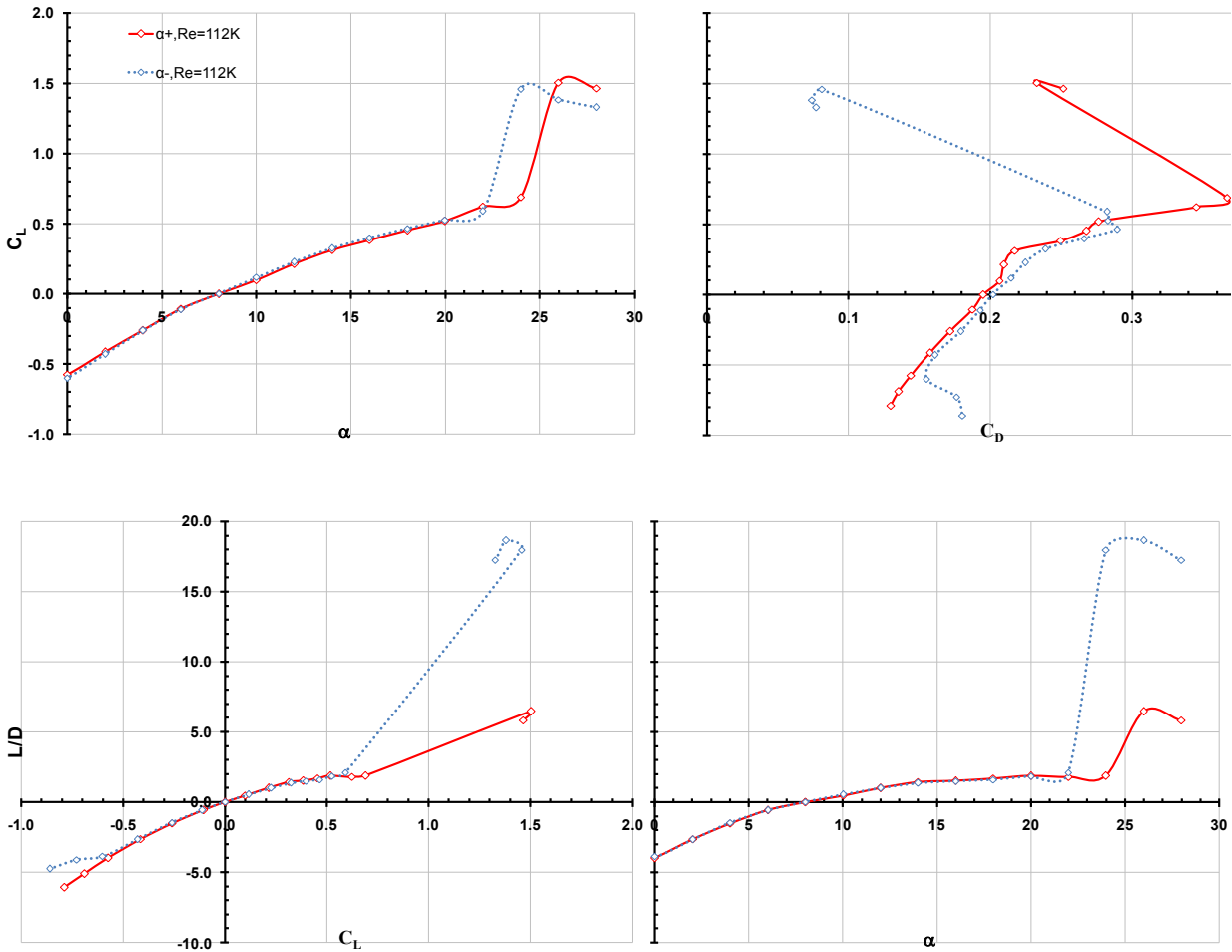


Chart 18. Stall hysteresis study at $Re = 112K$ for a clean airfoil in configuration C using the added contraction. Solid red lines marked $\alpha+$ while dotted blue lines indicated $\alpha-$.

C_p distributions were analyzed at $\alpha = 22^\circ, 24^\circ$ and 26° in Chart 19. For each α two C_p distributions were compared one for $\alpha+$ and one for $\alpha-$. At $\alpha = 24^\circ$ the $\alpha+$ vs. $\alpha-$ C_p distributions differed. For $\alpha+$ the airfoil TS had completely stalled while for $\alpha-$ the flow had stayed attached with a tendency of a bubble between $0.30 < x/c < 0.35$ on the TS. One could explain that the higher turbulence level past stall for $\alpha-$ tripped the flow to it's turbulent state further upstream on the TS, thereby preventing separation. The C_L varied

by a factor of 2.12 and the C_D varied by a factor of 4.63. The slight shift shown in the $\alpha = 22^\circ, 26^\circ$ C_p distributions, between α^- and α^+ , was due to measurements being conducted at different times with possible slight variations in Re and $(u')^2$.

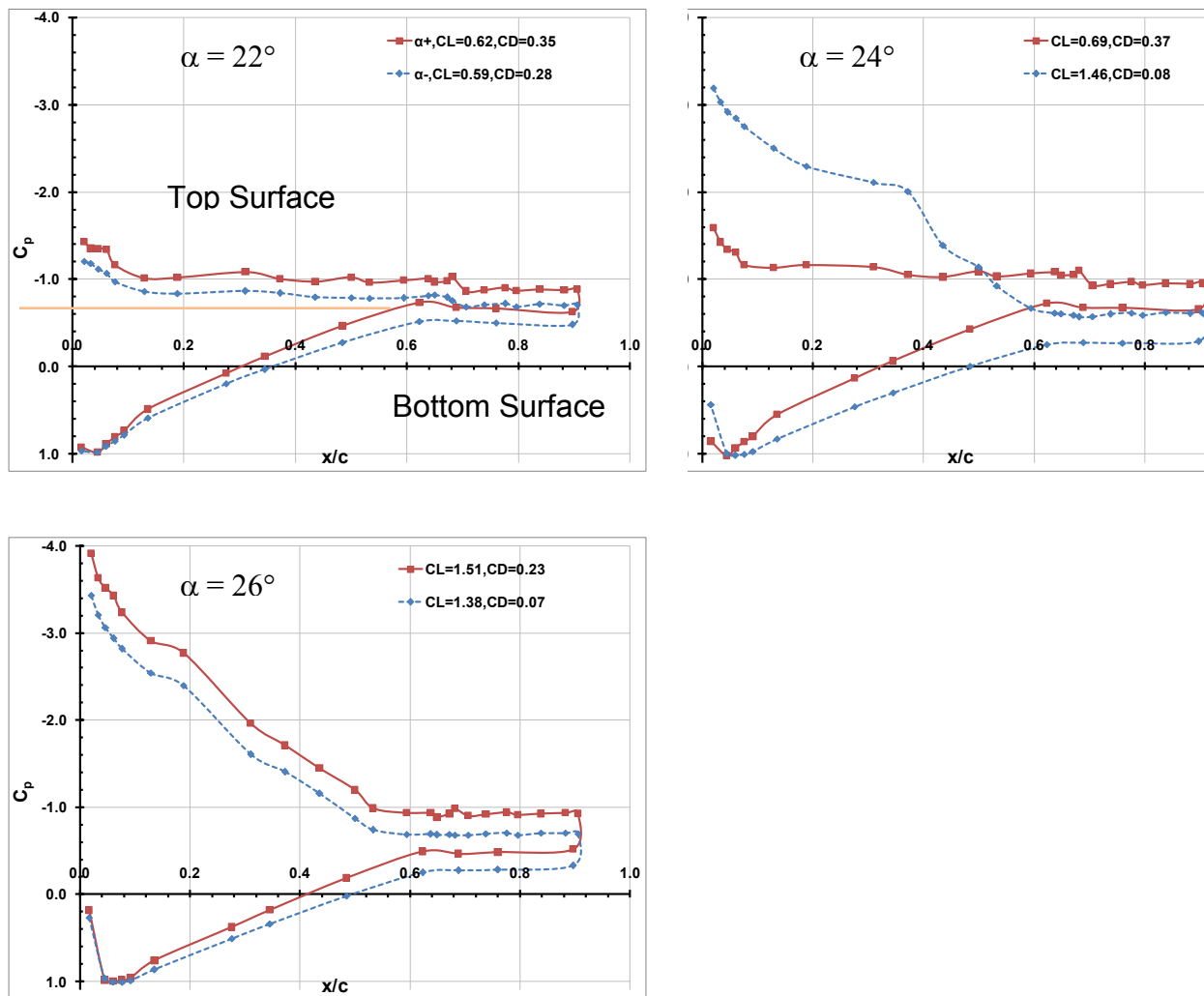


Chart 19. C_p distributions at $\alpha = 22^\circ, 24^\circ$, and 26° around hysteresis. $Re = 112K$ for a clean airfoil in configuration C and added contraction. Solid red lines marked α^+ while dotted blue lines indicated α^- .

Hysteresis was also discovered at lower α 's and higher Re's in Chart 20. The original 2004/2005 Scobee tunnel contraction, for airfoil configuration C and $Re = 320K$, was used. The solid red lines corresponded to $\alpha+$ while the dotted blue lines corresponded to $\alpha-$. An increase in $\Delta C_L = 0.15$ occurred at $\alpha = 7.25^\circ$ for $\alpha+$ and a decrease in $\Delta C_L \sim 0.15$ occurred at $\alpha = 0^\circ$ for $\alpha-$. The $\alpha+$, $\alpha-$ measurements were repeated several times with the same results. While there was a rapid drop in C_L at $\alpha = 7.25^\circ$, there also was a sudden increase in C_D of 44%. $\Delta L/D_{\max} = 4$ occurred at $\alpha = 6^\circ$. The combined hysteresis effect on L/D was not as large as one would expect from its' individual effects on C_L and C_D .

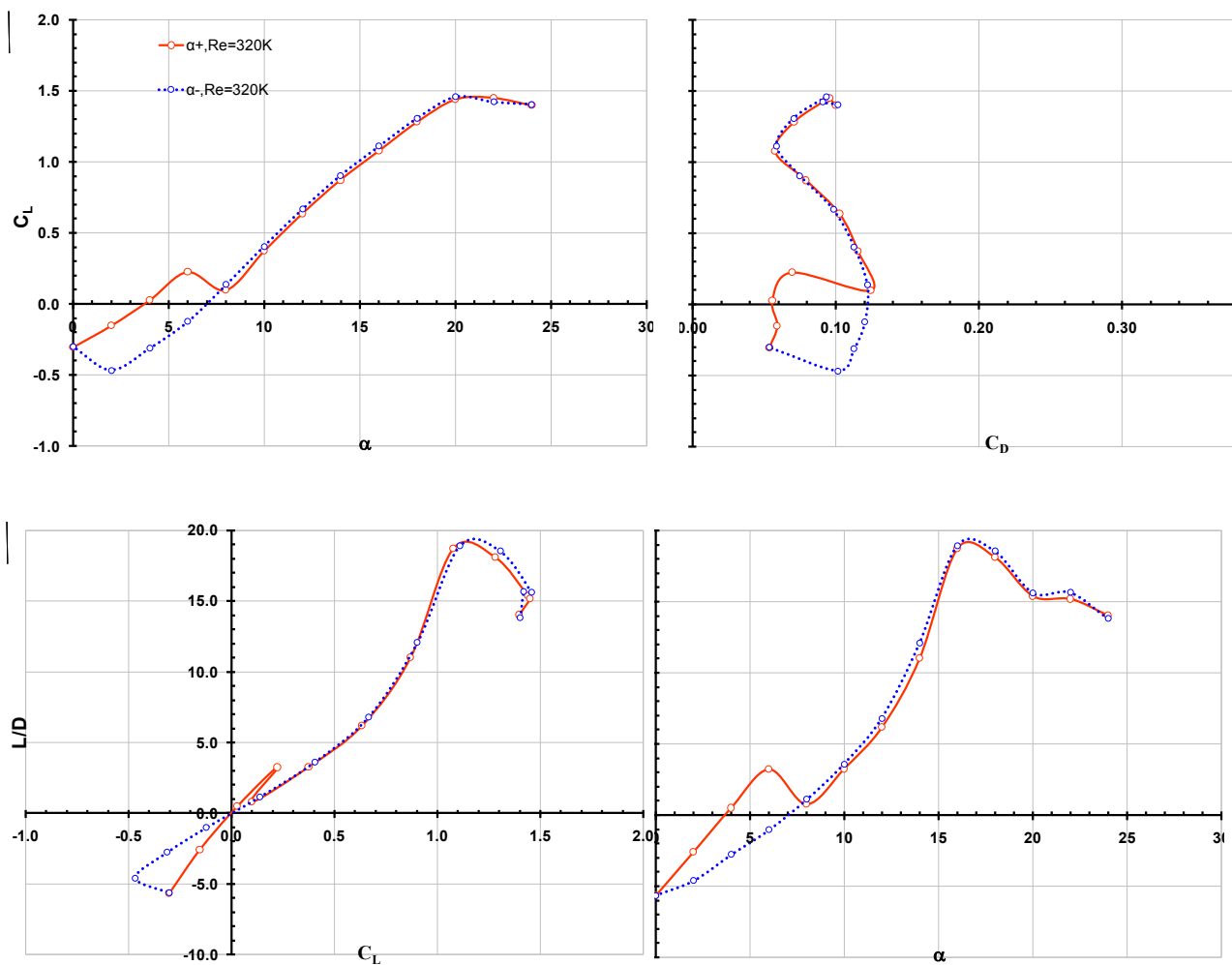


Chart 20. Hysteresis at $Re = 320K$ for a clean airfoil in configuration C using the original 2004/2005 Scobee tunnel contraction. Solid red lines marked $\alpha+$ while dotted blue lines indicated $\alpha-$.

C_p distributions were analyzed at $\alpha = 0^\circ, 4^\circ, 6^\circ,$ and 8° shown in Chart 21. The TS pressure taps had square symbols while the BS ones' had round symbols. The same $Re = 112K$ methodology for C_p comparison applied for $Re = 320K$. A laminar separation bubble appeared to reside around $x/c = 0.56$, which kept growing and moving upstream. At $\alpha \approx 6^\circ$ it extended from $x/c = 0.40$ all the way to $x/c = 0.52$. Increasing α further caused the bubble to burst, which was associated with abrupt drop in C_L and increase in

C_D . The flow separated upstream of the ramp at $x/c = 0.45$ without significant turbulent reattachment shown by the decrease in ramp $C_p = 0.13$.

This illustrated a problem of laminar high lifting airfoils. On the one hand the thick airfoil guarantees a favorable pressure gradient over its' 50% chord making the laminar BL immune to Tollmien-Schlichting type disturbances, on the other hand transition to turbulence needs to occur soon enough to stabilize the BL before entering regions of adverse pressure. One such region existed right after maximum airfoil thickness, the other one within the ramp. To avoid laminar separation and separation bubbles it was necessary to trip the BL. This artificially induced BL transition to turbulence upstream of the bubble shown in the first and second C_p distribution for $\alpha+$.

At $\alpha = 0^\circ$ the airfoil's BS stalled entirely, at all other α 's the BS stalled at $x/c \approx 0.65$. An important observation was made at this α . The $C_p = 1$, which corresponded to the stagnation point, was located on the TS not the BS.

Apart from the TS bubble, there were two additional bubbles on the BS. One bubble was located between $0.64 < x/c < 0.80$, while the other at $x/c = 0.04$. The BS TE bubble did not move much or grow within the inspected α range, and hence did not contribute to the hysteresis effect. The $x/c = 0.04$ BS bubble disappeared at $\alpha = 8^\circ$ indicating a possible burst. The burst could have caused turbulent transition to occur earlier through introduction of a disturbance. The pressure gradient on the BS was not as

favorable as had been the case on the TS and the laminar BL became much more sensitive to disturbances undergoing transition more easily.

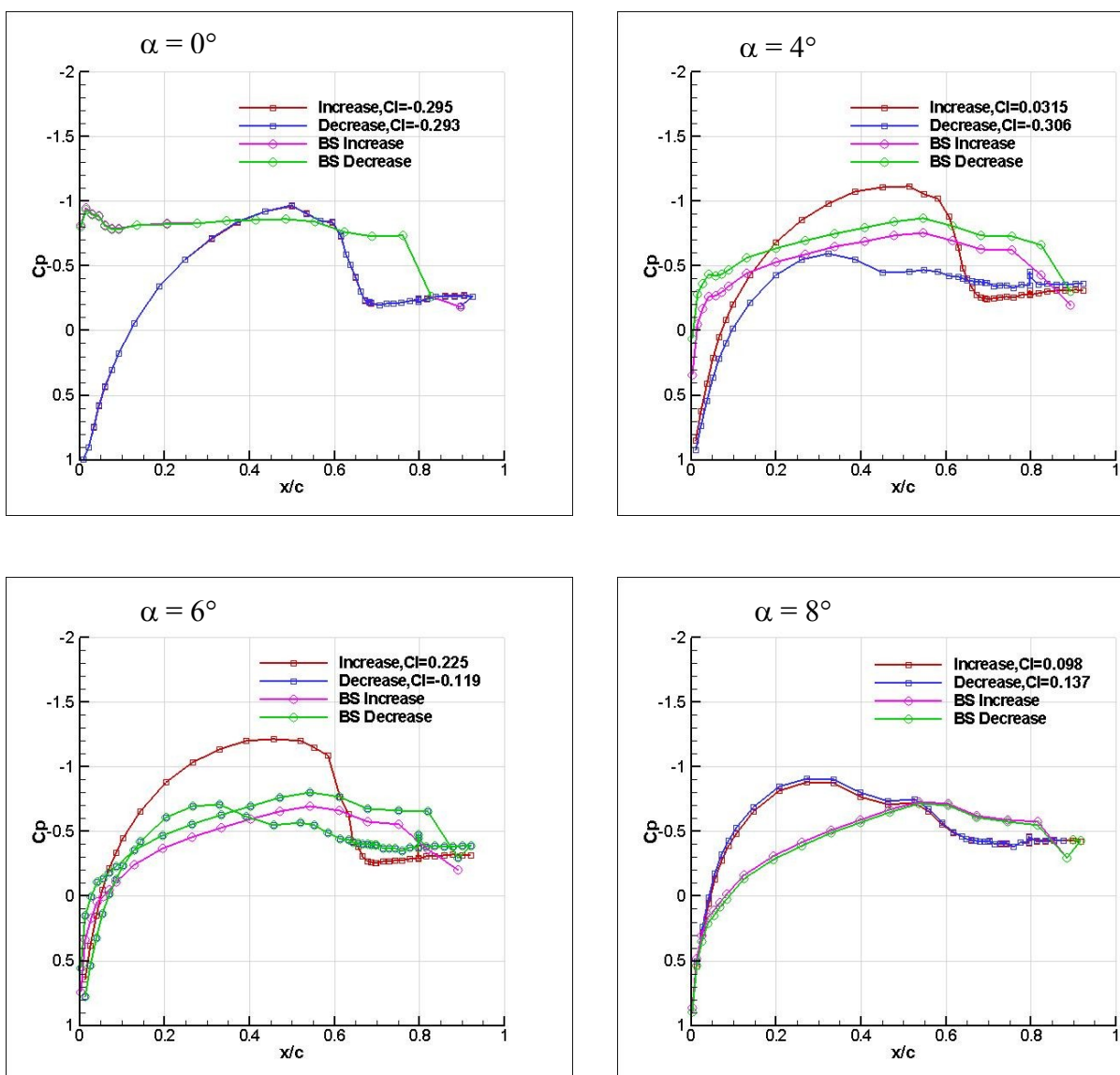


Chart 21. Hysteresis study of C_p vs. x/c at $Re = 320K$ at $\alpha = 0^\circ, 4^\circ, 6^\circ$ and 8° for $\alpha+$ (red TS and pink BS) and $\alpha-$ (blue TS and green BS).

C_L/C_D - hysteresis was discovered at $Re = 112K$ and $320K$. Hysteresis was caused by a laminar separation bubble on the airfoil's TS between $0.35 < x/c < 0.60$. The bubble was not stationary nor did it have a fixed size. It changed size and location with increasing or decreasing α , variation in Re , or change in flow turbulence level. A bubble burst at a fixed α resulted in abrupt drop in C_L and rise in C_D . Another bubble on the BS between $0.65 < x/c < 0.80$ was discovered. This bubble did not affect C_L/C_D - hysteresis.

The small BS LE bubble decreased C_L slightly upon burst, tripping the BL turbulent, but it had no noticeable effect on C_L/C_D - hysteresis.

At $\alpha = 0$ the stagnation point was located on the TS of the airfoil.

6.1.7 Baseline CFD Study

Flow structures around the GLAS II, at $\alpha = 0^\circ, 4^\circ, 6^\circ$ and 8° were visualized using CFD by Ahmed Hassan, Boeing Mesa.¹³ Baseline u velocity contours were calculated at $Re = 2,880K$, $M = 0.1$, shown in Figure 26. CFD results were investigated to support the discussion in Section 6.1.6 and Chart 21. CFD was compared to experimental data to test for existence of a bubble on the TS and BS, BL separation location, as well stagnation point location, and thereby verify CFD computations.

At $\alpha = 0^\circ$ on the TS there was hardly any thickening of the BL between $0.56 < x/c < 0.60$ where a bubble was detected from C_p distributions in Chart 21 at $Re = 320K$. At nine times the Re , the flow likely stayed attached up to $x/c \approx 0.65$ undergoing transition

to turbulence at $x/c \approx 0.5$. However, a thickening of the BS BL between $0.65 < x/c < 0.85$ was shown at $\alpha = 0^\circ$. This roughly corresponded to a laminar bubble suspected from the C_p distributions in Chart 21 between $0.64 < x/c < 0.76$ at the same α . CFD results showed a bubble that was likely to be much smaller than at $Re = 320K$ due to the large differences in Re 's.

The LE stagnation point at $\alpha = 0^\circ$ was located on the TS. This created a low pressure region on the LE BS shown as red high density velocity contours. With increasing α the stagnation point moved upstream towards the LE. At $\alpha = 8^\circ$ the stagnation point was almost at the LE. The LE BS low-pressure region vanished. Both observations agreed well with those made from the C_p distributions in Chart 21.

At $\alpha = 10^\circ$ the TS BL fully separated at $x/c \approx 0.4$, which agreed with the BL separation shown in Chart 21 at $x/c = 0.45$ and $\alpha = 8^\circ$. The BS BL did not separate in the computations, but it did separate based on the C_p distributions at $x/c = 0.73$ for $\alpha = 8^\circ$.

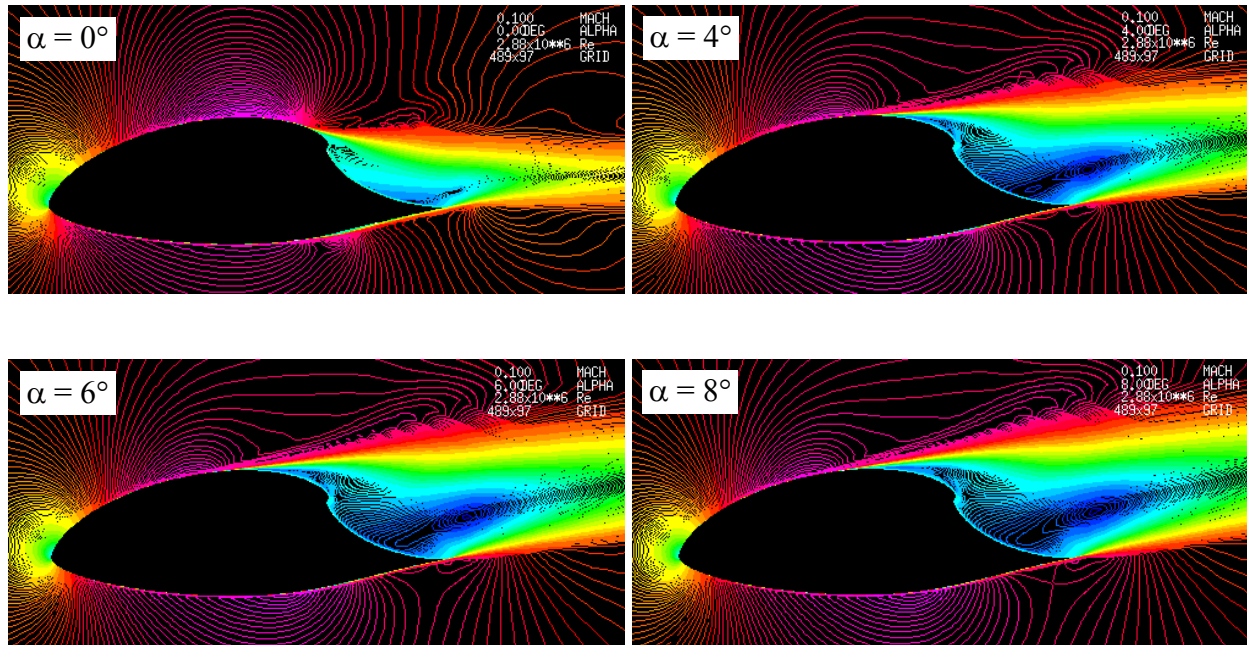


Figure 26. Baseline CFD study with u velocity contours. Computations were performed at 54.9 m/s at $\alpha = 0^\circ$ and 10° on a clean airfoil.¹³

CFD data did support assumptions made about the existence of a separation bubble on the BS ramp at $x/c \approx 0.72$ and $\alpha = 0^\circ$. It also accurately predicted the BL separation location on the TS. However, at that Re , no bubble was seen on the TS and the BL on the BS ramp did not separate.

The stagnation point jumped from the LE TS to the LE with increasing α . The LE TS stagnation point created a low-pressure region on the LE BS, which was also seen in the C_p distributions.

6.1.8 Effects of Roughness

Sand roughness was used to eliminate the effect of transition by fixing the transition location. It thereby prevented or delayed laminar separation, hence abrupt airfoil stall.

Several important length scales included average grain height, grain density, tape width, thickness, and height. Roughness in general increased C_D because it locally decreased Re and enhanced viscous effects such as BL mixing, thereby increasing C_f . As a comparison to the simplified flat plate BL model the C_f would change due to tripping from $C_f \propto 1/Re^{1/2}$ to $\propto 1/Re^{1/5}$.

Sand roughness illustrated in Figure 27 was used for tripping at TS locations of $x/c = 0.30, 0.36, 0.38$ and 0.58 and BS locations of $x/c = 0.56$ and 0.60 . Double-sided scotch tape was used that was 12.4 mm wide and 0.14 mm thick. It's center was the reference. The 60-grit sand with an average height of 0.36 mm was evenly applied over one side of the double-sided tape. V-shape cutouts were made when close to airfoil taps in order avoid measurement error described in Section 5.3.3.



Figure 27. Sand roughness strip were applied along b on the TS at 30%, 36%, 38% and 58 % chord and on the BS at 56% and 60% chord.

C_L vs. α and C_D are shown in Chart 22 for roughness placed at $x/c = 0.36$ TS and 0.56 BS, or a combination thereof. The airfoil tested was in configuration C within the Scobee tunnel using the original contraction at $Re = 320K$. First, the bubble on the BS TE was addressed by tripping at $x/c = 0.56$ on the BS. The BS bubble was eliminated but C_D increased slightly, hence no positive effect on C_D was realized by tripping at this location during baseline. C_L did not change with the BS trip. Second, the bubble $x/c \approx 0.56$ TS was addressed by tripping at $x/c = 0.58$ TS and 0.56 BS simultaneously, again with no effect on hysteresis. Third, roughness was placed at $x/c = 0.36$ TS. This location was chosen because at all α 's the BL would be tripped upstream of the fully separated zone between $0.40 < x/c < 0.52$ shown in the C_p distributions during α^- . This successfully eliminated the laminar separation bubble. Unfortunately, it also increased base drag, which was expected when roughening the surface. Finally, roughness was applied to $x/c = 0.36$ and 0.56 BS.

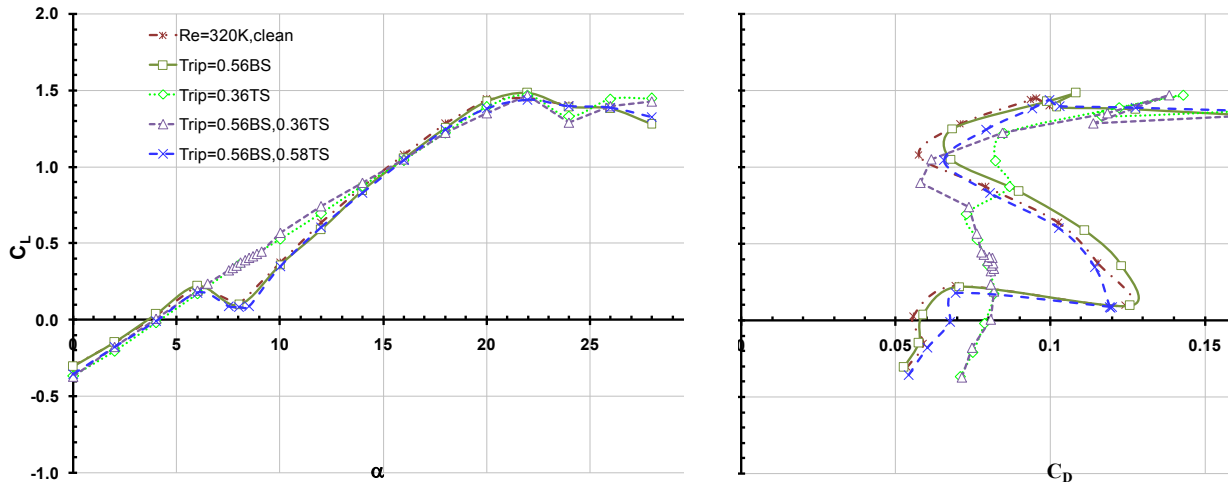


Chart 22. C_L vs. α , and C_D and $Re = 320K$. Roughness at $x/c = 0.56$ BS, 0.58 TS, and 0.36 TS was applied. The airfoil configuration C with original contraction was used.

The performance penalty of tripping is investigated by looking at L/D in Chart 23.

The L/D was improved by the $x/c = 0.36$ TS roughness between $6^\circ < \alpha < 14^\circ$. Additional L/D improvement was realized for $12^\circ < \alpha < 15^\circ$ by tripping at $x/c = 0.56$ on the BS. However, the penalty due to tripping compared with clean baseline at $\alpha > 14^\circ$ was substantial with reductions in $(L/D)_{\max}$ of up to 10%. It would be desirable to prevent separation more efficiently with less performance penalty and keep the BL laminar over more than just 36% chord.

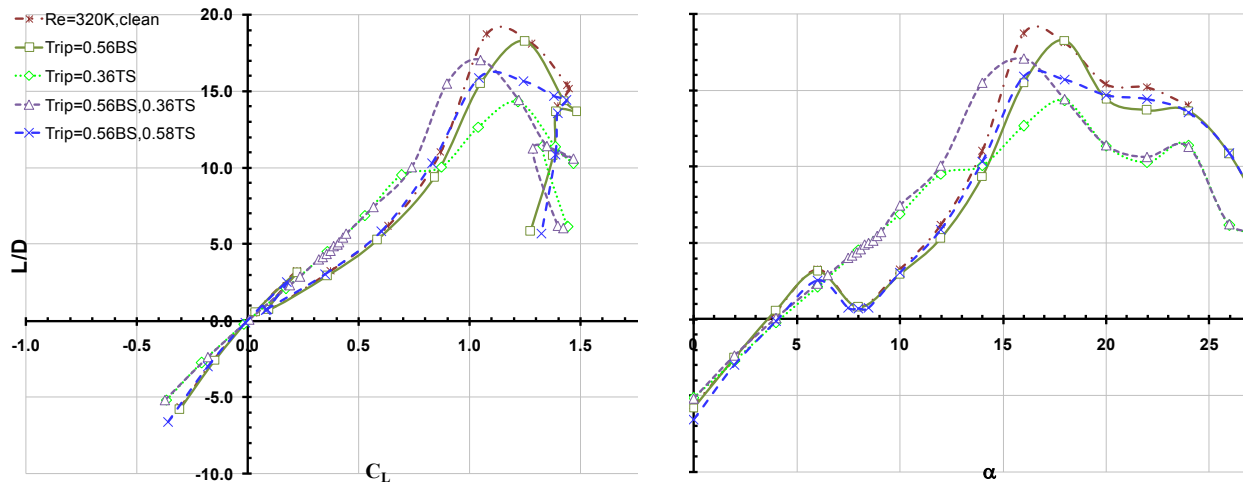


Chart 23. L/D vs. C_D at $Re = 320K$. Roughness at $x/c = 0.56$ BS, 0.58 TS, and 0.36 TS was applied. The airfoil configuration C with original contraction was used.

The effect of roughness was analyzed at $Re = 480K$ where no hysteresis was apparent in the clean baseline results. Roughness was placed at $x/c = 0.36$ and $x/c = 0.38$ on the TS shown in Chart 24. Roughness increased C_D at $\alpha = 0^\circ$ by 32.5% and reduced average C_L by about 15%.

At $\alpha_s \approx 20^\circ$, a 2% change in the chordwise roughness location had a large effect on C_L and C_D . With roughness at $x/c = 0.38$ two stalls seemed to occur, one at $\alpha = 18^\circ$ and the other at $\alpha = 25^\circ$. This might be attributed to a turbulent reattachment at post stall conditions on the TS.

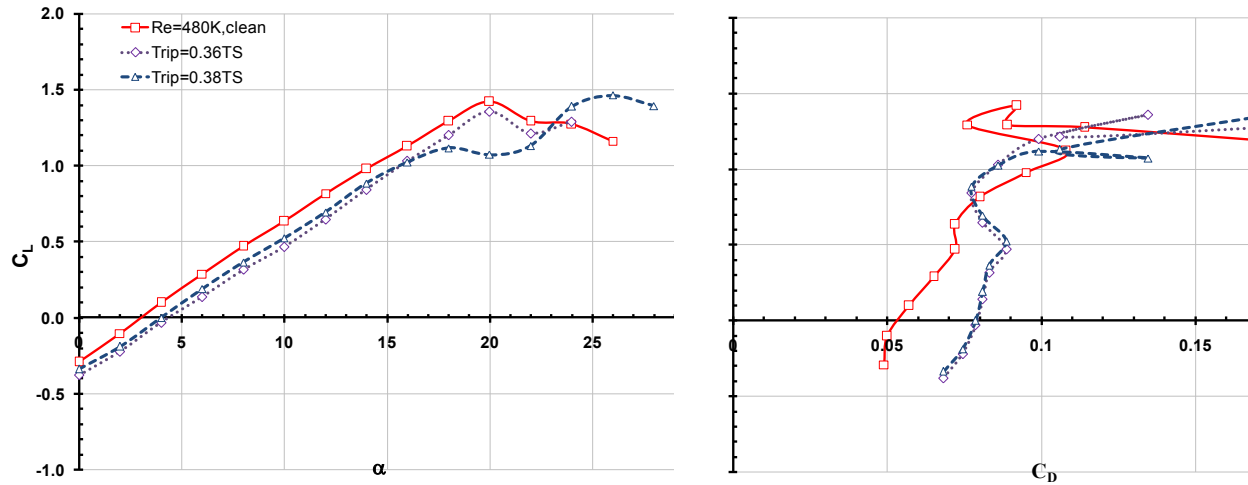


Chart 24. C_L vs. α , and C_D and $Re = 480K$. Roughness at $x/c = 0.36$ TS and 0.38 TS was applied. The airfoil configuration C with original contraction was used.

How did roughness affects airfoil performance? The L/D at $480K$ is shown in Chart 25. Tripping only seemed to be beneficial at $16^\circ < \alpha < 18^\circ$. It was especially deleterious at maximum lift and past stall. Tripping at 36% seemed slightly better than 38% with an average of 8% larger L/D at $\alpha < 18^\circ$. The maximum L/D was reduced up to 35.3% with tripping having a deleterious effect on airfoil performance. This raised the question if laminar separation at lower Re 's could be avoided without the deleterious effect on performance at higher Re 's.

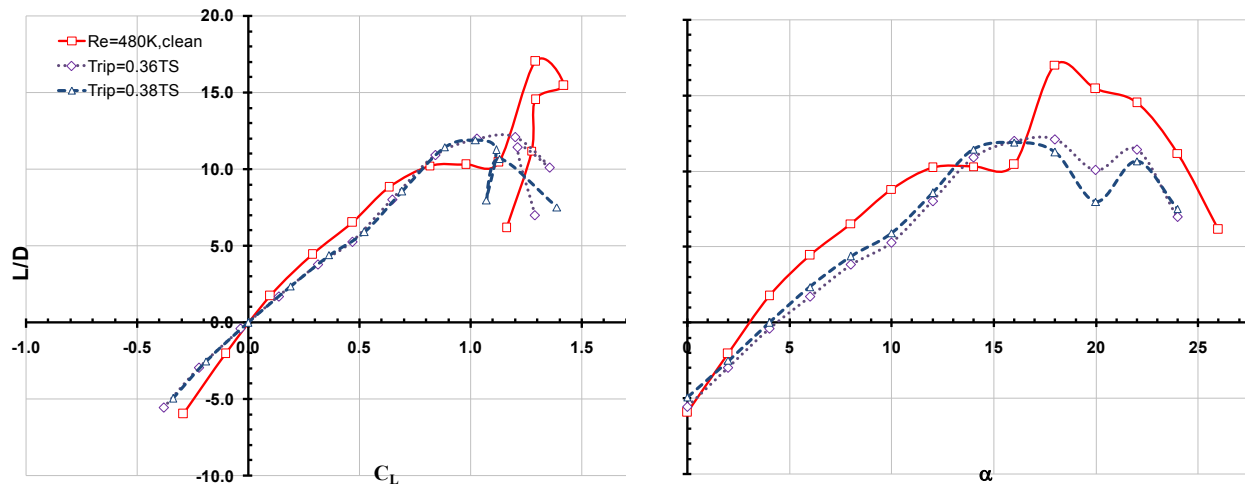


Chart 25. L/D vs. C_D and $Re = 480K$. Roughness at $x/c = 0.36$ TS and 0.38 TS was applied. The airfoil configuration C with original contraction was used.

Hysteresis, and $Re = 320K$, was eliminated through application of roughness at $x/c = 0.36$ on the TS, which removed the laminar separation bubble by fixing the BL transition location. Applying roughness at $x/c = 0.56$ on the BS improved C_D additionally for $12^\circ < \alpha < 18^\circ$ by removing another laminar separation bubble.

C_L and C_D were extremely sensitive to the location of the roughness at $Re = 480K$. A $\Delta(x/c) = 0.02$ caused a $\Delta C_L = 0.3$ at $\alpha = 20^\circ$. At this Re roughness had an overall deleterious effect on L/D .

6.1.9 Quarter Chord Moment Coefficient Analysis

It is a desirable airfoil characteristic to have zero or constant $C_{m_{c/4}}$ over most of its α range. A predictable airfoil $C_{m_{c/4}}$ is necessary for aircraft stability. An aircraft should have a negative pitching moment in order to prevent unstable pitch break behavior.

The $C_{m_c/4}$ vs. α for a clean and rough airfoil are compared in Chart 26. The airfoil in configuration C with added contraction was used. The tripped case at $x/c = 0.36$ with $Re = 112K$ showed similar trends to the clean airfoil $Re = 480K$ case. It was concluded that roughness could have similar effects as Re on $C_{m_c/4}$.

For $Re = 480K$ the $C_{m_c/4} = 0$ at $\alpha = 0^\circ$ and decreased approximately linearly to $C_{m_c/4} = -0.08$ at $\alpha = 20^\circ$. $C_{m_c/4}$ varied on average from 0.08 to -0.08 over the entire range of α 's.

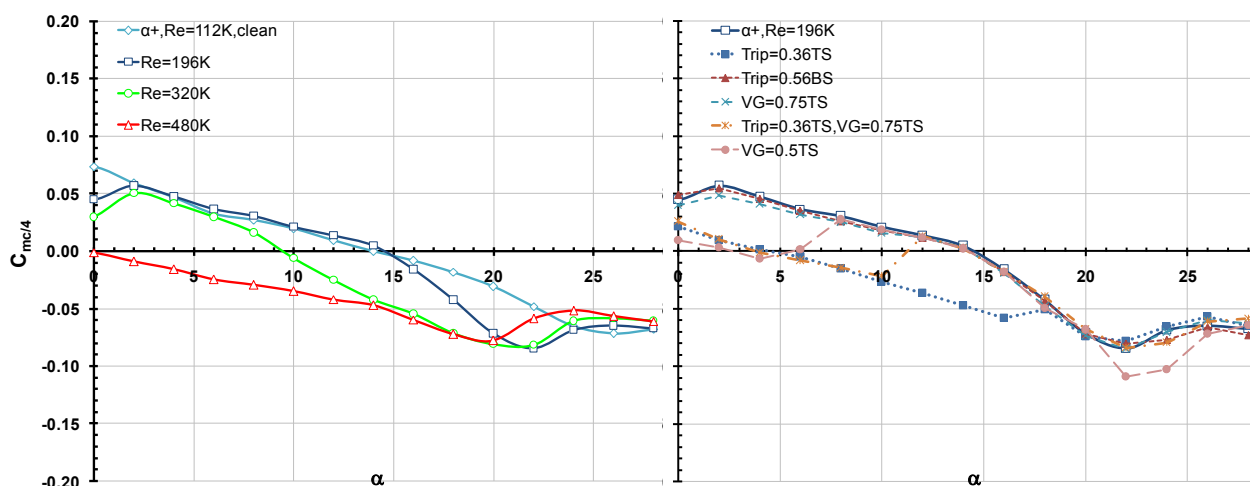


Chart 26. Baseline study of $C_{m_c/4}$ vs. α at 7 m/s, 12 m/s, 18 m/s, 20 m/s and 30 m/s for a clean airfoil and 12 m/s for an airfoil with various applied roughness strips and vortex generators. The airfoil tested was in configuration C and the added contraction was used.

A $C_{m_c/4} = 0$ was only realized at $\alpha = 0^\circ$ for high Re 's. For low Re 's, TS VG's at x/c

$= 0.5$ achieved a $C_{m_c/4} = 0.01$ at $\alpha = 0^\circ$.

$$\frac{\partial C_{m_c/4}}{\partial \alpha}$$

= 0.004 at $Re = 480K$. With increasing Re curves shifted downwards by 0.05 comparing $Re = 112K$ to $480K$. At intermediate Re 's there is a transition that gradually starts at higher incidence and then slowly expands over smaller incidence at ever increasing Re 's.

For $Re = 480K$ $C_{mc/4}$ decreased from zero to negative 0.08 in a linear fashion. At $Re = 112K$ and TS BL tripping at $x/c = 0.36$ showed a similar trend.

6.2 AFC Results

Several AFC control methods were applied to the modified GLAS II at two different slot locations to improve baseline performance by preventing and/or delaying flow separation, removing separation bubbles, inducing turbulent BL transition, and predictably controlling lift and/or drag. The control method efficacy was analyzed as well. The effect of AFC on various flow features such as streamwise/ spanwise vortices, laminar/turbulent separation bubbles and the stagnation point location were also of interest.

6.2.1 Case Study to Verify Glauert's Data

Initially steady external suction and blowing through Glauert's originally proposed 69.3% slot in airfoil configuration A was applied. Unfortunately, only C_{dp} was measured at the time. The goal was to reproduce the promising results of Glauert from 1948. He effectively reduced C_D and increased C_L for $Re = 960K$ arriving at maximum $L/D = 566$ with suction $c_{\mu} = 5.27\%$ at $\alpha = 16.9^\circ$. Glauert used a minimum suction approach in which the suction c_{μ} varied from $\sim 0.75\%$ for $\alpha < 10^\circ$, after which it rapidly increased, to \sim

5.27%, in order to keep the flow attached over the ramp. Blowing quantities required much larger c_μ 's, linearly increasing from 12.4% at $\alpha = -8^\circ$ up to 23.2% at $\alpha = 16.9^\circ$.² The conversion in Equation (14) was used to find c_μ from the mass flow C_Q . His Glas II's $h = 2.54$ mm and $c = 76.2$ cm.

$$c_\mu = \frac{2h}{c} \left(\frac{U_{jet}}{U_\infty} \right) = \frac{2h}{c} \left(\frac{C_Q c}{h} \right)^2 \quad (14)$$

During Undergraduate 2004 experiments at first, one blower was used. However, it soon became obvious that a second blower was needed since no significant C_L or C_{dp} improvements had been achieved for suction or blowing. A second blower was used to increase c_μ and attempt flow reattachment over the ramp. The blowing and suction c_μ 's corresponded to the maxima for the given blower, slot and ducting configuration.

C_L and C_{dp} during steady AFC are compared to the baseline for $Re = 335K$ in Chart 27. C_{dp} should only be viewed as an indicator of C_D trends and not as a reliable quantitative measure. In addition one had to be careful as at high α 's, pressure drag defied any resemblance to C_D .

Suction appeared effective at delaying stall by 22.2% and increasing C_{Lmax} by 6.25%. An increase in suction c_μ by 23.3% did not improve C_L or C_{dp} noticeably. Blowing had a deleterious effect on C_L at all $\alpha > 15^\circ$, but had a positive effect between $11^\circ < \alpha < 14^\circ$.

This analysis was focused on matching historical results only and a detailed control method efficacy study will be shown in Sections 6.2.4 to 6.2.8.

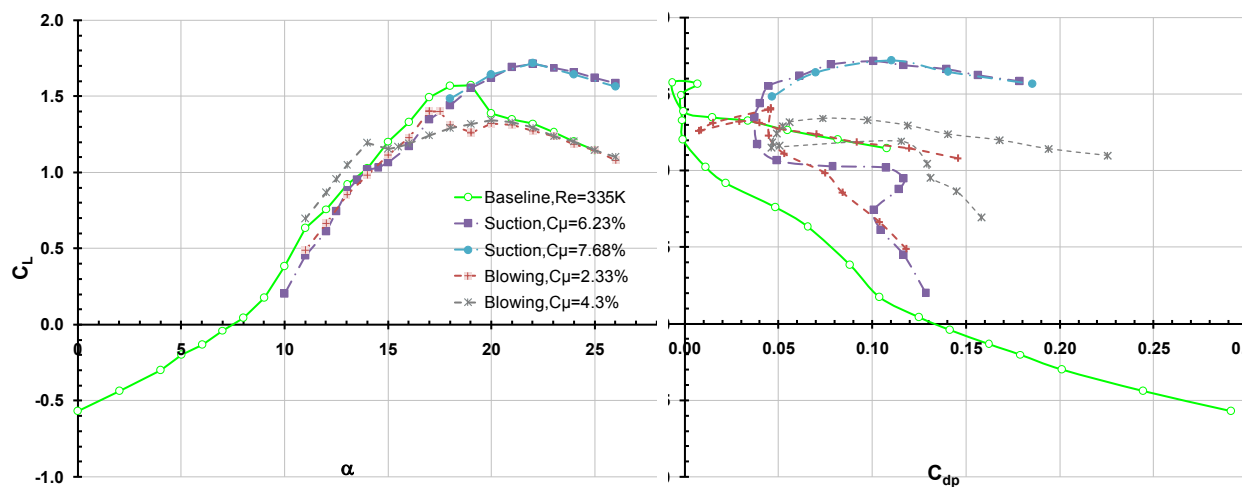


Chart 27. Steady AFC study of C_L vs. α and C_{dp} at 20 m/s. The airfoil was clean and two centrifugal type blowers were used in airfoil configuration A using the original contraction.

The L/D_p performance vs. C_L and α during suction and blowing is compared to baseline in Chart 28. The maximum L/D_p at $C_L = 1.4$ was ~ 36 for suction at $c_{\mu} = 6.23\%$. Suction widened the performance peak, which would allow to operate L/D_{pmax} during higher C_L portions of the flight envelope. Blowing at $c_{\mu} = 2.33\%$ seemed to be more effective at lower α 's.

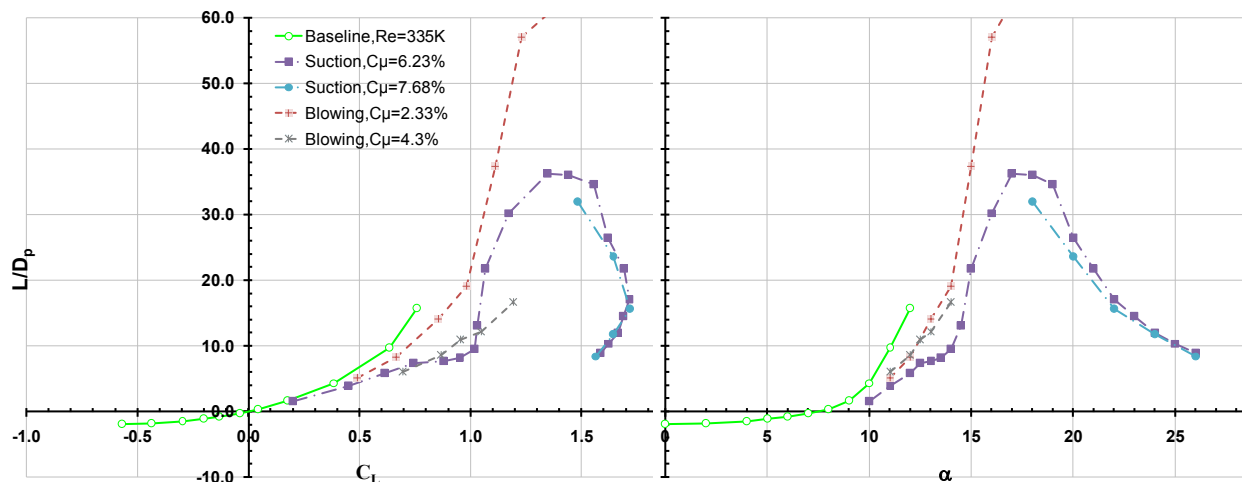


Chart 28. Steady AFC study of suction and blowing L/D_p vs. C_L and α at 20 m/s.

The same steady AFC experiment was repeated for $Re = 480K$ shown in Chart 29. $C_{L_{max}}$ was reduced substantially compared to the $Re = 335K$ case by 0.6. Stall at $\alpha \approx 17^\circ$ was not very pronounced and the ΔC_L before compared to past stall was only 0.12. Possible turbulent separation with early transition caused major loss in lift. Suction delayed stall by 4° while blowing was deleterious and promoted early stall by 3° . Blowing had a positive effect in the range $3^\circ < \alpha < 12^\circ$. C_L improvements were marginal due to lower c_{μ} 's of 3.41% and 1.91% for suction and blowing respectively.

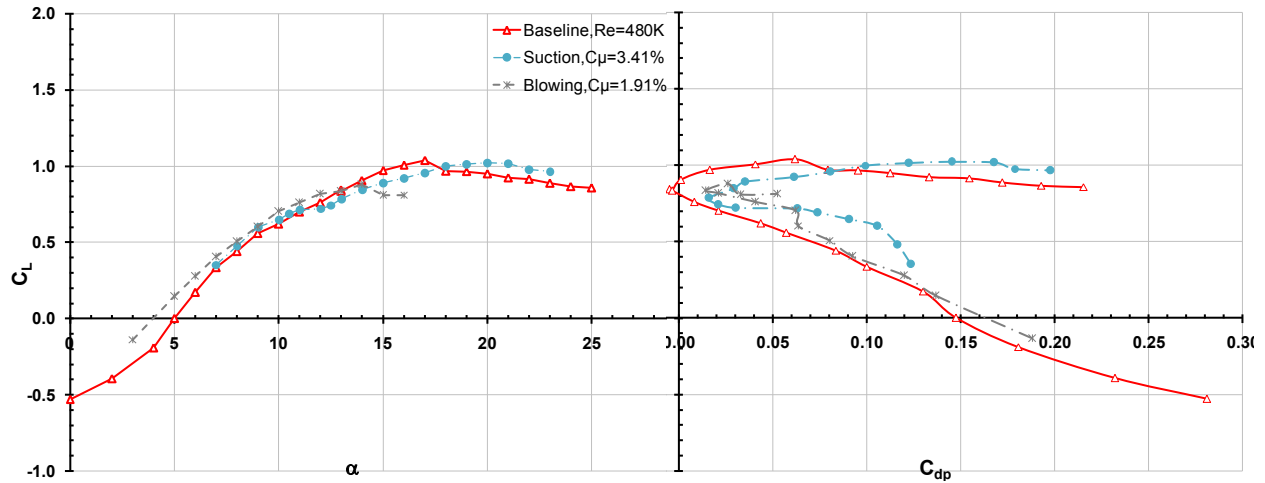


Chart 29. Steady AFC study of C_L vs. α and C_{dp} . Tests were done at 30 m/s for a clean airfoil with airfoil configuration A using the original contraction.

The L/D_p was analyzed in Chart 30. Blowing and suction $L/D_{pmax} = 60$ and 50 and were realized around $C_L = 0.9$, 0.8 respectively. However, the validity of the sharp L/D_{max} peak is questionable, because L/D_{max} so far had exhibited a smoother behavior around stall.

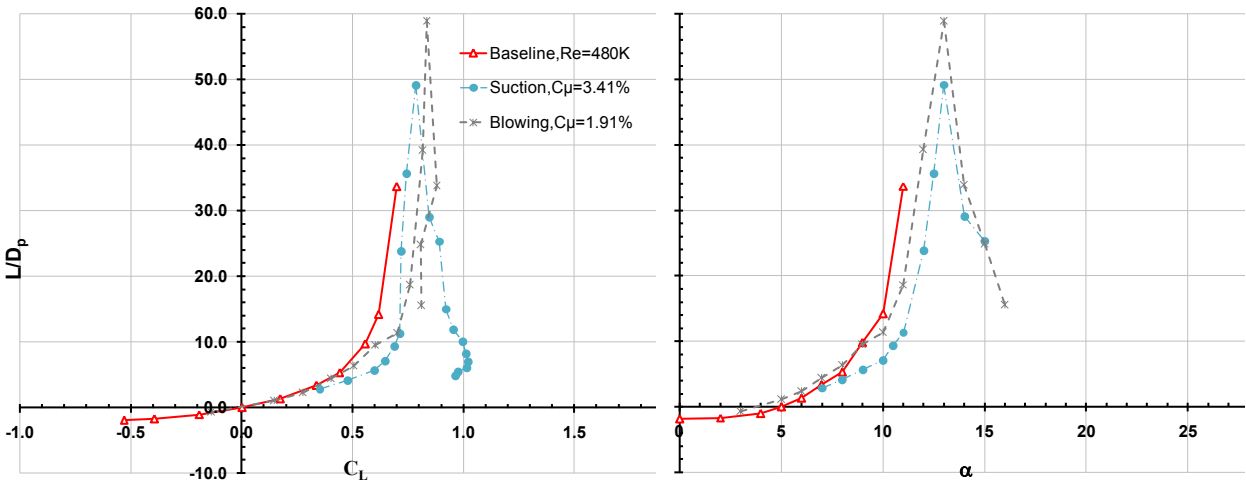


Chart 30. Steady AFC study of L/D_p vs. C_L and α . Tests were done at 30 m/s for a clean airfoil.

The suction/ blowing C_L , and the suction C_D for $Re = 480K$ are compared to Glauert's in Chart 31. C_D was not available for Glauert's blowing case.

Blowing reduced α_s by 1° during Glauert's experiments. For suction no α_s was available. Suction was much more effective at only $\sim 1/5$ the required c_{μ} compared to blowing. The $C_{L_{max}}$ increased from 1.4 to 1.8 during blowing.

For Scobee tunnel 2004 experiments at the highest investigated $Re = 480K$ only reached a $C_{L_{max}} = 1.05$. The low $C_{L_{max}}$ could have been due to surface roughness discussed in Section 6.1.8 and Chart 24 or Re effects discussed in Section 6.1.3 at $Re \geq 1210K$. Blowing had a deleterious effect on $C_{L_{max}}$ reducing it by 0.2. Suction did not change $C_{L_{max}}$. Suction at $c_{\mu} = 3.41\%$ delayed stall by 4° while blowing at $c_{\mu} = 1.91\%$ advanced stall by 3.5° .

Glauert's theoretical value of the GLAS II's $\frac{dC_L}{d\alpha} = 0.129$ during minimum suction.

Glauert achieved a comparable $\frac{dC_L}{d\alpha} = 0.115$ in his experiments and during

Undergraduate experiments at $\alpha < 5^\circ$, $\frac{dC_L}{d\alpha} \approx 0.085$, and at $\alpha > 12^\circ$, $\frac{dC_L}{d\alpha} \approx 0.055$. There

appeared to be a transition region similar to the one discovered in Section 6.1.3.

Due to Glauert's minimum suction approach, C_D was nearly constant for all α 's. He used the smallest c_{μ} required, for every α , to keep the ramp turbulently attached. According to Glauert, the remaining C_D was only due to the unsucked BL on the BS. For suction, he only presented data for $\alpha < 16.9^\circ$ after which minimum suction failed to keep the ramp from stalling.

In order to reduce C_D even further he improved on the GLAS II design with his GLAS III having two suction slots one on the TS at $\sim 69\%$ chord and one on the BS at $\sim 75\%$ chord. Thereby, he hypothesized that the entire BL could be removed eliminating airfoil C_D .

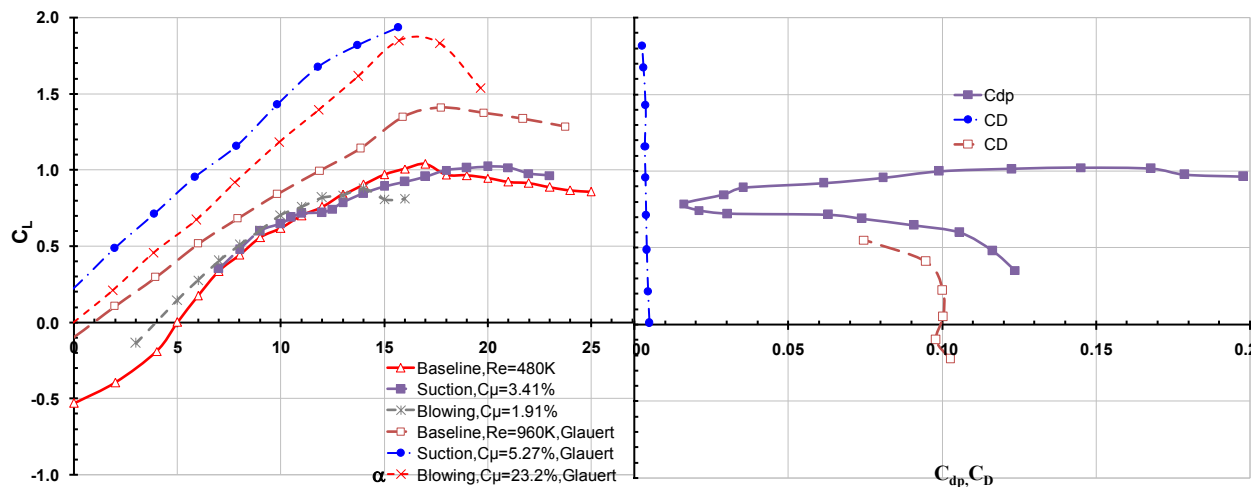


Chart 31. Steady AFC study of C_L vs. α and C_{dp}/C_D at 20 m/s for a clean airfoil. Undergraduate 2004 data using the original contraction was compared to Glauert's data.²

The suction L/D based on Glauert's C_D and Scobee tunnel C_{dp} is shown in Chart 32. Suction $L/D_p = 50$ was much lower than Glauert's $L/D = 566$ at $\alpha = 12^\circ$. Glauert only needed a suction $c_{\mu} = 1.5\%$, at $\alpha < 10^\circ$, to keep the ramp attached. No ramp attachment/reattachment was achieved during the Scobee tunnel 2004 experiments at any available c_{μ} .

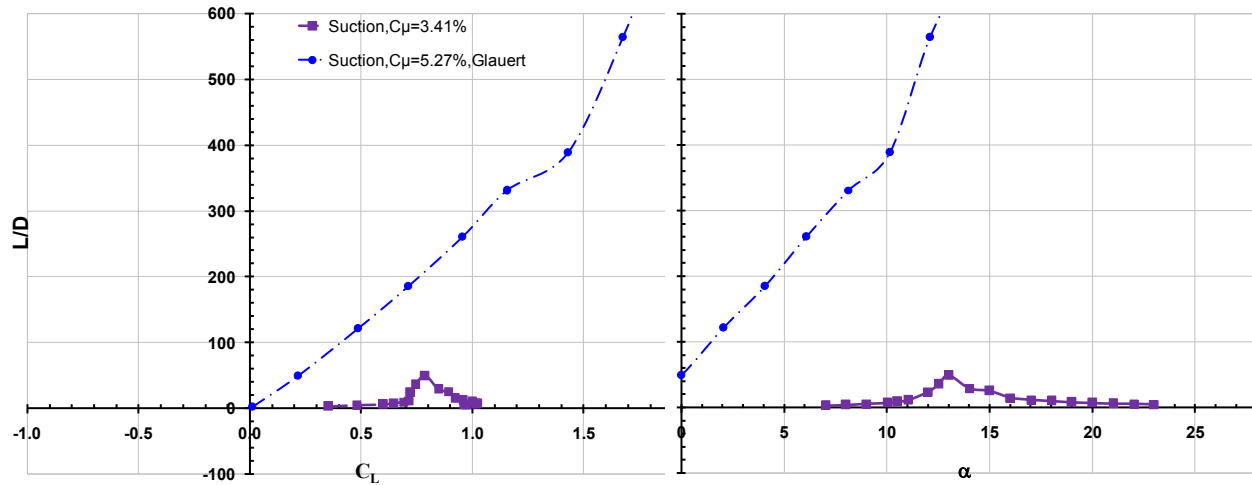


Chart 32. Scobee tunnel 2004 suction AFC study of L/D_p vs. C_L and α compared to Glauert's L/D performance 20 m/s but very different Re 's for a clean airfoil.

Performance did not compare to Glauert's. Suction did not increase $C_{L_{max}}$ significantly. Blowing was deleterious on $C_{L_{max}}$ and α_s . Baseline and steady AFC performance did not differ significantly.

The type of actuation, the c_{μ} , or the actuation location was inadequate. The control authority was limited by the achievable steady $c_{\mu_{max}}$, based on the available blowers and the airfoil's ducting design. Hence, the slot or actuation location was modified first. This triggered a new study determined to locate a more effective slot location at achievable steady c_{μ} 's and at available Re 's, which the Aerodynamics Laboratory wind tunnel facilities could provide.

6.2.2 CFD ZMF Actuation Slot Optimization Analysis

The same CFD analysis by Ahmed Hassan from Section 6.1.7 helped explain the reason for ineffectiveness of steady AFC through the 69.3% slot and determine a better actuation location.¹³ The pressure data for the baseline study discussed in Chart 21 was not available at the time, but it indicated separation on the TS at $x/c \approx 0.55, 0.56, 0.56,$ and 0.39 and on the BS at $x/c \approx 0.61, 0.65, 0.67,$ and 0.66 to occur for $\alpha = 0^\circ, 4^\circ, 6^\circ,$ and 8° respectively.

CFD verified some of the observations earlier on by estimating the BL separation location. For baseline results, the BL laminar separation locations were shown in Figure 26. The TS separated at $x/c \approx 0.73, 0.6, 0.55,$ and 0.54 for $\alpha = 0^\circ, 4^\circ, 6^\circ,$ and 8° . The BS BL did not show any separation but a BL thickening was noticed at $x/c \approx 0.72,$ and 0.76 corresponding to $\alpha = 0^\circ, 4^\circ$ after which the BL appeared to be fully attached.

It is known that the best location to apply ZMF control is immediately ahead of the separation, the location at which the maximum favorable pressure gradient is required to keep the flow attached. Based on CFD baseline results a ZMF actuation CFD study was performed introducing sinusoidal perturbations before TS BL separation in order to validate an optimized slot location.

ZMF control perturbations were introduced at 50% chord with 200 Hz and $C_{\mu} = 0.88\%$ shown in Figure 28 at $\alpha = 0^{\circ}, 4^{\circ}, 6^{\circ},$ and 8° . The u velocity contour plots represent an instant in time with the same $Re = 2,880K$ and grid used as in the baseline cases.

During ZMF control the stagnation point moved much more quickly from the LE TS to the LE BS within $0^{\circ} < \alpha < 8^{\circ}$ compared to the CFD baseline analysis.

With ZMF actuation, the wake region at all α 's was significantly reduced. The TS stayed attached up to $x/c \approx 0.76, 0.66, 0.59, 0.60$ delaying separation by 3.7%, 10%, 7.3%, and 11.5% for $\alpha = 0^{\circ}, 4^{\circ}, 6^{\circ},$ and 8° . After initial separation a thickening of the BL was noticed, especially at $\alpha = 4^{\circ}$ and 6° .

ZMF control creates a separation bubble on the ramp BS between $0.76 < x/c < 1.0$ and $0.81 < x/c < 1.0$ corresponding to $\alpha = 0^{\circ}$ and 4° . At higher α 's the bubble seems to disappear.

During forcing much larger amplification of “vortical” style structures occurred within the shear layer. These almost matched the shedding wavelength of 0.27, assuming shedding was locked into the forcing frequency and might be regarded as shedding vortices. The bottom surface (BS) shear layer exhibited velocity contour structures at similar wavelengths to the one on top, though with greatly decreased amplitude. These were probably due to the induced forcing disturbances at the slot through oscillations of the entire flow field around the GLAS II.

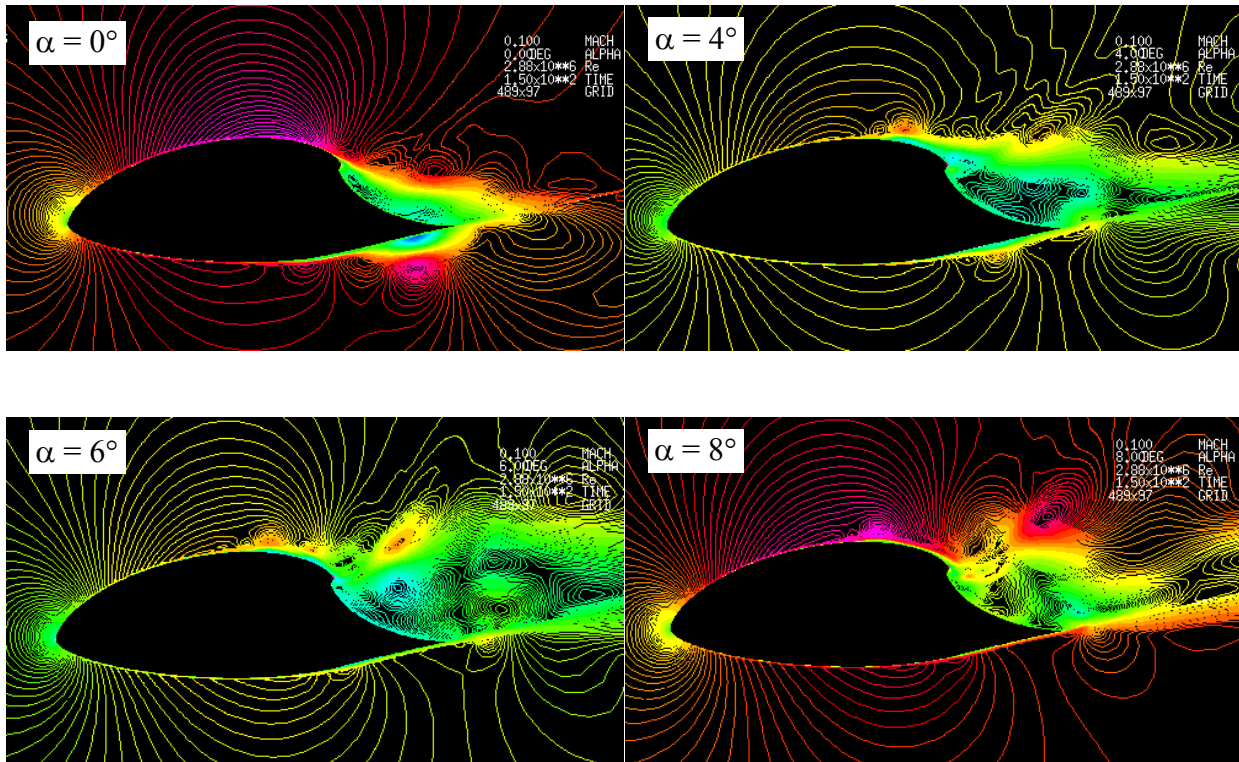


Figure 28. CFD study of u velocity contours around the GLAS II. The computations were performed at 54.9 m/s and $\alpha = 0^\circ, 4^\circ, 6^\circ,$ and 8° . ZMF control disturbances were introduced at 59% chord with 200 Hz and $C_{\mu} = 0.88\%$.¹³

The stagnation point might be affected by ZMF control improving the airfoil's circulation. It appeared as if the stagnation point moved more rapidly to the LE BS than would be the case during baseline, for increasing α .

CFD suggested an effective slot location at 50% chord with noticeable reduction in wake size. A reduced wake size would equal a decreased C_D . Additionally, the delay in TS flow separation by about 10% would likely increase C_L by enlarging the suction peak.

ZMF control might inadvertently produce a separation bubble on the ramp's BS at low α 's.

6.2.3 The Importance of Slot Location (69.3% vs. 59%)

It was decided to place the slot on the upper loft at 59% chord right in-between Glauert's 69.3% location shown to be effective by CFD at 50% chord. The hope was that AFC would still be able to improve flow attachment, at least up to the new slot location.

Chart 33 compares data from Section 6.2.1 to data acquired with the new slot in the Davis wind tunnel with airfoil configuration B at $Re = 352K$. Suction through the 69.3% chord slot, improved C_{Lmax} by 6.25% and α_s by 4° . With the updated slot, suction and blowing improved C_L by 175% and 300%, respectively. Improvement was realized over the entire range of α up until stall. Beyond stall, the 69.3% slot with suction was more effective than the 59% chord slot. Steady suction C_L past stall, e.g. at $\alpha = 24^\circ$, was improved by 36.7% for the old and 30.7% for the new slot. $\frac{dC_L}{d\alpha}$ for the 69.3% and 59% slot with suction was $\approx 0.135 \frac{\Delta C_L}{\Delta \alpha}$ and $0.113 \frac{\Delta C_L}{\Delta \alpha}$, respectively. $\frac{dC_L}{d\alpha} = 0.135$ deviated from Glauert's theoretically predicted value for suction by 4.49% while $\frac{dC_L}{d\alpha} = 0.113$ deviated by 12.5%.

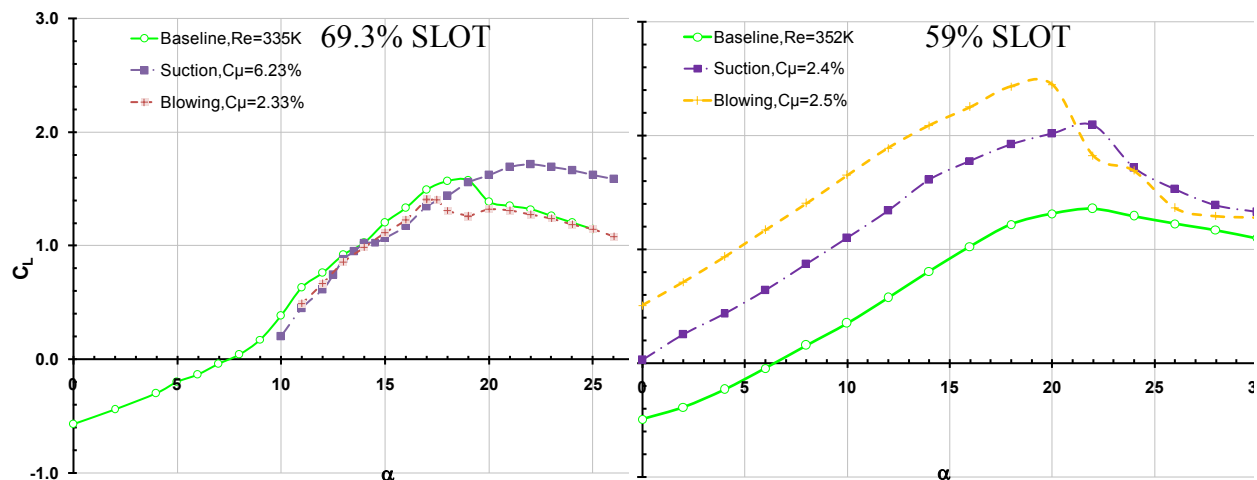


Chart 33. Slot optimization study of C_L vs. α at 20 m/s. The 69.3% chord slot efficacy, with $h = 0.711$ mm, was compared to the optimized 59% chord one, with $h = 0.813$ mm slot.

The new slot location was more effective than the old one for steady suction and steady blowing. A 10% change in slot location had a large positive effect on flow control authority. Suction and blowing improved C_L by 175% and 300%, respectively. Past stall forcing through the old slot became beneficial.

6.2.4 Steady vs. Unsteady AFC through 59% Slot at $Re = 117K$

The efficacy of the 59% chord slot was evaluated using steady and unsteady external forcing techniques in airfoil configuration B within the Davis wind tunnel. The C_D was not available for all cases and C_{dp} was used in the analysis if useful. It should be recalled that C_{dp} only signified C_D trends and not quantitative data in particular when flow control was used.

Aerodynamic coefficients with steady forcing are compared to ZMF control results at $Re = 117K$ shown in Chart 34. Baseline C_D data was used from Section 6.1.1 because

C_D data collected in the Davis wind tunnel at $Re = 117K$ was flawed. All AFC methods significantly improved C_L and C_D . Blowing at $c_\mu = 24.5\%$ produced the highest $C_{Lmax} = 5$ at $\alpha = 24^\circ$, a $\Delta C_L = 4.2$ compared to baseline. Suction at $c_\mu = 19\%$ and ZMF control at $C_\mu = 5.7\%$ followed with $C_{Lmax} = 3.5, 3.4$ and a $\Delta C_L = 2.7, 2.6$ respectively.

During forcing, $\frac{\Delta C_L}{\Delta \alpha} \approx \text{constant}$ at $\alpha < 20^\circ$ and $C_L > 0$ at $\alpha = 0^\circ$. Thus, forcing was able to eliminate the TS laminar separation bubble while keeping the flow attached, with exception of the ramp. This was the case even with the high upstream wind tunnel turbulence levels experienced in the Davis wind tunnel.

ZMF actuation compared to blowing at $\alpha < 20^\circ$ at only $\frac{1}{4}$ of the required momentum input. During ZMF control, the airfoil stalled much more gently with a wider maximum lift peak compared to the narrow peaks for suction and blowing. With the new slot, all forcing methods were effective in reducing drag. The added momentum injected in the direction of streaming during blowing was so large that it overcompensated for C_D , essentially producing thrust, which resulted in $C_D = -0.2$ being negative.

C_D could have been corrected for by adding the jet C_μ/c_μ for ZMF forcing, blowing and suction. None of the C_D 's analyzed in this paper were corrected. Because, it was difficult to measure how much of the 2D blowing, suction, and ZMF control momentum was actually recovered three airfoil chord lengths downstream within the wake.

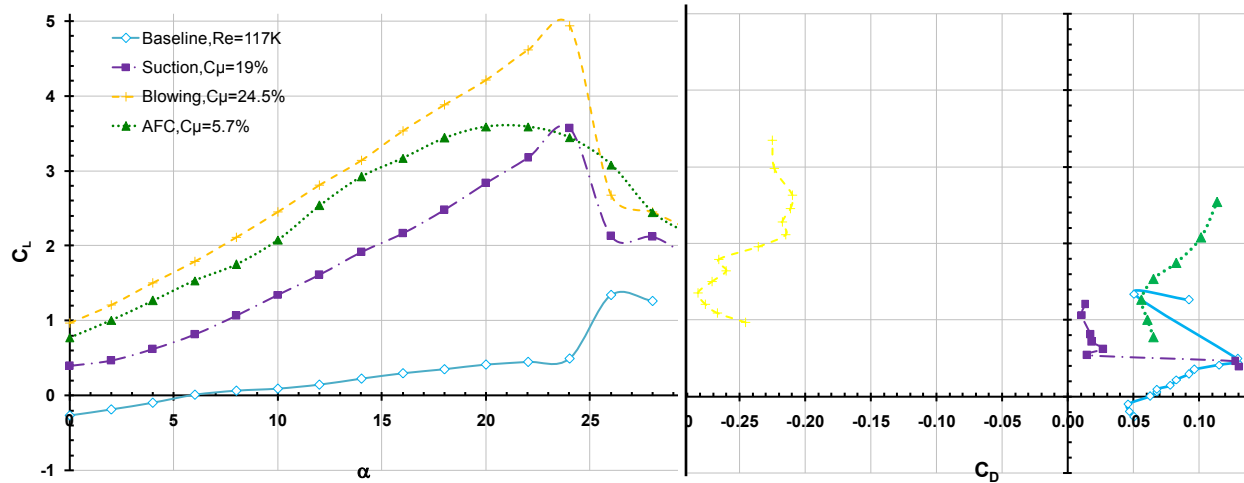


Chart 34. AFC study of the C_L vs. α and C_D at 7 m/s for a clean airfoil in configuration B. $h = 0.711$ mm and $c = 25.16$ cm.

The L/D performance is analyzed in Chart 35. The second chart from the left with blowing showed equivalent thrust performance (L/T) at given C_L . Suction was effective with $L/D_{\max} = 100$ at $C_L = 1$. At $C_L = 0.6$ there was a drop in L/D followed by an immediate recovery at larger α 's. This behavior was discussed in Section 6.1.6 and was attributed to a bubble sitting on the BS at $x/c \approx 0.6$.

AFC did not improve L/D_{\max} but was able to prevent sudden lift loss and drag increase by either reducing the separation region around 50% chord on the TS or forcing the separation bubble to stay attached longer.

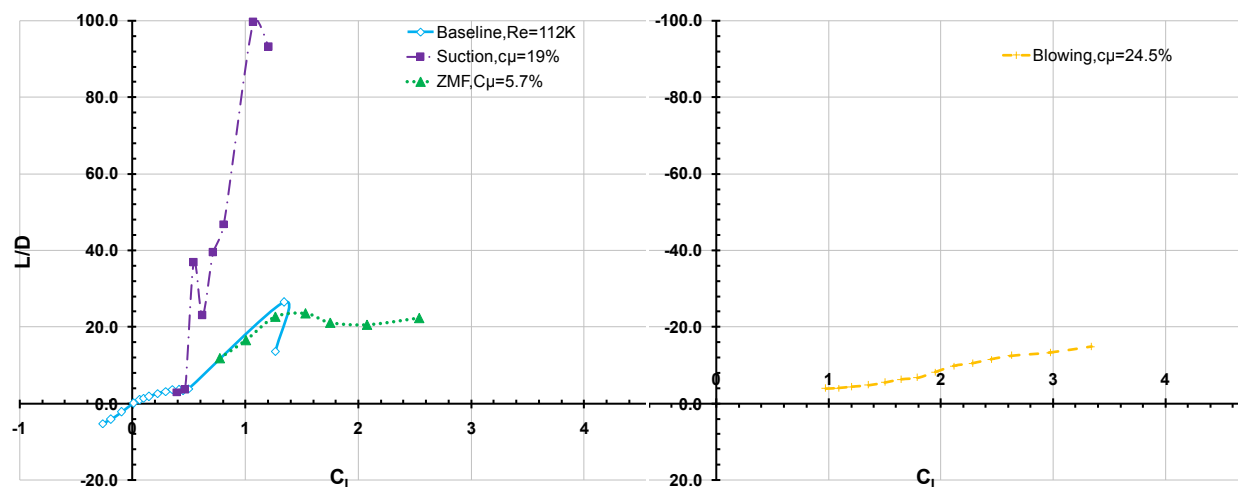


Chart 35. AFC study of L/D and L/T vs. C_L at 7 m/s for a clean airfoil in configuration B.

Large C_L improvements were realized for all AFC methods with benefits using ZMF forcing at $\sim 1/3$ of the required C_{μ} .

ZMF control was not effective in increasing the L/D_{\max} , but was effective at delaying stall. ZMF forcing created a broader performance peak, which would be beneficial for safer aircraft operation over a larger range of C_L . The aircraft would be more versatile in conforming to different mission requirements. ZMF was able to produce the second highest zero incidence C_L at $1/3$ of the momentum input.

Suction was most effective in increasing C_L and L/D through wake size reduction. The downside was a narrow performance peak. If the flight envelope during a mission would change, e.g. due to loss in engine power, the result could be disastrous. Hence, due to safety constraints the aircraft could only fly at maximum $C_L < 0.82$.

Blowing increased C_L the most but its' L/D was inconclusive due to inadvertently producing thrust.

Momentum inputs ranged from 5.7% - 24.5% , which were very large and not very practical. A more detailed ZMF control analysis, at lower C_μ 's, will be discussed in following Sections.

6.2.5 Steady vs. Unsteady AFC at $Re = 235K$

The same forcing methods used in 6.2.4 were compared at $Re = 235K$ in Chart 36. The actuator momentum input was kept constant for $Re = 117K$, $235K$ and $352K$ and C_μ decreased proportionally as $(U_{\infty 1}(7 \text{ m/s})/ U_{\infty 2}(14 \text{ m/s}))^2$ solely due to increased reference freestream momentum. Resembling the $Re = 117K$ actuation cases there were no changes in $\frac{\Delta C_L}{\Delta \alpha}$, thus no TS separation bubble (for a clean airfoil). The C_L at $\alpha = 0^\circ$ was shifted downward by 0.2. ZMF actuation and suction trends compared with 1/5 of the power required for ZMF control. Blowing provided the highest $C_L = 3.2$ and highest average lift gain of 1.7 between $\alpha = 0^\circ - 20^\circ$ compared to baseline.

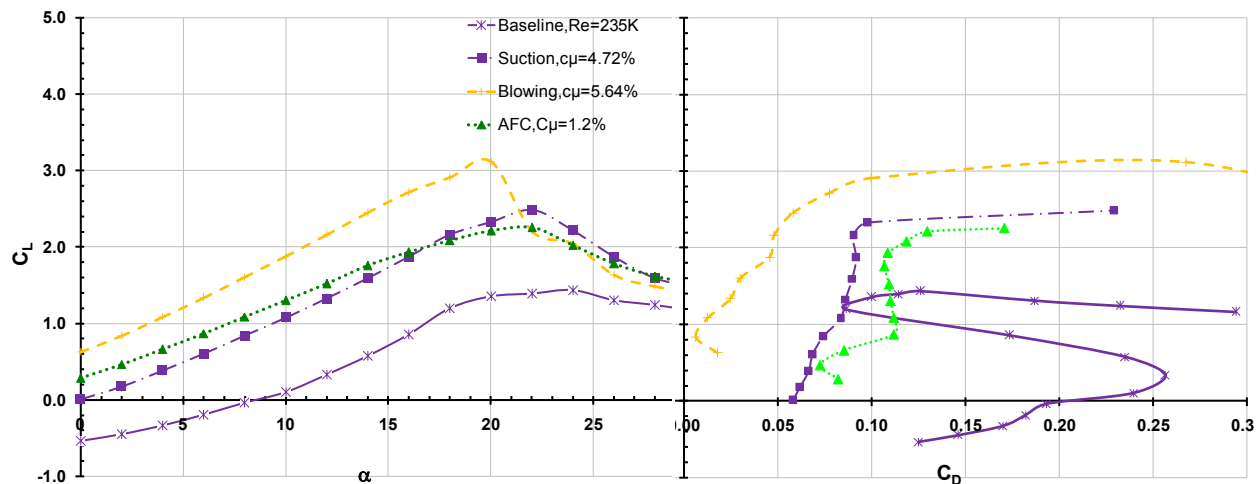


Chart 36. AFC study of C_L vs. α and C_D at 14 m/s for a clean airfoil with moderate C_{μ} 's.

The L/D performance is shown in Chart 37. For ZMF control the $L/D_{max} = 17.8$ at $\alpha = 16^\circ$, for suction 23.9 at $\alpha = 18^\circ$, and for blowing 21.4 at $\alpha = 14^\circ$ a substantial L/D improvement over baseline of 20.5%, 41.4% and 34.6% respectively.

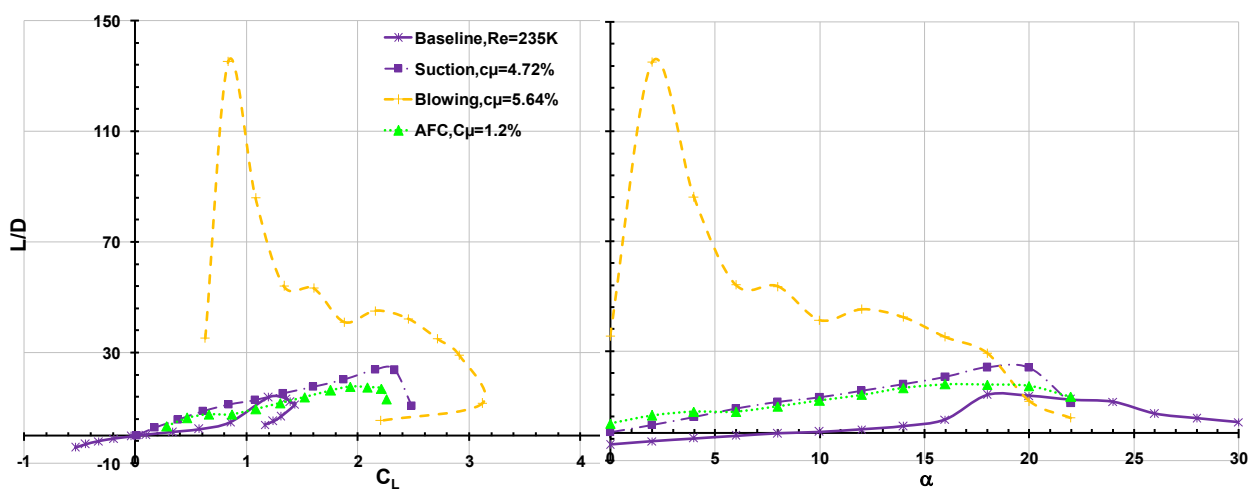


Chart 37. AFC performance study of L/D vs. C_L and α at 14 m/s for a clean airfoil with moderate C_{μ} 's.

6.2.6 Steady vs. Unsteady AFC at $Re = 352K$

The same forcing methods from Section 6.2.5 are compared at $Re = 352K$ in Chart 38. Unfortunately, no C_D measurements were made for steady or unsteady AFC. ZMF forcing and suction performance agreed well for $\alpha < 20^\circ$ with ZMF control only requiring 1/4 of the power. Blowing provided the highest $C_L = 2.5$ and highest average lift gain of 1.3 between $\alpha = 0^\circ - 20^\circ$ compared to baseline.

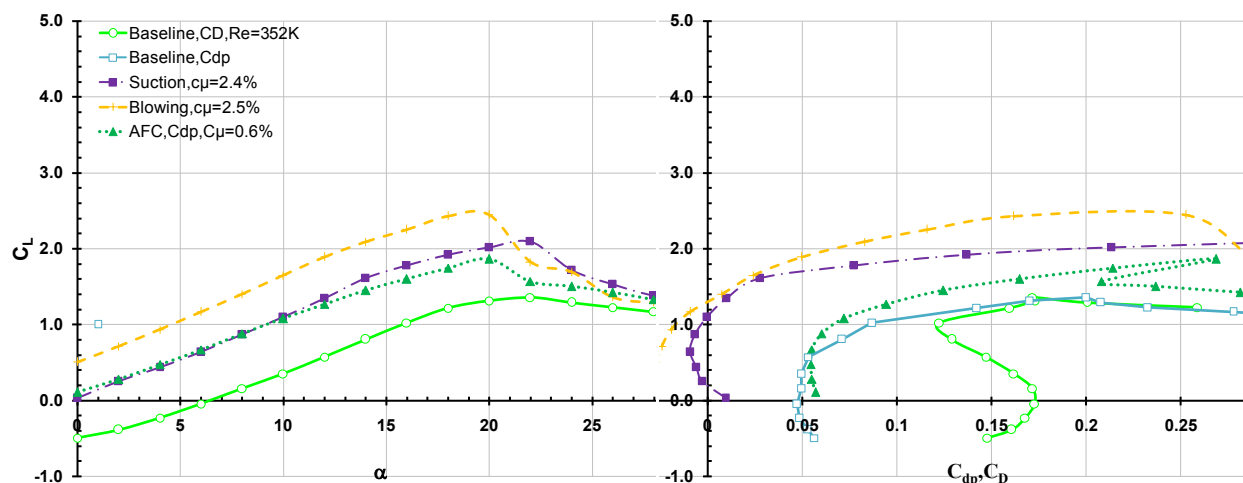


Chart 38. AFC C_L vs. α and C_{dp} & C_D at 20 m/s for a clean airfoil with moderate to small C_μ 's.

The L/D and L/D_p is shown in Chart 39. The baseline C_{dp} and C_D were known while for ZMF actuation only the C_{dp} was acquired. For steady suction and blowing C_{dp} was not physically representative. For ZMF control $L/D_{max} = 14$ at $\alpha = 10^\circ$ a 40% improvement over baseline.

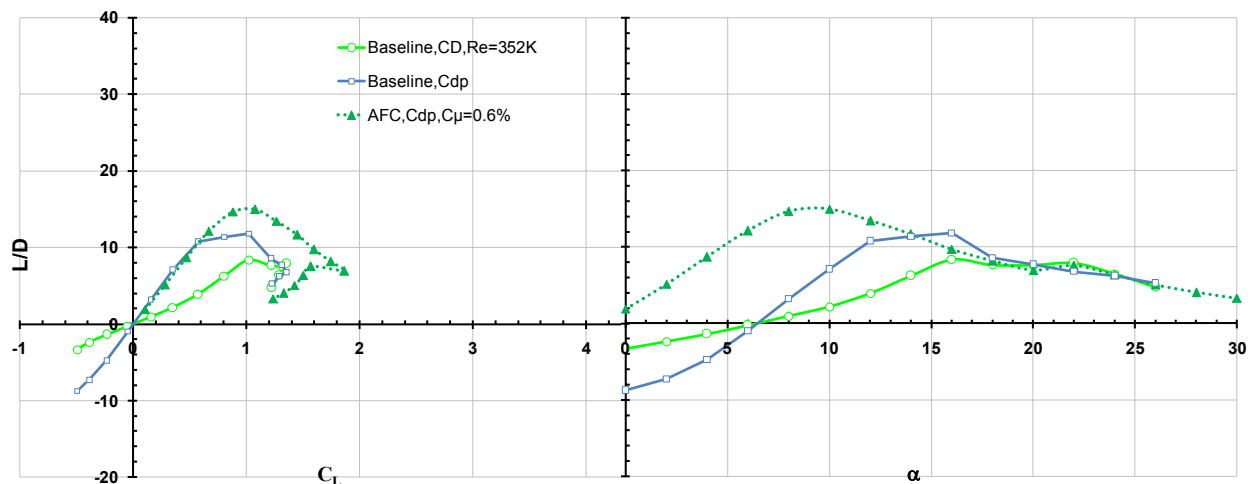


Chart 39. AFC performance study of L/D & L/D_p vs. C_L and α at 20 m/s for a clean airfoil at small C_{μ} .

Section 6.2.4, 6.2.5 and 6.2.6 compared external ZMF AFC to suction and/or blowing AFC. ZMF control had performed exceptional with highest control efficacy. ZMF control required 75.3% less C_{μ} than suction with comparable results at lift penalties of 4.35% for $Re = 117K$ and 37.4% for $Re = 352K$. Compared to blowing at similar C_{μ} savings the C_L penalties were 40.5% for $Re = 117K$ and 58.3% for $Re = 352K$.

Some other important properties are presented in the following table with approximate indicated fractional changes for $Re = 117K$ to $Re = 235K$ and $Re = 235K$ to $352K$. From the table several interesting correlations were derived, whether they were accidental or physically significant would require further testing with many more Re 's. Therefore, correlations should be applied at the user's discretion.

Only minor effect of Re on $C_{L_{max}}$ was apparent for all Re 's under consideration. Hence, it was likely that the BL at α_s separated from the TS at the same x/c independent

on Re. When tripped the C_{Lmax} was reduced by approximately 0.1 for Re = 320K. Whether the BL separated in a laminar or turbulent fashion at that TS x/c location, the resulting C_{Lmax} fell within $\pm 10\%$.

For steady AFC, an increase in Re, from Re_1 to Re_2 , was directly and inversely related to a decrease in ΔC_{Lmax} . For ZMF actuation, no such correlation was apparent. Hence, if a constant c_{μ} would be applied across increasing Re's, C_L improvement, whether it be for steady blowing or suction, would be the same. From 117K to 235K stall happened 2° earlier with exception of ZMF control. From 235K to 352K stall happened another 2° earlier with exception of baseline and ZMF control. The F^+ was 0.28, 0.196 and 0.098 for Re = 117K, 235K and 352K respectively. The apparent reduction in F^+ was solely due to an increase in Re proportional to $(U_{\infty 1}/U_{\infty 2})$.

	Baseline	Blowing	Suction	AFC	Baseline	Blowing	Suction	AFC	Baseline	Blowing	Suction	AFC
Re	117	117	117	117	235	235	235	235	352	352	352	352
C_{Lmax}	1.3	5	3.6	3.5	1.3	3.1	2.5	2.1	1.3	2.5	2.1	1.8
α°	26	23.5	24	21	24	19.5	22	22	22	19.5	22	20
C_{μ}, $c_{\mu}\%$	0	24.5	19	5.7	0	5.64	4.72	1.2	0	2.5	2.4	0.6
$1/\Delta Re\%$	-	-	-	-	0.5	0.5	0.5	0.5	2/3	2/3	2/3	2/3

$ \Delta C_{Lmax} \% $	-	-	-	-	-	1/2	1/2	?	-	2/3	2/3	?
$ \Delta \alpha \% $									110/119			119/130
$ \Delta C_{\mu} \% $	-	-	-	-	1/4	1/4	1/4	1/4	1/2	1/2	1/2	1/2

6.2.7 Effects of C_{μ} and F^+ on Aerodynamic Performance

For ZMF actuation two non-dimensional parameters were generally recognized to allow for good comparisons between data sets and optimize for improved attachment and/or power required to keep the flow attached. These parameters were directly related to the physics of the flow around the airfoil and were discussed in more detail in Section 1.3.1. From previous sections, ZMF control, if applied at the proper location, increased baseline C_L and broadened the C_D peak increasing L/D when integrated over C_L values under investigation. Sufficient C_{μ} 's delayed separation, eliminated bubbles or reduced laminar separation bubble size and forced BL transition at or near the AFC origin. The goal was to find parameters that increase L/D by decreasing C_D or increasing C_L . With the caveat that an increase in C_L also incurred an increase in induced drag for 3D applications that would possibly offset any benefits due to ZMF control.

The effect of C_{μ} and F^+ on C_L and C_D is shown in Chart 40. A clean airfoil in configuration C was tested within the Scobee tunnel using the original contraction setup at $Re = 320K$. The F^+ was four times higher than in Section 6.2.6 for matching

experimental conditions. C_L improved by 28% for $F^+ = 1.2$ over baseline. C_D decreased for all α 's and the separation bubble was removed. The smaller measured C_D compared to Section 6.2.6 was possibly due to the Scobee tunnel's lower $(u')^2$. $F^+ = 1.2$ did better than $F^+ = 1.4$, when it came to decreasing C_D . C_L at $F^+ = 1.2$ was not available. At $F^+ = 1.2$ the vortex shedding frequency was successfully locked to the actuation frequency, thereby organizing the flow structures, preventing meandering and possibly reducing their size shown by the decrease in C_D .

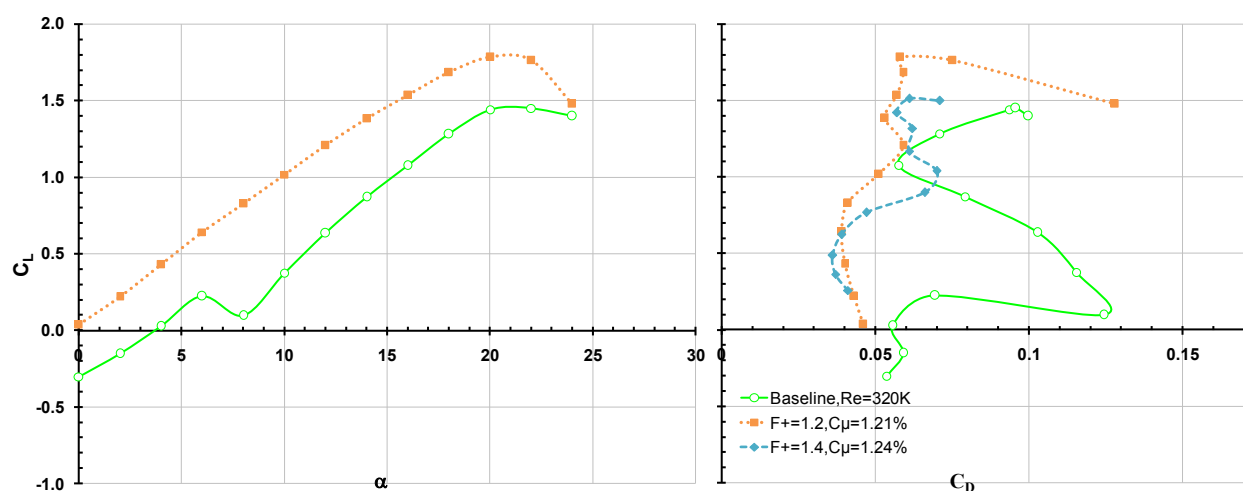


Chart 40. ZMF forcing parameter study of C_L vs. α and C_D at 20 m/s. A clean airfoil in airfoil configuration C with original contraction was used. $L = 11.6\text{cm}$, $h = 0.711\text{mm}$, and $c = 25.16\text{ cm}$.

The L/D performance is shown in Chart 41. The L/D performance increased substantially during ZMF control. With the right selection of F^+ and C_{μ} , large performance increases were accomplished in addition to a wider performance peak and the elimination of laminar separation from the TS.

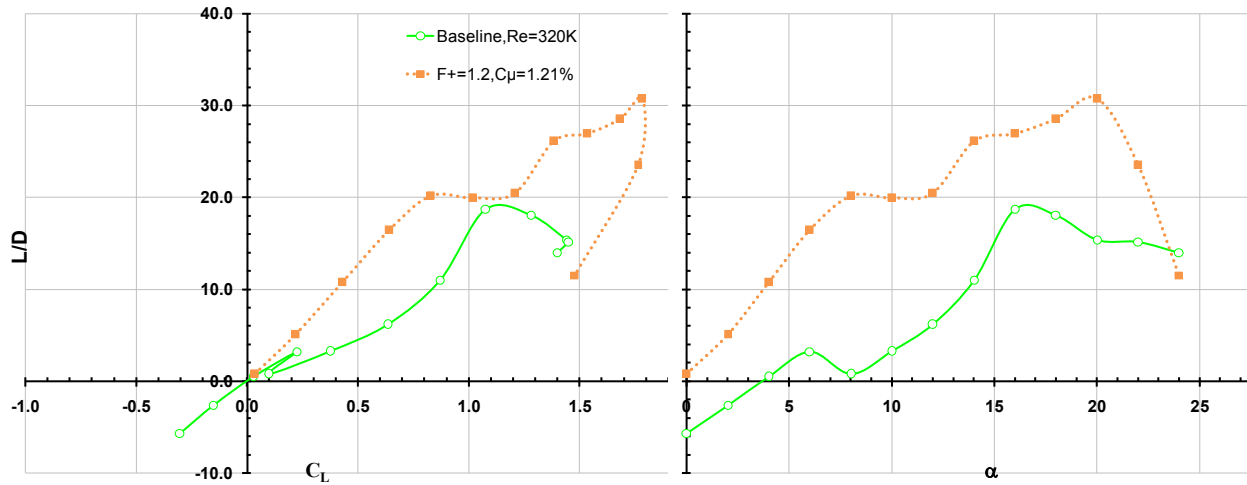


Chart 41. ZMF control parameter study of L/D vs. C_L and α at 20 m/s for a clean airfoil.

The effect of C_μ and F^+ on C_L and C_D is shown Chart 42 for $Re = 480K$ with a clean airfoil. The reduction in C_μ and F^+ was solely due to an increase in Re . C_L was increased by 8% with $F^+ = 1.02$ compared to baseline. The higher the F^+ the less of an effect ZMF actuation seemed to have on increasing C_L , which agreed with $Re = 320K$ results. For $F^+ = 0.8$, 0.93 stall was reduced by 2° while with $F^+ = 1.2$ the airfoil stalled at $\alpha = 20^\circ$ equal to baseline. The $C_\mu = 0.29\%$ for the $F^+ = 1.2$ case was not adequate in reducing drag at $\alpha > 14^\circ$.

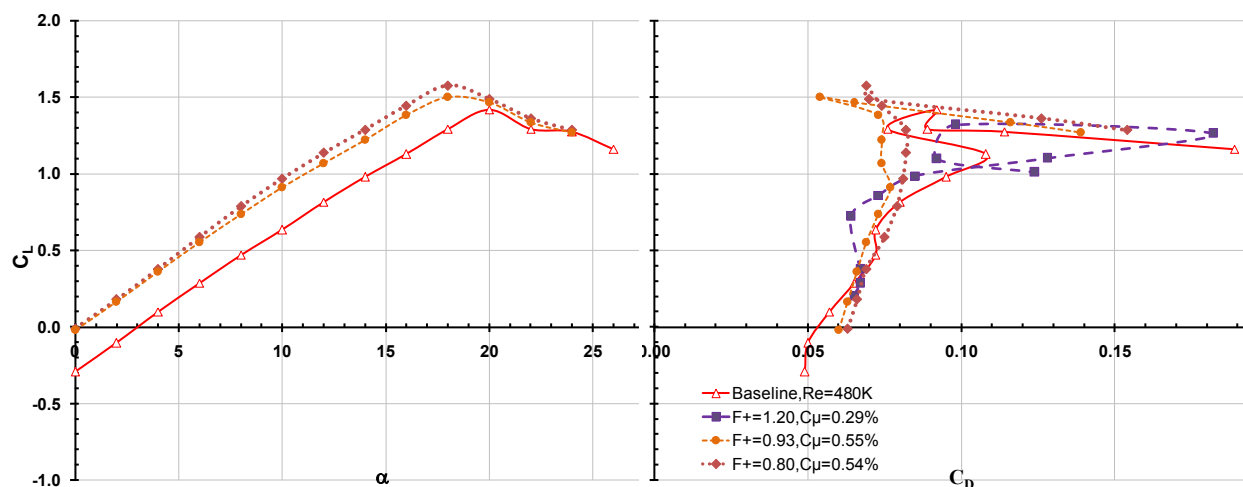


Chart 42. ZMF control parameter study of C_L vs. α and C_D at 30 m/s for clean airfoil. The Scobee tunnel with the original contraction was used.

L/D performance is shown in Chart 43. The drop in baseline L/D between $12^\circ < \alpha < 18^\circ$ was likely caused by a separation bubble on the TE BS, because no corresponding drop in C_L was seen. For $F^+ = 1.2$ the reduction in L/D occurred over $13^\circ < \alpha < 20^\circ$ and was likely caused by that same bubble. Lower F^+ forcing might have amplified the instability thereby increasing its' size resulting in higher airfoil C_D . At $\alpha > \alpha_s$ the bubble had completely separated from the BS and the flow had completely reattached. For ZMF control at $F^+ = 0.8, 0.93$ the laminar separation bubble seemed to disappear with no recorded drop in L/D over the same α range compared to baseline. $F^+ = 0.93$ was most effective with L/D improvements over nearly all α 's, especially between $12^\circ < \alpha < 21^\circ$ corresponding to $1.05 < C_L < 1.3$. The L/D_{\max} increased by 66.7% over baseline at $\alpha = 18^\circ$. The L/D_{avg} increased by 7 for $\alpha < 12^\circ$.

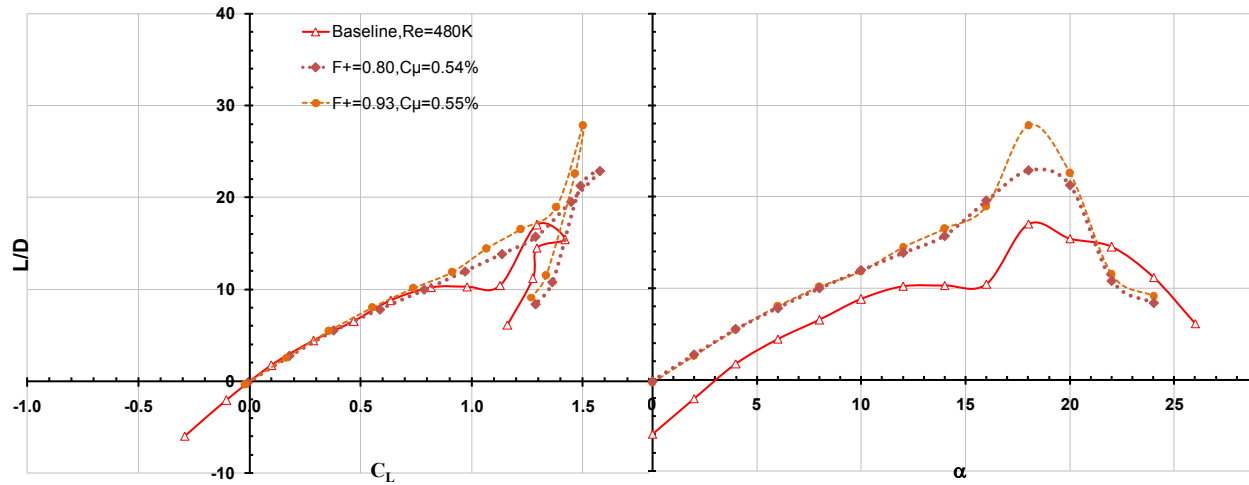


Chart 43. ZMF forcing parameter study of L/D vs. C_L and α at 30 m/s for a clean airfoil.

By choosing a F^+ close to 1 the airfoil's L/D was improved. ZMF control not only provided C_L but also C_D benefits. For ZMF actuation at $Re = 320K$, $F^+ = 1.2$, and $Re = 480K$, $F^+ = 0.8, 0.93$ the TS separation bubble was removed. Additionally, for the latter ZMF control case the BS bubble was removed.

6.2.8 Effects of Roughness on ZMF Control Performance

From previous discussions when using AFC, whether it be steady or unsteady, it became clear that by forcing the TS separation bubble could be eliminated. From Section 6.2.7, it was shown that forcing at $F^+ > 0.8$ might also remove the ramp BS separation bubble discovered in Section 6.1.8. This was true without any tripping or applied roughness. How then is the performance affected by tripping and ZMF forcing simultaneously? Chart 44 shows the effect of roughness on ZMF control performance for $Re = 320K$. The airfoil was in configuration C and was tested within the Scobee tunnel and the original contraction setup.

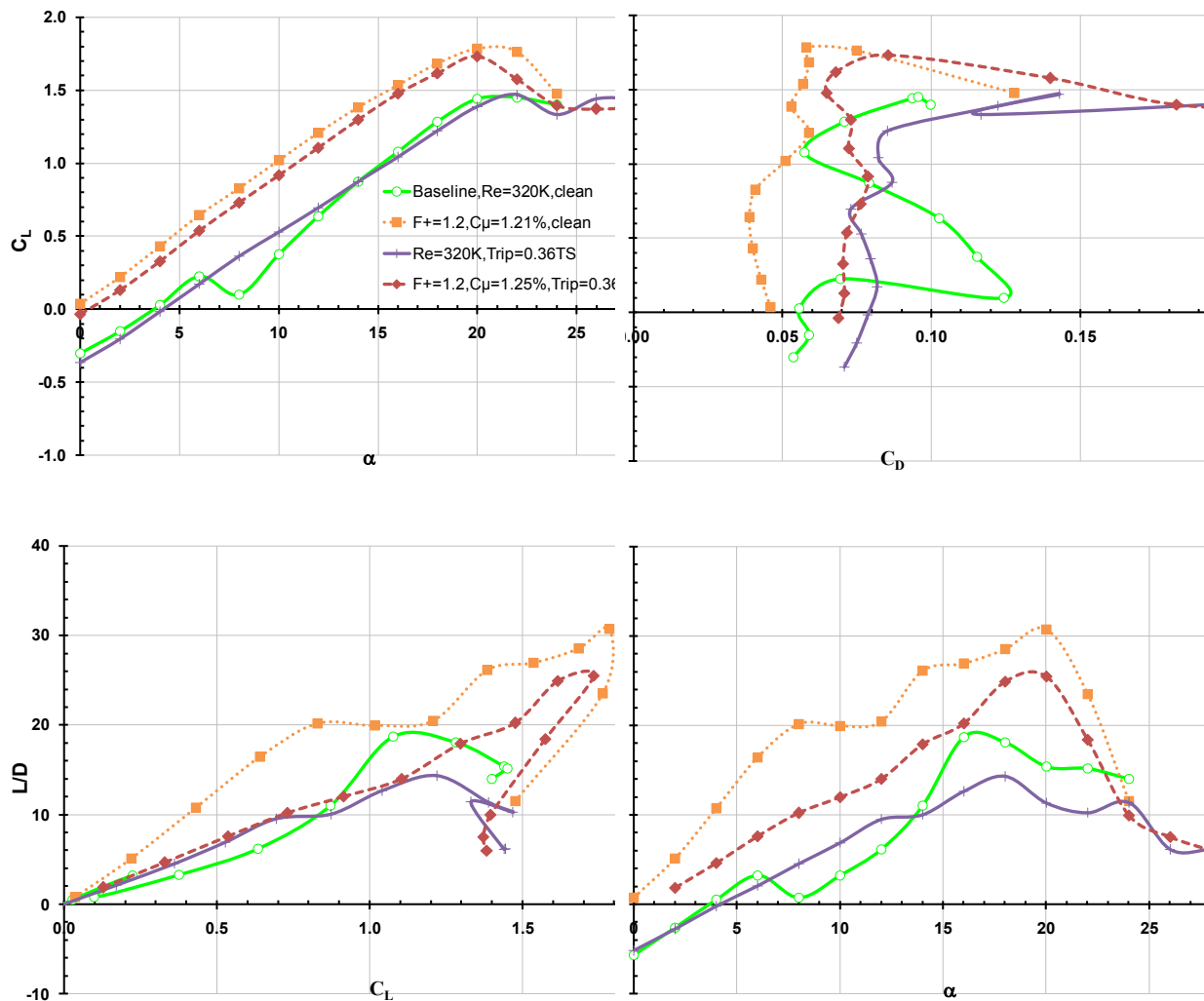


Chart 44. Roughness effects on ZMF actuation study at 20 m/s comparing a clean to a tripped airfoil.

TS roughness at 36% chord reduced L/D significantly. It also narrowed the L/D peak. Two mechanisms might have been responsible for the L/D decrease during tripping. The BL transition was forced 23% earlier, which caused loss in C_L and increase in C_f . The roughness strip itself retarded the flow locally over 5% chord possibly producing a laminar separation bubble over the width of the strip thereby increasing C_D additionally.

Chart 45 shows the effect of roughness on ZMF control performance at $Re = 480K$. The same deleterious effect existed at higher Re . With ZMF control and tripping, the performance dropped below baseline L/D . It illustrated how sensitive GLAS II performance was to transition location and surface roughness.

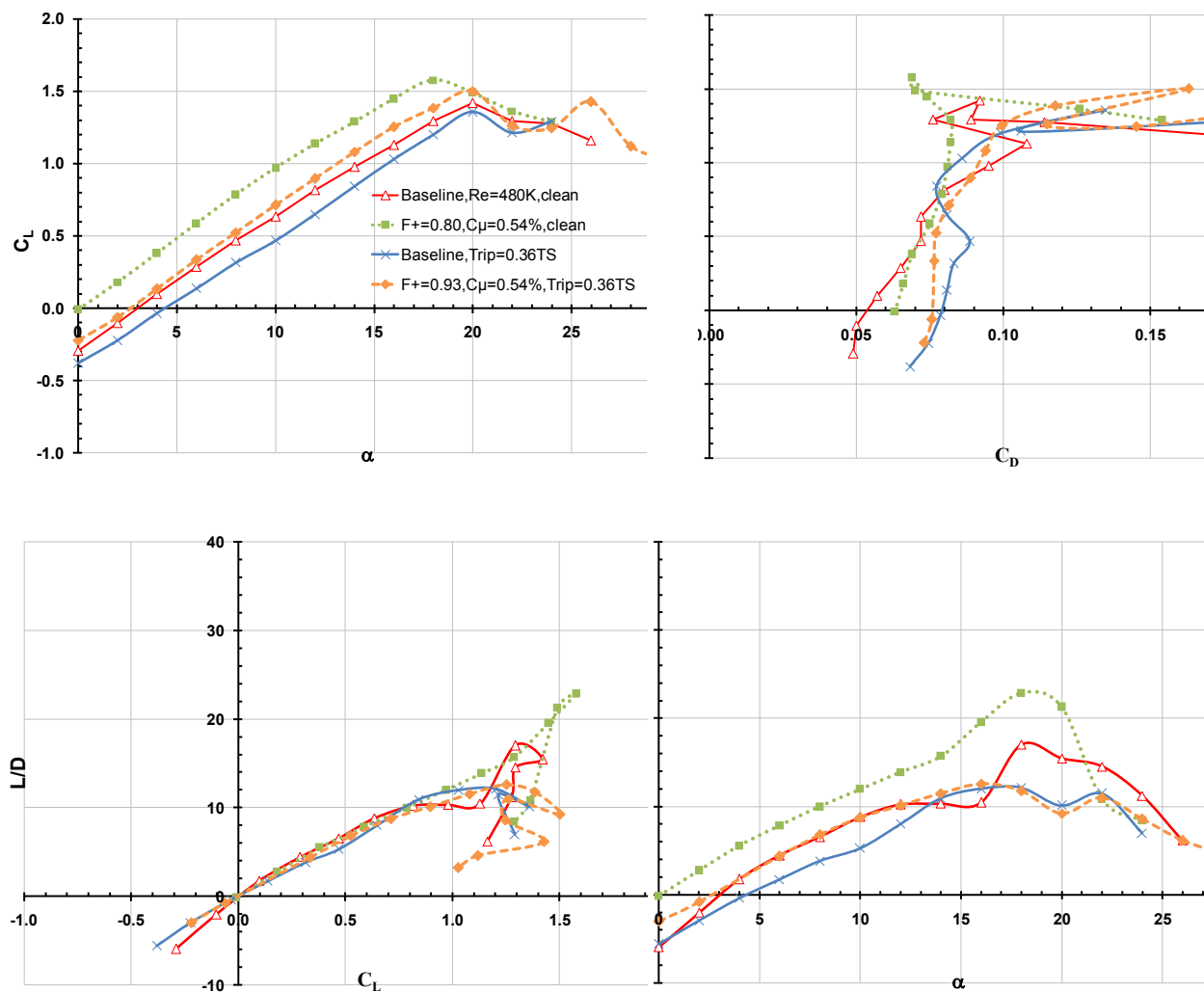


Chart 45. Roughness effects on ZMF forcing study at 30 m/s comparing a clean to a tripped airfoil.

The application of roughness at 36% chord on the TS caused L/D losses during ZMF control, which were substantial. The results indicate that with the right combination of C_μ and F^+ these losses can be avoided and separation regions can be eliminated with complete flow reattachment over the originally separated regions without tripping.

6.2.9 Effect of ZMF - and ZMF - control with Roughness on $C_{mc/4}$

$C_{mc/4}$'s for ZMF forcing are shown in Chart 46 for a clean airfoil with various Re's and ZMF_{max} with a clean/rough airfoil at $Re = 196K$. The airfoil in configuration C with added contraction was used. For each Re the ZMF control, parameters chosen resulted in the L/D_{max} to magnify potential adverse effects of ZMF control on $C_{mc/4}$.

Average $\Delta C_{mc/4} = -0.01, -0.064, -0.055,$ and 0.00 for $112K, 196K, 320K,$ and $480K$ respectively compared to baseline. The average $\frac{\partial C_{mc/4}}{\partial \alpha}$ did not change much with ZMF actuation and the curves were mostly shifted towards the highest clean Re baseline case of $480K$.

The $Re = 480K$ $C_{mc/4}$ with $C_{\mu} = 0.10\%$ did follow the baseline trend with no apparent shift.

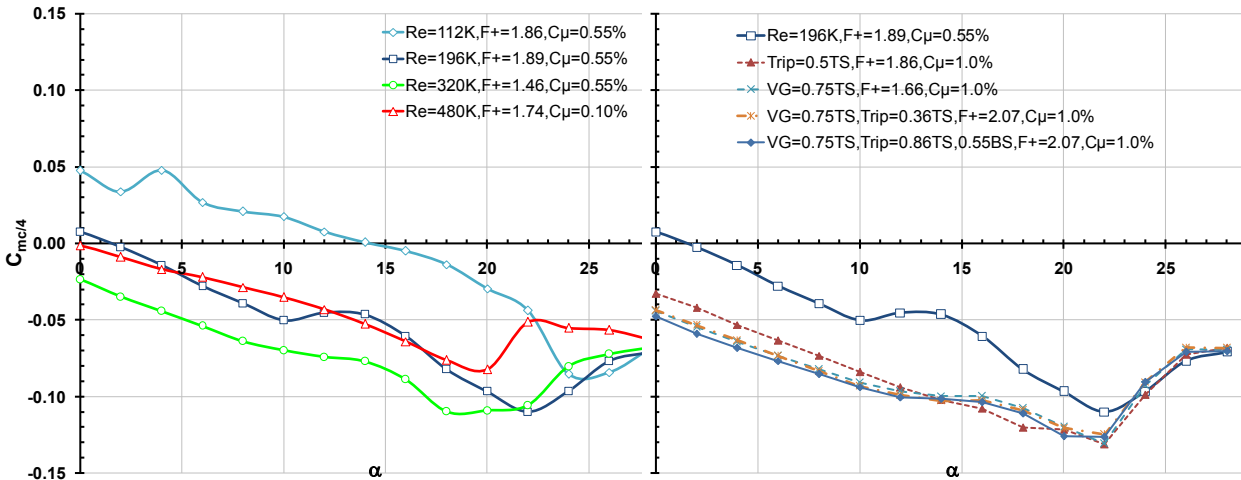


Chart 46. ZMF control study of $C_{mc/4}$ at 7 m/s, 12 m/s, 18 m/s, 20 m/s and 30 m/s for a clean airfoil and 12 m/s for an airfoil with various applied roughness strips and vortex generators. The airfoil tested was in configuration C and the splitter plate setup was used.

ZMF control had a similar effect than tripping the airfoil on $C_{mc/4}$. Variations were minor between various tripping and max ZMF forcing cases.

6.2.10 Open Loop Control through ZMF Control Parameters

If the performance on the GLAS II airfoil could be accurately mapped, at flow conditions existing during aircraft mission requirements, a failsafe closed loop control system could be implemented. The two ZMF forcing parameters, that can be easily adjusted, are F^+ and C_μ . A function generator carried on the aircraft could alter the ZMF forcing frequency continuously while an amplifier, powered by a BPU, would provide the power required of the actuators. A feedback control loop would decide the frequency and amplitude based on pressure sensor inputs, pilot inputs, aircraft dynamics, and mission goals. The determined parameters would then be compared to an existing aircraft performance map to ensure that resulting changes, due to ZMF actuation, of forces on the

aircraft or pilot are not exceeded and that operation within a save performance envelope is ensured. The control of C_L is especially important for takeoff and landing while for cruise and loiter the control of L/D would be of major concern.

From Section 6.2.7 and 6.2.8, ZMF control authority was confirmed. The ability to control the separation region on the BS ramp might be used to an advantage. The $C_{mc/4}$ as well as C_D could be controlled within a range of $12^\circ < \alpha < 18^\circ$. Another option would be to control the TS separation region around $0.50 < x/c < 0.60$ in the range $0^\circ < \alpha < 6^\circ$. Finally, the largest effect of ZMF forcing was due to controlling structures in the near wake of the airfoil around the ramp region by locking shedding frequency to forcing frequency, thereby influencing wake size and $C_{mc/4}$.

The effects of changing forcing parameters on aerodynamic coefficients are shown in Chart 47, for $Re = 235K$, with external ZMF forcing within the Davis wind tunnel. At $\alpha = 0^\circ$ the $\frac{\partial C_L}{\partial C_\mu} \approx 1.33$ for $0\% < C_\mu < 0.3\%$, and $\frac{\partial C_L}{\partial C_\mu} \approx 0.17$ for $0.3\% < C_\mu < 1.7\%$. The change in $\frac{\partial C_L}{\partial C_\mu}$, and the jump in C_L at critical C_μ , happened simultaneously with a decrease in C_D . C_D was only available for $F^+ = 0.36$, and 1.8 but C_{dp} trends still agreed with those of C_D and were therefore considered. For $F^+ = 0.36$ the C_D increased from 0.124 to 0.173 up to the critical value of C_μ , before abruptly dropping down to 0.088 , about 1.5 times less than the baseline value. If a control scheme would be implemented small C_μ 's would be chosen at lower α and larger ones at larger α , because C_L increases and C_D decreases at $C_\mu > 0.3\%$ came at eight times the required C_μ for equal ΔC_L , $\Delta C_D/\Delta C_{dp}$. This trend

was largely independent of the frequency with some caveat. $F = 150$ Hz was probably the overall best choice of forcing at low incidence because it offered the largest $\frac{\partial C_L}{\partial C_\mu}$ at $C_\mu < 0.3\%$ and a comparable $\frac{\partial C_L}{\partial C_\mu}$ to 50 Hz at $C_\mu > 0.3\%$. If duty cycles of operation were of concern to the reliability of the actuators, the following control scheme could be employed. At $C_\mu < 0.3\%$, $F = 150$ Hz would be chosen and at $C_\mu > 0.3\%$, the actuator frequency would be reduced to $F = 50$ Hz without any deterioration in C_L at the same time improving actuator life.

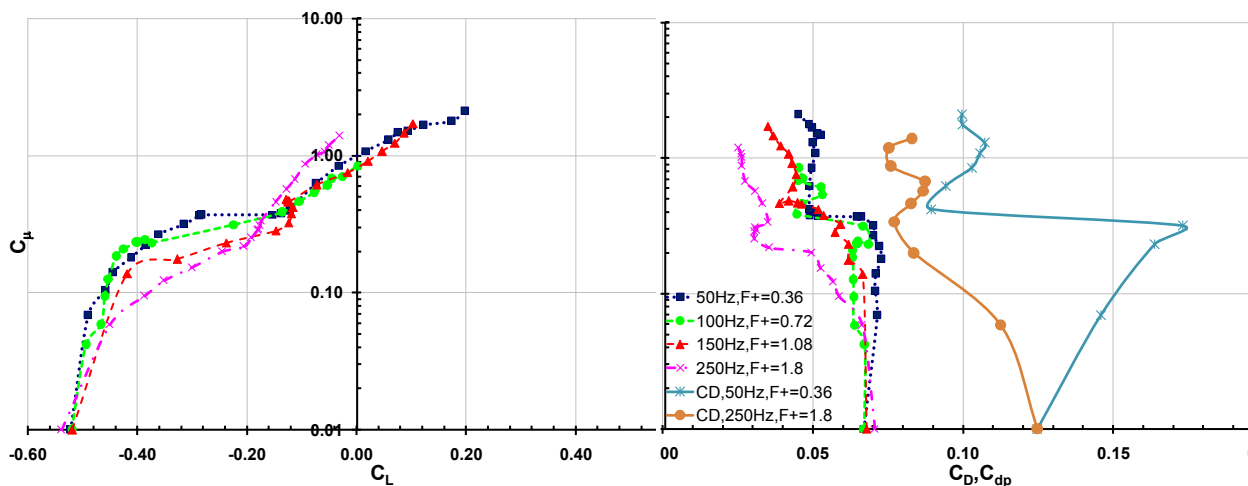


Chart 47. ZMF control frequency sweep at $\alpha = 0^\circ$ with C_μ vs. C_L and C_{dp}/C_D at 14 m/s for a clean airfoil in configuration B.

The C_μ vs. L/D is shown in Chart 48. The performance measured by C_D abruptly increased by $\Delta L/D = 6$ at $C_\mu = 0.3\%$. The L/D increase using C_{dp} occurred over a much wider range $0.1\% < C_\mu < 1\%$. The disappearance of the separation bubble on the TS is likely the reason for sudden increase in L/D at $\alpha = 0^\circ$.

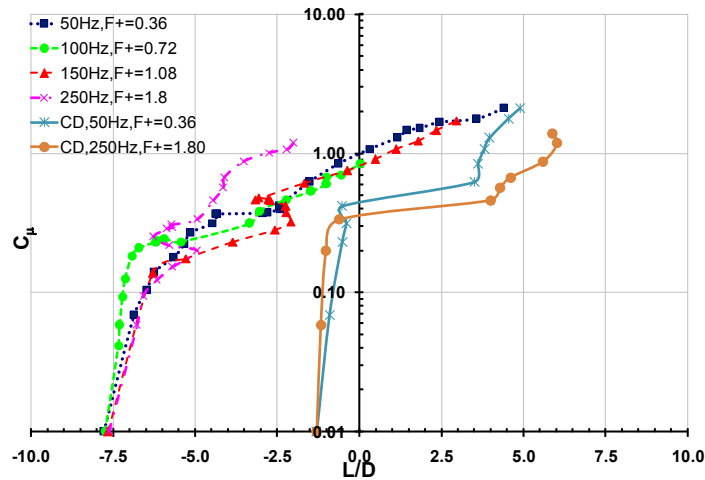


Chart 48. ZMF control frequency sweep at $\alpha = 0^\circ$ with C_μ vs. L/D at 14 m/s for a clean airfoil in configuration B.

What caused the rise in C_D at $F = 50$ Hz and could it be avoided by other means than increasing F before “critical” C_μ was reached? The ZMF forcing and baseline C_p distributions are therefore compared, with ZMF control at $C_\mu = 0.3\%$ and $F = 50$ Hz, or $F = 250$ Hz, in Chart 49 at $Re = 235K$. The separation location moved downstream by 12% for ZMF forcing compared to baseline, which should have reduced the C_D not increased it. No changes in the ramp C_p were apparent. The reason for an increase in C_D at $F = 50$ Hz was possibly the generation of a large bubble that sat between 48% and 67% chord, on the BS. This would explain the increase in C_D even though the C_L was increasing and C_{dp} was constant compared to baseline. A trip strip or roughness at 45% chord on the BS might mitigate the problem of a bubble at low α 's and C_μ 's. The small C_D at $F = 250$ Hz was due to a reduction in bubble size on the BS by $\sim 35\%$ and an improved suction peak that moved the TS separation location downstream by 7.1%.

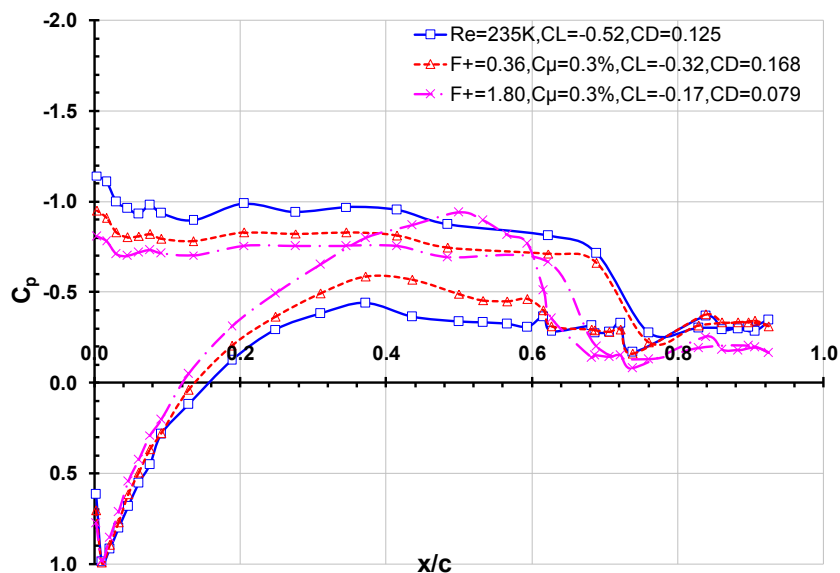


Chart 49. C_p with $F^+ = 0.36$ and 1.80 at $C_{\mu} = 0.3\%$ compared to baseline at 14 m/s. The airfoil was clean at $\alpha = 0^\circ$.

The reason for the large change in C_L over a small change in momentum input, at constant frequency, was further investigated. The C_p distributions before and after $\Delta \frac{\partial C_L}{\partial C_{\mu}}$, at $Re = 235K$, are shown in Chart 50 for $\alpha = 0^\circ$. External ZMF forcing was applied at constant $F^+ = 0.36$. After exceeding a critical $C_{\mu} = 0.39\%$ the separation location on the upper loft moved downstream from 44% chord to 62% chord creating a much more developed suction profile contrasted to forcing at subcritical levels. With a larger attachment area, the circulation was improved, raising the pressure on the entire BS generating additional lift. The pressure on the BS of the ramp also rose. Partial flow reattachment at the ramp TE was accomplished, which contributed little to the change in lift experienced, but helped reduce the drag majorly.

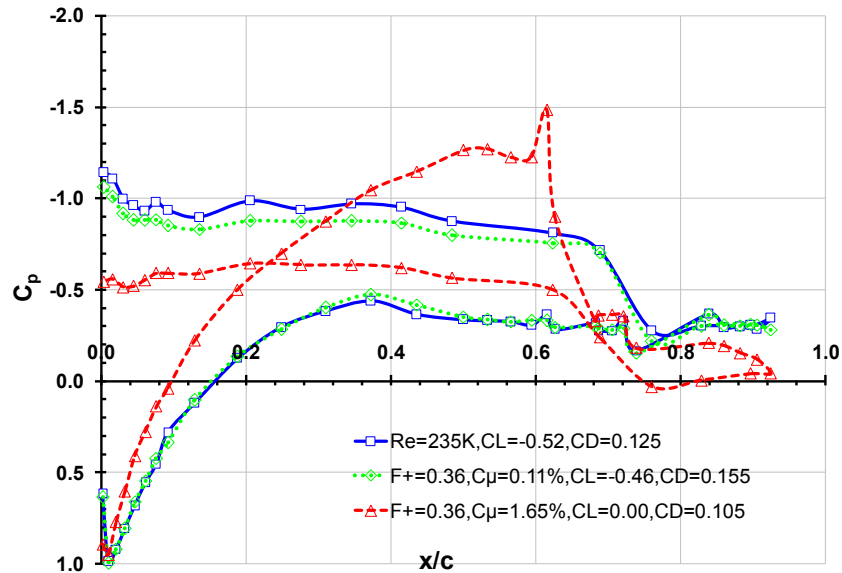


Chart 50. C_{μ} sweep study of C_p distributions before and after $\Delta \frac{\partial C_L}{\partial C_{\mu}}$ occurred compared to baseline at 14 m/s and $\alpha = 0^\circ$ for a clean airfoil and external ZMF control at $F = 50$ Hz.

The effect of C_{μ} and F^+ at $\alpha = 6^\circ$ is investigated in Chart 51 at $Re = 235K$. At $\alpha = 6^\circ$ there was much less change in $\frac{\partial C_L}{\partial C_{\mu}}$ than at $\alpha = 0^\circ$ and the change occurred in the opposite direction. No C_D data was acquired for this incidence. At $\alpha = 6^\circ$, $\frac{\partial C_L}{\partial C_{\mu}} \approx 0.154$ for $0\% < C_{\mu} < 0.5\%$, and $\frac{\partial C_L}{\partial C_{\mu}} \approx 0.32$ for $0.5\% < C_{\mu} < 1.8\%$. In the control scheme suggested above the C_{μ} should be large for larger incidence to achieve the desired change in lift. This was justified because $\frac{\partial C_L}{\partial C_{\mu}}$ for $C_{\mu} > 0.5\%$ offered C_L changes at only half the required momentum input. The momentum input, at which the jump in $\frac{\partial C_L}{\partial C_{\mu}}$ occurred, was much more dependent on frequency than before. $\frac{\partial C_L}{\partial C_{\mu}}$ changed at $C_{\mu}=0.35\%$ for 250 Hz, $C_{\mu}=0.43\%$ for 150 Hz, $C_{\mu}=0.5\%$ for 100 Hz, and $C_{\mu}=0.76\%$ for 50 Hz. A control

scheme at $\alpha = 6^\circ$ could take advantage of these results. First, AFC at 250 Hz and $C_{\mu} = 0.35\%$ should be used to achieve attachment sooner at the lowest required momentum input. Second, the frequency should be gradually reduced to 50 Hz for C_{μ} 's $> 0.8\%$ for further lift enhancements at the lowest necessary momentum input. This would improve reliability of the actuators if dutycycles and endurance were of concern. Alongside an increase in C_L the C_{dp} decreased.

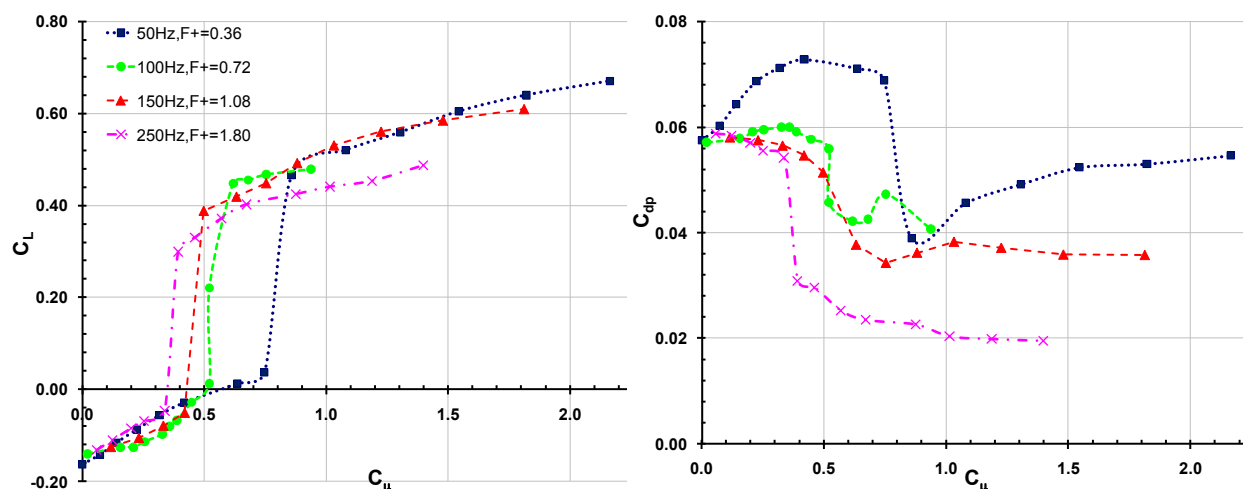


Chart 51. ZMF actuation frequency sweep at $\alpha = 6^\circ$ with C_L and C_{dp} vs. C_{μ} at 14 m/s for a clean airfoil.

At $\alpha = 6^\circ$, the effect was much more pronounced. The C_p distributions before and after lift-curve slope change at 6° are shown in Chart 52 at $Re = 235K$. External ZMF control was applied at a constant $F^+ = 0.36$. Separation on the upper loft moved downstream from 40% chord to 62% chord. Circulation increased due to a more developed suction profile causing an increase in pressure along the entire BS that

contributed to the increased lift. The generation of the large suction profile shifted the pressure over the bottom and top surface of the entire ramp.

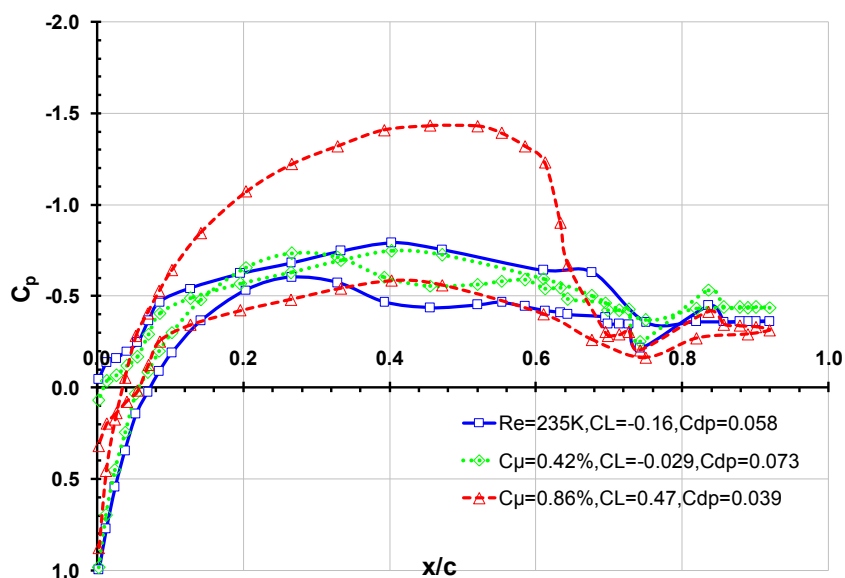


Chart 52. C_{μ} sweep study of C_p distributions before and after $\frac{\partial C_L}{\partial C_{\mu}}$ occurred compared to baseline at 14 m/s and $\alpha = 6^\circ$ for a clean airfoil and external ZMF actuation at $F = 50$ Hz.

An interesting phenomenon in the ramp was observed shown in Chart 49. From 86% chord within the ramp the pressure increased up to 70% chord in the upstream direction with a $\Delta C_p = 0.15$. The same change existed at small incidences. Two driving factors behind this phenomenon most likely existed. First, the oscillatory jet perturbations were amplified downstream with additional momentum being picked up along the way due to entrainment effects. Entrainment caused streamlines to bend downwards. The entrainment source could be modeled as a line of sinks in potential flow. Second, a global difference in speed at which the two shear layers left the airfoil existed between the top and bottom surface, as seen by the ramp. Entrainment and the fact that the ramp was at

slightly lower than atmospheric pressure accelerated fluid particles upstream to fill the void. As the particles reached the TE, they experienced a radial pressure gradient that decelerated the particles and changed their direction along the curvature of the ramp. Ahmed Hassan who performed the GLAS II CFD analysis also performed a vorticity analysis on a generic 2 D ramp in a freestream to gauge the change in reattachment length of streamlines by steady forcing at the forcing location of $(Y,X) = (0,0)$ for steady suction at $C_{\mu} = 1\%$ shown in Figure 29.¹³ This illustrated the pressure rise within the ramp of the GLAS II opposing the pressure distribution trends seen on the BS of the ramp and other parts around the airfoil.

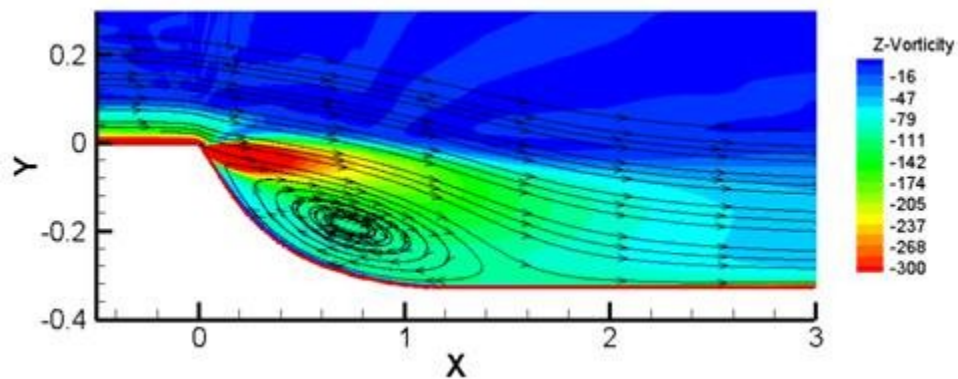


Figure 29. CFD vorticity study of a generic ramp to gauge changes in streamline reattachment length here for steady suction at $C_{\mu} = 1\%$ at $(Y,X) = (0,0)$ shown to illustrate streamline patterns within the ramp region and explain the pressure rise in the ramp opposite of the flow direction.⁷

6.3 Smoke Wire Flow Visualization Experiments

Some questions that arose up until now could only be addressed looking at C_p distributions providing an averaged and reduced image of the actual time dependent flow field over the entire airfoil. To discover and visualize dynamic flow phenomena and time dependent ZMF control behavior the airfoil was modified in configuration D.

6.5.1 Baseline Flow Study

The airfoil was covered in black, light absorptive material. The smoke-wire flow visualization technique took advantage of the reflective behavior of the immersed visualization particles called seeding particles. Seeding particles could be in solid, liquid, or gaseous phase or a combination thereof. The seeding particles generated during the experiment came from a mixture of 50% hydraulic oil and 50% purified olive oil (sweet oil). The oil wetted a wire that was heated under influence of AC current sent through the wire by a VARIAC. The wire was placed in the y plane midspan and four chord lengths upstream of the airfoil. The wire spanned the entire wind tunnel height. Four large halogen lamps illuminated the particles, which reflected and refracted the light. The white lines in the following visualizations were lines of particles originating from the same source that of the wire. Hence, they were considered streak lines, which are commonly used in flow visualization techniques. Only in the case of inviscid, incompressible, irrotational, and steady flow do the streak lines coincide with flow streamlines. The advantage of the smoke-wire technique was that it could be implemented quickly and inexpensively. The disadvantage lied in the seeding particles of the partially combusted

oil itself. By heating the oil, it evaporated as a heated gas plus uncombusted particles that rose in the surrounding ambient temperature air. Hence, the smoke was not neutrally buoyant and tended to rise with time making it difficult to arrive at horizontal streak lines. Another disadvantage was the limited amount of smoke that could be produced by a single coated wire. That volume was limited due to the oil's volume surrounding the wire as well as the oil's thermodynamic and fluid properties. Another disadvantage was that it was invasive because the wire itself influenced the downstream flow, in which it was seeding the particles. Three areas of interest were investigated the LE, top ramp, and bottom ramp. Reynolds numbers ranged from 8.28K to 66,2K, limited by the amount of smoke that could be generated during a single heating session, the cooling effect on the wire itself, and the necessary AC current that was required to overcome cooling. Starting with the LE of the airfoil the effect of flow control on the stagnation point location was visualized. The LE was viewed through the Plexiglas side plate during a baseline flow case at $Re = 22.3K$ and zero incidence shown in Figure 30. The streak lines impinged on the LE at the airfoils midspan location. Seeding particles came to rest at the nose's TS indicative of the airfoils stagnation point. All pictures had been enhanced to increase contrast of the seeding particles.

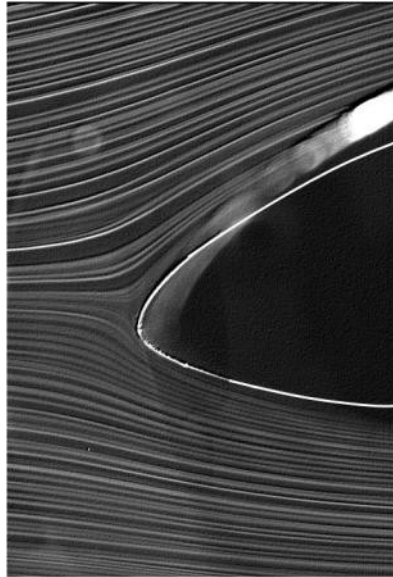


Figure 30. Baseline smoke-wire study of the GLAS II's LE at $\alpha = 0^\circ$ and 1.35 m/s in configuration D.

The baseline flow over the TS ramp was scrutinized at $\alpha = 10^\circ$ perspective viewed from the right of the airfoil through the clear endplates shown in Figure 31. Shear layer roll up was visible and a smoke free zone showed an entirely separated ramp. The white reflective marker indicated the midspan location along the ramp. Successive roll ups of the shear layer occurred also called vortices. Vortex size increased downstream of the separation location. Since flow within the shear layer was unsteady and viscous effects were important the white streak lines were only indicative of the vortices not the vortices themselves.



Figure 31. Baseline smoke-wire image of the TS ramp at $\alpha = 0^\circ$ and 1.35 m/s. Shear layer rollup was indicated through concentrated smoke streak lines. The flow separated from the TS around 50% chord.

The third area of interest was the ramp's BS. The baseline flow was investigated in search of a separation bubble at low incidence Figure 32. Clearly, the streak lines separated at about 70% chord from the BS. The same shear layer roll up was visible like on top of the ramp, but happened sooner with less well defined structures. No separation bubble could be seen.

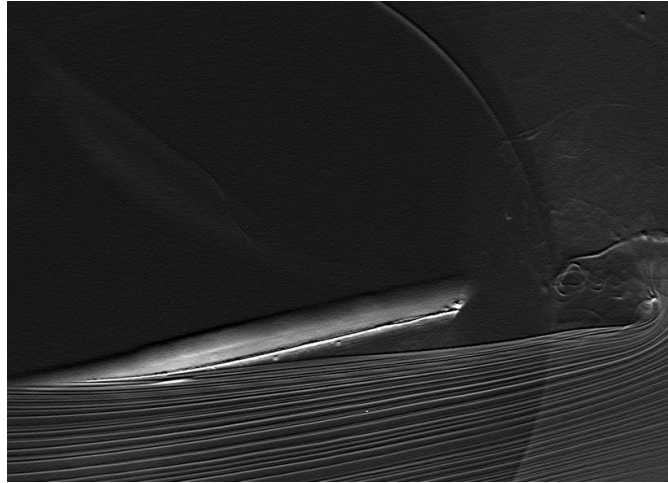


Figure 32. Baseline smoke-wire image of the BS ramp $\alpha = 0^\circ$ and 1.35 m/s. The flow separated at BS $\sim 70\%$ chord and the shear layer rolled up in the ccw direction.

6.5.2 AFC Flow Study

What happened to the flow around the airfoil during ZMF actuation in configuration C? The flow over the nose was visualized for ZMF control at $F = 200$ Hz and $C_{\mu} = 176\%$ shown in Figure 33. Tests were run at the same conditions as in baseline for $\alpha = 0^\circ$ and Re ranged from 8.28K to 66,2K. The stagnation point visualized by the streak lines jumped to the nose BS. A shift in stagnation point from TS to BS usually had a global effect on circulation around the airfoil increasing the lift substantially. A bending upward of the streak lines could be observed resulting in flow reattachment. Fluid particles over the upper loft were accelerated through the large suction peak. The source of particle acceleration came from the oscillating ZMF control jet. It's net jet momentum, a result of vortex shedding, was positive creating a jet as seen by the flow, in addition to the resulting flow entrainment from the pulsating jet. Because of the pressure gradient

and the resulting velocity potential between the upper and lower loft streak lines bend upward.

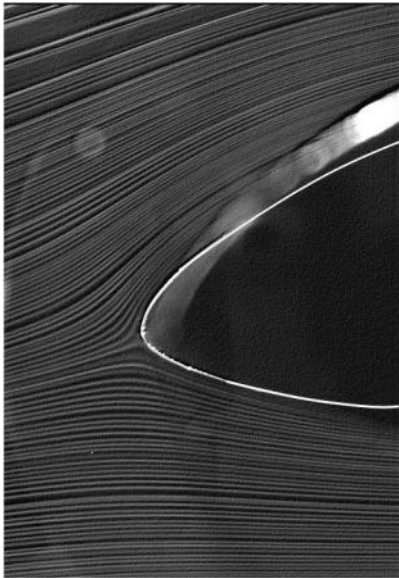


Figure 33. ZMF actuation smoke-wire image of the airfoil nose at $\alpha = 0^\circ$ and 1.35 m/s. Forcing parameters were $F = 200$ Hz and $C_\mu = 176\%$ in airfoil configuration C and D.

Actuated case with the ramp's TS seen at a 5° perspective viewed from the side with same ZMF control parameters as before are shown in Figure 34. Complete turbulent attachment over the entire ramp was accomplished. The flow attached in a laminar fashion over the upper loft until 59.65% chord. The streak lines bent downwards as the smoke particles accelerate along the convex curvature. The potential of complete turbulent attachment over the ramp through ZMF actuation was realized at very high C_μ 's.

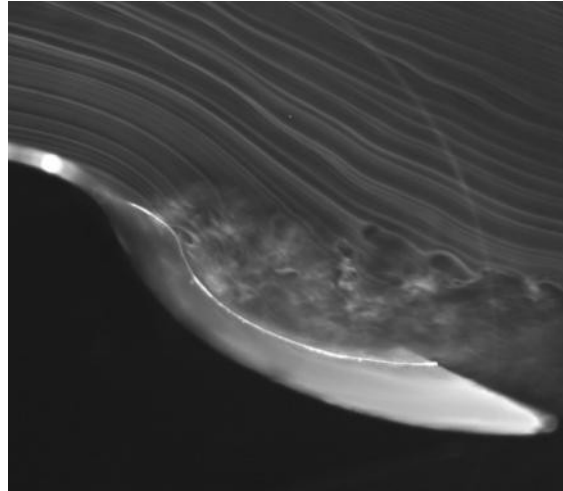


Figure 34. ZMF control smoke-wire image of the TS ramp at $\alpha = 0^\circ$ and 1.35 m/s. Forcing parameters were $F = 200$ Hz and $C_{\mu} = 176\%$ in airfoil configuration C and D.

The ZMF forcing case with the ramp's BS at 5° perspective viewed from the side with the same ZMF forcing parameters as before is shown in Figure 35. The ramp's BS was completely attached with streak lines following the airfoil's geometry closely. The wake was turbulent and no organized structures were indicated by the smoke streak lines.

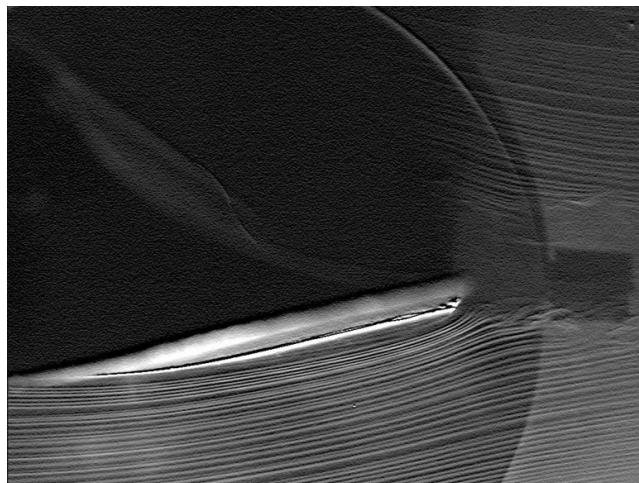


Figure 35. ZMF control smoke-wire image of the BS ramp at $\alpha = 0^\circ$ and 1.35 m/s. Forcing parameters were $F = 200$ Hz and $C_\mu = 176\%$ in airfoil configuration C and D.

After investigation of the pressure distribution in Chart 49 a bubble at the BS TE was suspected. The bubble increased the drag at increasing C_μ 's up until a critical momentum input was reached. The bubble did not show up for high actuation frequencies only for low ones'. Therefore, the AFC frequency was reduced to investigate if the suspected bubble actually existed and could be visualized. The flow over the BS ramp for ZMF forcing at $F = 100$ Hz and $C_\mu = 65.8\%$ is shown in Figure 36. The streak lines showed a separation bubble stretching from 85% chord all the way to the TE where partial reattachment occurred. This lent some credibility to the smoke-wire method that only allowed testing at very low Re 's with very large C_μ 's.

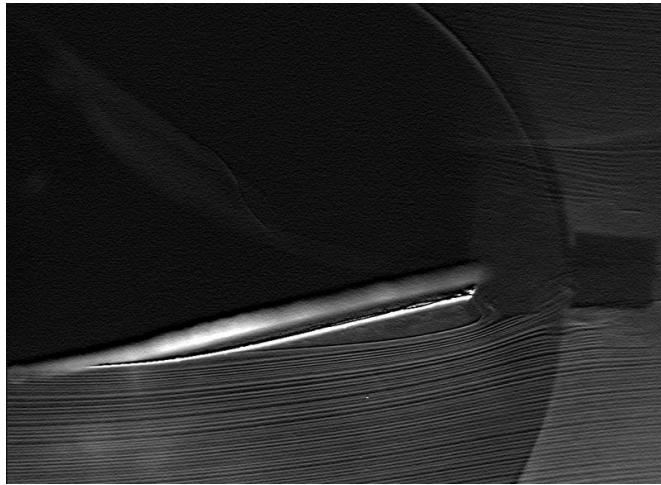


Figure 36. ZMF control smoke-wire image of the BS ramp at $\alpha = 0^\circ$ and 1.35 m/s. Forcing parameters were $F = 100$ Hz and $C_\mu = 65.8\%$ in airfoil configuration C and D.

In conclusion of smoke-wire flow visualization experiments stream wise flow structures were unveiled and problematic areas were investigated. The technique proved uncomplicated and produced qualitatively useful results. It was shown that the stagnation point at the LE jumped from top to bottom during ZMF actuation substantially changing the entire velocity field around the airfoil. The existence of a separation bubble with partial reattachment at the TE was validated during ZMF control at frequencies of less than one-half of 250Hz.

6.4 Particle Image Velocimetry Flow Visualization Experiments

Due to the airfoils thickness and the ramp's convex concave inflection the assumed 2D flow over TS ramp was questioned. PIV was the best choice to investigate any spanwise flow structures within the ramp region. Lutz Taubert and Boris Zakharin performed the 2D PIV experiment and data analysis on the airfoil in configuration D. A dual pulsed laser sheet illuminated the plane perpendicular to the flow within the ramp spanning the entire wind tunnel width. A camera synchronized to the laser was used to take one picture per laser pulse resolving the movement of the seeding particles between two successive frames as taken by the camera. Knowing the displacement of a particle or group of particles and the time between successive frames the velocity and acceleration vectors were calculated. Tecplot was used to graph the results. Through PIV velocity, acceleration, vorticity, and streamlines could be analyzed. A commercially available smoke generator produced the seeding particles (smoke). The smoke filled the entire lab in order to achieve the desired density and uniformity of seeding particles. Instantaneous

as well as time averaged data was taken at 20 m/s and $\alpha = 6^\circ$. Similar to the smoke-wire experiments the airfoil was covered in black light absorptive material to minimize reflections from the metal alloy surface of the airfoil that could potentially harm any useful quantitative estimation. The experimental apparatus was extensively shielded to avoid exposure to laser or reflected laser light. Streamwise instantaneous vortical structures were illuminated by the laser sheet at 20 m/s seen in Figure 37 during a baseline run. The white horizontal line highlighted the airfoil's TE with the top of the photo corresponding to the airfoil's upper loft. The structures did not by themselves represent streamlines but were illuminated concentrated smoke streak and were indicative of vortices being present. Another feature of the spanwise structures was the fact that adjacent structures counter rotated. These structures were created by centrifugal instabilities due to the ramps concavity and also known as Görtler vortices.²⁵

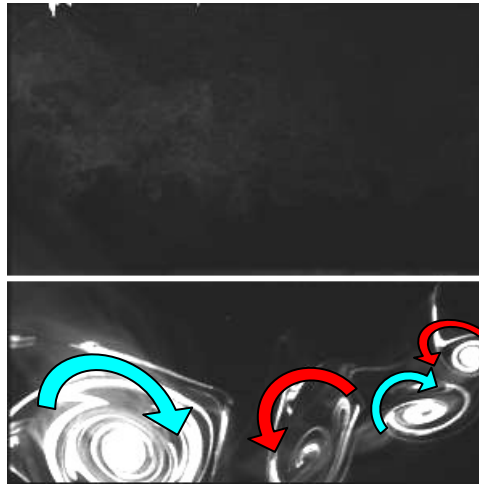


Figure 37. Instantaneous PIV image of spanwise flow structures illuminated by a laser sheet placed perpendicular to the flow within the ramp during a baseline run at 20 m/s. The white line indicates the TE.

Once internal ZMF forcing at $F = 200$ Hz and $C_{\mu} = 0.88\%$ was activated the structures increased in visible intensity and changed their location in the y plane moving closer to the ramp's surface shown in Figure 38. They also exhibited the counter rotating behavior. It was difficult to tell if the structures lied in the same z plane or if they were randomly jumping around.

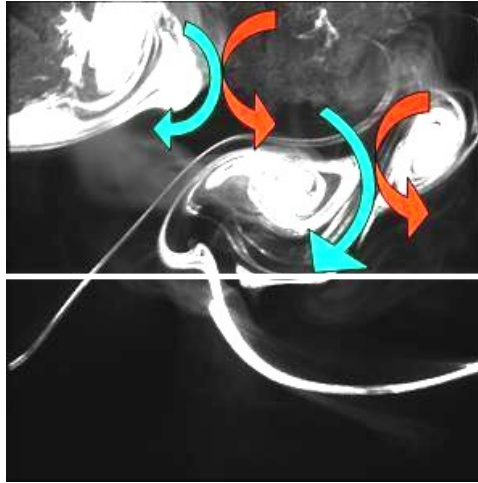


Figure 38. Instantaneous PIV study of spanwise flow structures illuminated by a laser sheet placed perpendicular to the flow within the ramp during ZMF actuation airfoil configuration C with $C_{\mu} = 0.88\%$ and $F = 200$ Hz.

The instantaneous structures looked chaotic and successive images did not show much similarity. Therefore, an averaged PIV study was conducted to show if any spanwise stationary flow structures existed within the ramp. A good quantitative analysis was not performed and all vorticity values should be regarded for their qualitative information. Vorticity contours are plotted in Figure 39 for baseline flow at 20 m/s. The contour map was created by averaging ~ 100 successive images and calculating averaged velocity and acceleration vectors and evaluating their partial derivatives. Since vorticity in the z plane was defined as Equation (15) and $v(x,y)$ and $u(x,y)$ were known the vorticity could be calculated.

$$\Omega_z = \left(\frac{\partial v}{\partial x} - \frac{\partial u}{\partial y} \right) \hat{k} \quad (15)$$

Bright green indicated zero vorticity, dark blue $\Omega_z = -130$ Hz, and dark red $\Omega_z = +130$ Hz. Only cw $\Omega_z = -80$ Hz stationary vorticity concentrations could be seen with no apparent and visible ccw vortex pairs. Since counter rotating vortex pairs could be seen during the instantaneous study, the conclusion was that those pairs were not stationary and moved in space and time resulting in an undistinguishable uniform mean vorticity field.

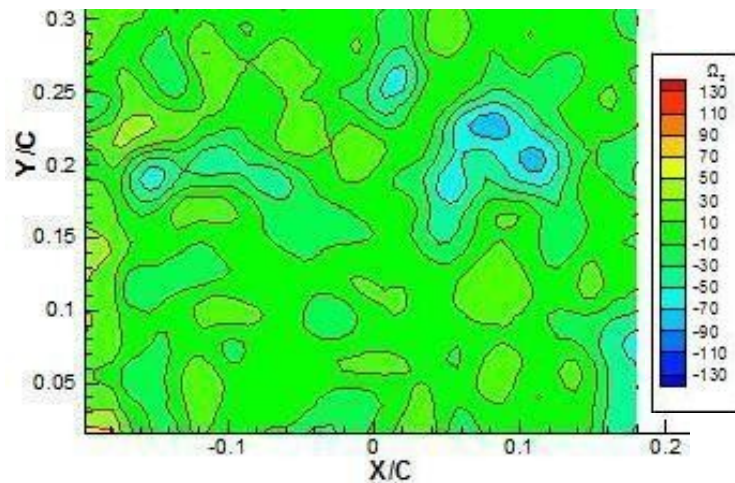


Figure 39. Averaged PIV image of spanwise vorticity within the ramp during a baseline run at 20 m/s. $y/c = 0$ indicated the TE of the airfoil and $y/c = 0.318$ indicated the upper loft of the GLAS II.

With ZMF control the averaged vorticity contours are shown in Figure 40 at $F = 200$ Hz and $C_{\mu} = 0.88\%$. A stationary counter rotating vortex pair was resolved midspan of the ramp. This came as a surprise considering the averaged baseline vorticity contours and the seemingly chaotic instantaneous flow structures. ZMF forcing did not attach the

flow over the ramp at 20 m/s and $C_{\mu} = 0.88\%$ but effectively locked in Görtler type instabilities and amplified them.

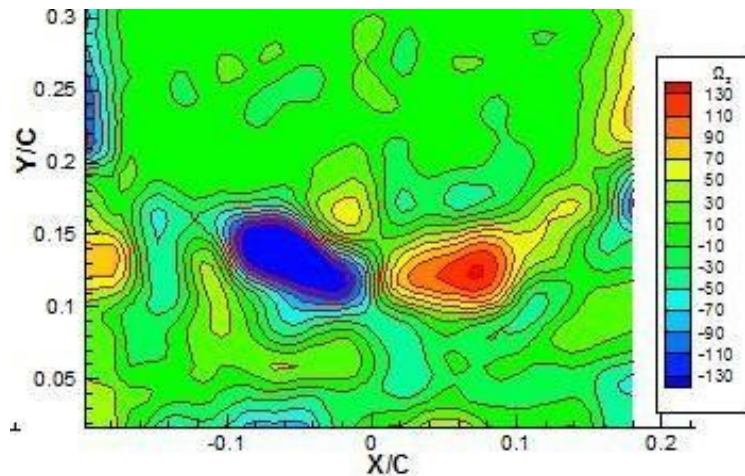


Figure 40. ZMF control averaged PIV image of spanwise ramp vorticity at 20 m/s with $F = 200$ Hz, $C_{\mu} = 0.88\%$. $Y/c = 0$ indicated the TE and $y/c = 0.318$ indicated the upper loft of the GLAS II.

In conclusion, of this topic several instabilities around the GLAS II were visualized using two different flow visualization techniques. Smoke-wire flow visualization resolved instantaneous streamwise flow structures, while PIV resolved instantaneous and/or averaged spanwise flow structures. The advantage of PIV over smoke-wire was the ability to resolve structures at much shorter time steps and successive frames due to an unlimited supply of seeding particles that were also much more evenly distributed. Spanwise Görtler vortices were discovered within the ramp region that were stationary during forcing and non-stationary and further removed from the ramp surface in the y direction during baseline.

6.5 Conclusion

Clean baseline airfoil performance was strongly dependent on Re. For a clean airfoil a Re plateau was reached at Re = 480K. With TS tripping at $x/c = 0.36$, and 0.50 and ramp VG's at $x/c = 0.75$ the same plateau could be reached much earlier at Re = 250K.

A laminar separation bubble on the TS between $0.35 < x/c < 0.60$ was responsible for C_L/C_D - hysteresis. An abrupt change in $\frac{dC_L \cup dC_D}{d\alpha}$ was often indicative of the existence of a bubble and C_L/C_D - hysteresis while a gradual change was not. Other laminar separation bubbles existed one on the TS LE and another on the BS at $x/c = 0.56$. Both did not affect hysteresis but influenced C_L and C_D in certain ranges of α .

Roughness on the TS at $x/c = 0.36$ eliminated hysteresis by tripping the BL and removing the laminar separation bubble. Applying BS roughness at $x/c = 0.56$ improved C_D additionally between $12^\circ < \alpha < 18^\circ$ by removing another smaller laminar separation bubble. Roughness had an overall deleterious effect on L/D at Re = 480K where hysteresis was not apparent. In particular, in conjunction with ZMF forcing roughness was deleterious to L/D.

Glauert's hypothesized and researched airfoil performance for steady AFC through the $x/c = 0.698$ slot was unattainable. The optimized $x/c = 0.59$ slot, for C_μ 's, c_μ 's $< 10\%$, was much more effective than the old slot for ZMF control or steady AFC.

ZMF forcing required less C_{μ} than steady suction or blowing even after accounting for losses in airfoil L/D. ZMF control appeared to delay α_s on average by 2° , while steady AFC did not. For steady AFC, at constant c_{μ} , C_L improvement was constant when increasing Re. For ZMF actuation, no such relationship could be seen.

With ZMF control only the $C_{mc/4}$ tended towards the clean airfoil $C_{mc/4}$ curve for $Re = 480K$. With ZMF and tripping there was a slight shift downward by 0.04.

A F^+ close to 1 improved the overall L/D the most. ZMF forcing provided both C_L and C_D benefits. During ZMF control, the TS bubble was removed and for certain F^+ and large enough C_{μ} the bubble on the BS as well without any additional tripping or roughness.

APPENDIX

Benjamin Wesley was born in Berlin Germany 1978. He completed his basic education through 10th grade in Blumberg, a little town deep in the southwest of Germany. He continued with a four year Apprenticeship at TRW Motor Components. By then, he decided to pursue an advanced degree in the USA. Therefore, he finished his technical Abitur at the Hohentwiel Gewerbeschule through 13th grade. After moving to Glendale Arizona in 2001, he spent a year at the Glendale Community College to complete most of his lower division college requirements. Currently he lives in Seattle working for Boeing on the Boeing 787 maintenance-engineering program.

REFERENCES

- ¹ GLAUERT, M.B., "THE APPLICATION OF THE EXACT METHODS OF AEROFOIL DESIGN", REPORTS AND MEMORANDA NO. 2683, AERONAUTICAL RESEARCH COUNCIL REPORTS AND MEMORANDA, HIS MAJESTY'S STATIONERY OFFICE, LONDON 1947.
- ² GLAUERT, M.B., "THE DESIGN OF SUCTION AEROFOILS WITH A VERY LARGE CL-RANGE", REPORTS AND MEMORANDA NO. 2111, AERONAUTICAL RESEARCH COUNCIL REPORTS AND MEMORANDA, HIS MAJESTY'S STATIONERY OFFICE, LONDON 1955.
- ³ DESKTOP AERONAUTICS, INC. (2007). THICK AIRFOIL DESIGN. APPLIED AERODYNAMICS A DIGITAL TEXTBOOK, 5TH EDITION. RETRIEVED FEBRUARY 2007 FROM [HTTP://DESKTOPAERO.COM/APPLIEDAERO/AIRFOILS2/THICKSECTIONS.HTML](http://desktopaero.com/appliedaero/airfoils2/thicksections.html)
- ⁴ PRIYANK, V., (2003). MASTER THESIS. "EFFECT OF ACTIVE FLOW CONTROL AT THE LEADING AND TRAILING EDGES OF A GENERIC AIRFOIL HAVING A DIVERGENT TRAILING EDGE."
- ⁵ OSTER, D ., AND WYGNANSKI, I., "THE FORCED MIXING LAYER BETWEEN PARALLEL STREAMS," JOURNAL OF FLUID MECHANICS, VOLUME 123, PAGES 91-130, 1982.
- ⁶ KATZ, Y ., NISHRI, B ., AND WYGNANSKI, I., "THE DELAY OF BOUNDARY LAYER SEPARATION BY OSCILLATORY ACTIVE CONTROL," PHYSICS OF FLUIDS, FEBRUARY 1989.
- ⁷ NEUBERGER, D ., AND WYGNANSKI, I., "THE USE OF A VIBRATING RIBBON TO DELAY SEPARATION ON TWO - DIMENSIONAL AIRFOILS: SOME PRELIMINARY OBSERVATIONS," PRESENTATION AT THE WORKSHOP ON UNSTEADY SEPARATED FLOW, AIR FORCE ACADEMY, JULY 1987.

⁸ ZHOU, M .D ., AND WYGNANSKI, I., “PARAMETERS GOVERNING THE TURBULENT WALL JET IN AN EXTERNAL STREAM,” AIAA JOURNAL, VOLUME 31, NUMBER 5, PAGES 848 -853, 1993.

⁹ SEIFERT, A ., BACHAR, T ., KOSS, D ., SHEPSHELOVICH, M ., WYGNANSKI, I., “OSCILLATORY BLOWING: A TOOL TO DELAY BOUNDARY-LAYER SEPARATION,” AIAA JOURNAL, VOLUME 31, NUMBER 11, PAGES 2052-2060, 1993.

¹⁰ SEIFERT, A., DARABI, A ., WYGNANSKI, I., “DELAY OF AIRFOIL STALL BY PERIODIC EXCITATION,” AIAA JOURNAL, VOLUME 31, NUMBER 4, PAGES 691-698, 1996.

¹¹ GREENBLATT, D ., AND WYGNANSKI, I., “USE OF PERIODIC EXCITATION TO ENHANCE AIRFOIL PERFORMANCE AT LOW REYNOLDS NUMBERS,” JOURNAL OF AIRCRAFT, VOLUME 38, NUMBER 1, PAGES 190-192, 2000.

¹² WESLEY, B., ZAKHARIN, B., WYGNANSKI, I., “SEVERAL ASPECTS OF ACTIVE FLOW CONTROL ON MODIFIED GLAS II AIRFOIL” PROCEEDINGS FOR SUBMISSION TO AIAA CONFERENCE IN SAN FRANCISCO, 2005.

¹³ HASSAN, A., PRIVATE COMMUNICATION, 2005.

¹⁴ ESTERLINE PRESSURE SYSTEM. MINIATURE ELECTRONIC PRESSURE SCANNERS, ESP-16HD/32HD/64HD. RETRIEVED FEBRUARY 2007 FROM [HTTP://WWW.PRESSURESYSTEMS.COM/PDF_FILES/ESPHD-1004.PDF](http://www.pressuresystems.com/pdf_files/ESPHD-1004.pdf)

¹⁵ ENDEVCO. PIEZORESISTIVE PRESSURE TRANSDUCER, MODEL 8507C. RETRIEVED FEBRUARY 2007 FROM [HTTP://WWW.BKSV.COM/PDF/8507C-2-5-15-50.PDF](http://www.bksv.com/pdf/8507C-2-5-15-50.pdf)

¹⁶ MKS INSTRUMENTS. ORDERING INFORMATION, TYPE 698 DIFFERENTIAL PRESSURE SENSOR. RETRIEVED FEBRUARY 2007 FROM [HTTP://WWW.MKSINST.COM/DOCS/UR/600HI_AC.PDF](http://www.mksinst.com/docs/UR/600HI_AC.pdf)

¹⁷ AA LAB SYSTEMS. AN-1003 HOT-WIRE ANEMOMETER, TECHNICAL SPECIFICATION. RETRIEVED FEBRUARY 2007 FROM [HTTP://WWW.LAB-SYSTEMS.COM/PRODUCTS/FLOW-MEA/AN1003/TECHSPEC.HTM](http://www.lab-systems.com/products/flow-meas/AN1003/TECHSPEC.HTM)

¹⁸ NATIONAL INSTRUMENTS. NI 6023E/6024E/6025E FAMILY SPECIFICATIONS. RETRIEVED FEBRUARY 2007 [HTTP://WWW.NI.COM/PDF/MANUALS/370719C.PDF](http://www.ni.com/pdf/manuals/370719c.pdf)

¹⁹ KING INSTRUMENT COMPANY. 7520 & 7530 SERIES PDF, ACRYLIC METERING TUBE. RETRIEVED FROM [HTTP://WWW.KINGINSTRUMENTCO.COM/PDF/7520_7530_SERIES.PDF](http://www.kinginstrumentco.com/pdf/7520_7530_series.pdf)

²⁰ ALEXANDER LEE SIMPSON. HOT-WIRE AND HOT-FILM ANEMOMETRY. RETRIEVED FEBRUARY 2007 FROM [HTTP://WWW.AOE.VT.EDU/~SIMPSON/AOE4154/HOTWIRELAB.PDF](http://www.aoe.vt.edu/~simpson/aoe4154/hotwirelab.pdf)

²¹ JOHN D. ANDERSON, JR. (2001). FUNDAMENTALS OF AERODYNAMICS, 3RD EDITION, 116-123. NEW YORK: MCGRAW-HILL.

²² NATIONAL INSTRUMENTS. SCXI UNIVERSAL STRAIN GAUGE INPUT MODULE, NI SCXI-1520. RETRIEVED FEBRUARY 2007 FROM [HTTP://WWW.NI.COM/PDF/PRODUCTS/US/4SCXISC286_ETC_196.PDF](http://www.ni.com/pdf/products/us/4scxisc286_etc_196.pdf)

²³ N. GREGORY, B.A., “FURTHER WIND TUNNEL TESTS ON A 30 PER CENT SYMMETRICAL SUCTION AEROFOIL WITH A MOVABLE FLAP”, REPORTS AND MEMORANDA No. 2287, AERONAUTICAL RESEARCH COUNCIL REPORTS AND MEMORANDA, HIS MAJESTY’S STATIONERY OFFICE, LONDON 1950.

²⁴ C. SALTER, M.A., “TESTS ON A GLAS II WING WITHOUT SUCTION IN THE COMPRESSED AIR WIND TUNNEL”, REPORTS AND MEMORANDA No. 2540, AERONAUTICAL RESEARCH COUNCIL REPORTS AND MEMORANDA, HIS MAJESTY’S STATIONERY OFFICE, LONDON 1948.

²⁵ SCHLICHTING H., (1951). 325 – 330. GRENZSCHICHT-THEOIE. KARLSRUHE: G. BRAUN.